



GEORG-AUGUST-UNIVERSITÄT
GÖTTINGEN

**THE VIRTUAL EAR: DEDUCING TRANSDUCER FUNCTION IN THE
DROSOPHILA EAR**

Dissertation

for the award of the degree

“Doctor rerum naturalium”

Division of Mathematics and Natural Sciences

of the Georg-August-Universität Göttingen

Submitted by

Qianhao Lu

From Guiyang, China

Göttingen, 2011

Members of Thesis Committee

Prof. Dr. Martin Göpfert (Supervisor/Reviewer)

Georg-August-University of Göttingen, Cellular Neurobiology

Prof. Dr. André Fiala (Reviewer)

Georg-August-University of Göttingen, Molecular Neurobiology of Behaviour

Dr. Jan Benda

Ludwig-Maximilians-University München, Department Biology II

Oral examination:

I, Qianhao Lu, herewith declare that my PhD thesis entitled “The Virtual Ear: Deducing Transducer Function in the *Drosophila* Ear” was written independently. No other sources and aids than the quoted were used.

Qianhao Lu

Göttingen, September 2011

Table of Contents

1. Introduction.....	5
1.1. Mechanosensation	5
1.2. Hearing in <i>Drosophila</i>	6
1.3. Anatomy of the fly’s ear.....	7
1.4. Mechanics of <i>Drosophila</i> sound receiver.....	8
1.5. Active amplification	10
1.6. Motility of sound receptors of <i>Drosophila</i>	11
1.7. Molecular mechanisms of the sensory neurons.....	12
1.7.1 Candidate transducer is required for the active amplification	12
1.7.2 Transducer-based model of <i>Drosophila</i> hearing organ.....	14
1.8. Aim of this study	17
2. Material and methods	19
2.1. Fly lines	19
2.2. Fly preparation for mechanical measurement	19
2.3. Mechanical Measurements	20
2.3.1 Free fluctuations of the sound receiver	20
2.3.2 Sound-induced intensity characteristic of the sound receiver.....	20
2.3.3 Passive receiver mechanics	21
2.3.4 Sound-induced vibrations	23
2.3.5 Mechanical & nerve response to step stimulus	27
2.3.6 Receiver’s linear response function for weak sinusoidal forcing ...	30
2.4. Pre-processing of experimental data	31
2.4.1 Drift correction.....	31
2.4.2 Outlier detection.....	32

2.4.3	Averaging	33
2.4.4	Data smoothing.....	34
2.5.	Summary of experimental data	35
2.6.	System requirement and integrated libraries for the programs.....	35
3.	Results	39
3.1.	The virtual fly ear	40
3.1.1	Structure and workflow of the programs.....	40
3.1.2	Post-processing of the experimental data	41
3.1.3	Data storage (database structure).....	48
3.1.4	Graphical user interfaces	50
3.1.5	The models	54
3.2.	Model selection and Akaike's information criterion	77
3.2.1	Akaike's Information Criterion (<i>AIC</i>).....	77
3.2.2	Model selection by using <i>AIC</i>	78
3.3.	Assessment of active process by calculation of energy flux.....	82
3.3.1	The fluctuation of sound receiver of anesthetized fly	82
3.3.2	The active and passive components betrayed by the sound receiver 83	
3.3.3	The dissipation rate spectrum.....	84
3.3.4	Energy flux during the fluctuation of the sound receiver.....	86
3.3.5	Energy flux and frequency tuning during sound stimulation	89
4.	Discussion	93
4.1.	The framework "Virtual Fly Ear"	93
4.2.	Two-state model.....	95
4.3.	Simple harmonic oscillator with floating joint versus 2-state model	96

4.4. Two-state model with floating joint or with nonlinear parallel stiffness versus 2-state model	96
4.5. Four-state model versus 2-state model	97
4.6. Active process by energy flux	97
4.7. Outlook	98
5. Abbreviations	99
6. Literature	101
Appendix A. Definition of continuous Fourier transform and discrete Fourier transform	113
Appendix B. Result of the energy flux analysis for fly 2 and fly 3	114
B.1. Fly 2 (Canton-S)	114
B.2. Fly 2 (Canton-S)	115
Appendix C. Fit parameters used in this thesis	116
C.1. Two-state model	116
C.2. Simple harmonic oscillator model with floating joint	116
C.3. Two-state model with floating joint	116
C.4. Two-state model with nonlinear parallel stiffness	116
C.5. Four-state model	117
Appendix D. LDV Setup for sound stimulation	118
Appendix E. Table of Figures	119
Acknowledgement	122
Curriculum vitae	123

1. Introduction

1.1. Mechanosensation

Mechanosensation relies on the transduction of mechanical stimuli into neuronal impulses. It comprises the sense of touch and also proprioception and hearing. In contrast to sight, smell and taste, relatively little is known about the molecular machineries that mediate the mechanotransduction. However, it is already clear that important aspects are conserved from *Caenorhabditis elegans* to humans. Because of the advantages including a sequenced genome and the ability to conduct electrophysiological recording from mechanoreceptor neurons, *Drosophila melanogaster* has taken a well placed position to make contributions to mechanotransduction studies. Even human geneticists expect that studies on *Drosophila* will provide a new source of candidate genes which with their human homologues can be examined for roles in mechanosensory development, function and disease.

Hearing is a specialized form of the mechanosensation. Not all animals that can sense mechanical stimuli are able to hear. Hearing of an animal depends on whether it can behaviorally respond to biological relevant sound stimuli following the processing flow:

Sound stimuli → detected by sound receiver → transduced in sensory organ → processed and encoded by CNS → effect or initiate corresponding behavior.

In *Drosophila*, evidence for hearing and the corresponding mating behavior (courtship songs) emerged already in late of 50's and early 60's last century [1-3].

In this thesis, it will be focused on the study of hearing with the model organism *Drosophila*.

Hearing in *Drosophila*

1.2. Hearing in *Drosophila*

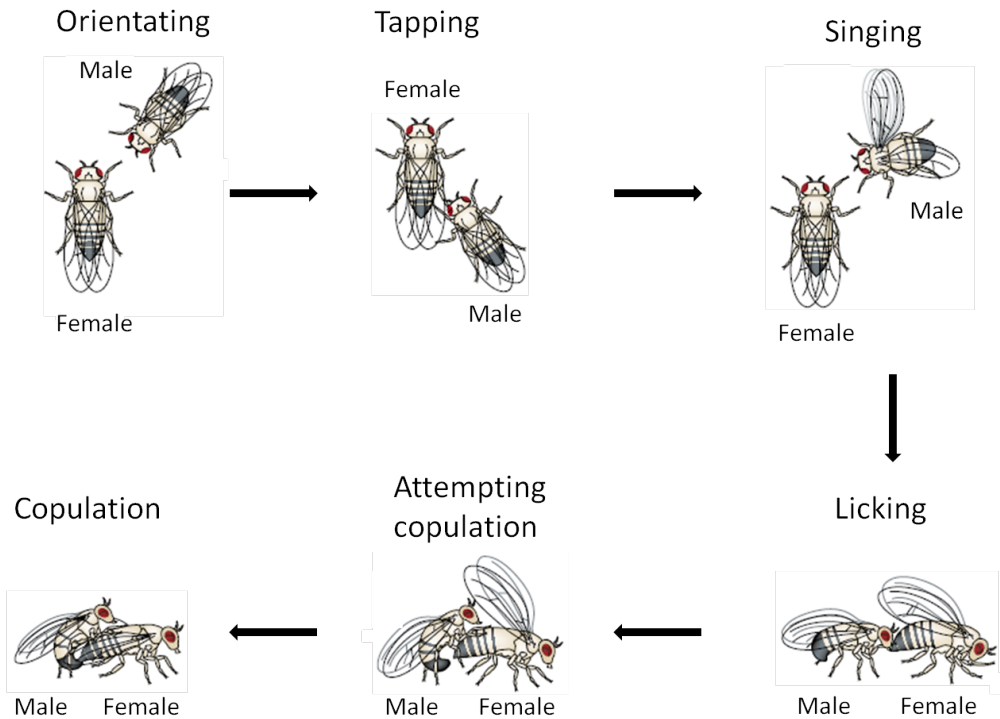


Figure 1: Sequence of courtship of *Drosophila melanogaster*

The 6 steps of the mating behavior of *Drosophila melanogaster*: 1. Orientating, 2. Tapping, 3. Singing, 4. Licking, 5. Attempting copulation and, 6. Copulation. (Modified after [4])

The studies on hearing in *Drosophila* were initiated by the discovery of the flies' communication with courtship songs [1-3, 5-7]. In addition to visual, olfactory and gustatory cues, auditory cues are important for *Drosophila* mating behavior [7] (Figure 1). During courtship, male flies flap one of their wings generating trains of sound pulses that are detected by the females. Two kinds of courtship songs can be distinguished: short sound pulses that are delivered at a rate of ca 30 pulses per second [8] and sine songs produced by continuous vibration of the wing [8, 9]. Both song types have a dominant frequency of ca 150-200 Hz and are believed to serve different roles in mating [10]: the sine songs prime the female prior to courtship and the pulse songs act as a final trigger and also increase the activity of nearby males [9, 11, 12]. As a part of the multisensory communication system, acoustic courtship song serves sex and species recognition [13, 14] and provides information about male quality and reproductivity.

1.3. Anatomy of the fly's ear

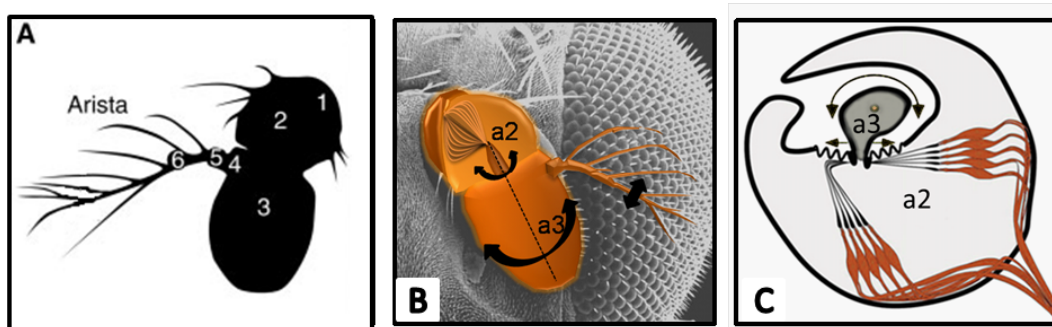


Figure 2: Antennal hearing organ of *Drosophila*

(A) Sketch of the antenna depicting six segments. Segments 3-6 form the sound receiver, vibrations of which are picked up by Johnston's organ, which is housed in Segment 2. (B) Frontal view of the left part of *Drosophila* head, second antennal segment (a2) and third antennal segment are shown. Direction of the movement of the 3rd segment and its extension are indicated by black arrows. (C) Sketch of a cross section through the 2nd segment shows the direct connection of the 3rd segment (a3) to the neurons in the 2nd segment and the relative movements depicted by black arrows.

Anatomically, the *Drosophila* antenna is composed of six segments (a1-a6) (Figure 2 A and B): 3 three large basal segments: the scape (first segment; a1), the pedicel (second segment; a2), the funiculus (third segment; a3), and two small segments residing on the funiculus (a4 and a5) connected with a feather-like extension named arista (a6) [15]. Only the 1st segment houses muscles, allowing for active movements of the entire antenna. The 2nd segment houses a chordotonal stretch-receptor organ, Johnston's organ (JO). The 3rd segment is flexibly suspended in the 2nd segment via an antennal joint [16] (Figure 2C). Segments a3-a6 are stiffly coupled together and mediate the reception of sound as a rigid body, which is named as arista [16, 17]. When stimulated acoustically, the distal segments (a3-a6) sympathetically twist back and forth about the longitudinal axis of a3 (Figure 2B and C). These movements are directly coupled to, and picked up by the primary mechanosensory neurons of Johnston's organ.

Mechanics of *Drosophila* sound receiver

Johnston's organ is composed of ca. 200 chordotonal sensilla (scolopidia). Each of these sensilla consists of two to three sensory neurons and several accessory cells (Figure 3) [18, 19].

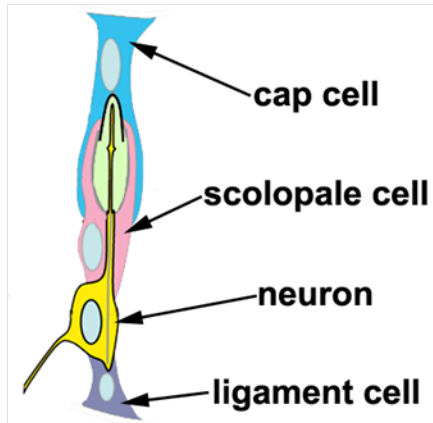


Figure 3: Sketch of the chordotonal organ

Each chordotonal organ is composed of two to three neurons (not shown in the figure) and three different types of accessory cells: the cap cell (and the extracellular cap depicted as bold black line), scolopale cell, and ligament cell. (Modified after [20])

Chordotonal sensory neurons are bipolar and monodentritic, bearing a single distal ciliated dendrite and a proximal axon that conveys neuronal impulses to the CNS [21]. The ciliated dendrite of the sensory neurons is directly connected to the antennal sound receiver via an extracellular cap. The neurons of Johnston's organ are arranged like a bowl [22]. Cross-sections through the organ show that the neurons form two populations that are symmetrically connected to the posterior and anterior sides of the sound receiver [16, 22]. Recordings of intracellular calcium signals in neurons of Johnston's organ revealed that these two neural populations are alternatively activated when the sound receiver twists back and forth [22]. The neurons are endowed with mechanically gated transduction channels [23-25]. Because of the direct connection between these channels and the sound receiver, the mechanics of the sound receiver can be used to probe the auditory transduction events.

1.4. Mechanics of *Drosophila* sound receiver

The mechanics of the fly's antennal sound receiver can be assessed noninvasively by measuring its vibration via a laser-Doppler Vibrometer (LDV) ([26] and section 2.3). Because the entire sound receiver (a3-a6) moves as a rigid body, monitoring the vibration at one point betrays the frequency characteristics of the whole antennal sound receiver [16, 17]. In the absence of acoustic stimulation, the

sound receiver twitches erratically back and forth due to thermal bombardment by air particles in Brownian motion [27, 28]. The power spectra of the receiver's free fluctuation closely resemble those of a moderately damped harmonic oscillator, whose resonance frequency approximately corresponds to the dominant frequency of the fly's courtship songs (ca. 150-200 Hz) [27]. When the sound receiver is stimulated with a pure tone at a much higher frequency than the dominant frequency of the courtship songs, the amplitude of the vibration response linearly scales with the intensity of the pure tone [29]. This linear behavior coincides with that of a single harmonic oscillator. However, when the frequency of the stimulating pure tone approaches the resonance frequency of the sound receiver, this linear relation breaks down: In the near of the resonance frequency, the sound receiver displays the compressive nonlinearity, which is one of the four characteristics defining the cochlear amplifier [30, 31]. Due to this compressive nonlinearity, a wide range of stimulus intensities is condensed into a narrow range of response amplitudes and the sensitivity to faint sounds is increased by a factor of ca. 10 [29, 32, 33] (Figure 4C, green trace). With the compressive nonlinearity the sound receiver achieves an increase in the dynamic range with the by-product of reduced intensity resolution. When the fly's physiological condition deteriorates, this gain in sensitivity become much larger, reaching factors of up to 100 [29] (Figure 4, red traces). Along with this excess gain the oscillation becomes larger, resulting in the sharp peak in the power spectrum [28, 29, 34]. When the flies die or are anesthetized by CO₂, the fluctuation amplitude drops and the peak in the power spectrum and the nonlinearity disappear. The sound receiver then behaves linearly throughout the intensity range [27, 28] (Figure 4, blue traces). When the receiver is stimulated by different intensities of sound, the mechanical frequency response varies. This change results in a down shift of resonance frequency from ca. 800 Hz to 200 Hz, as the stimulus intensity declines [17, 27, 35]. This suggests that the sound receiver tunes in on the courtship songs when the songs are faint.

Active amplification

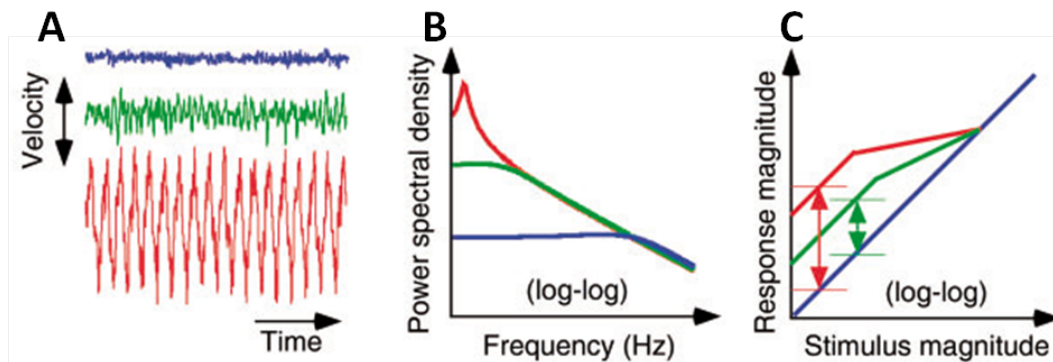


Figure 4: Mechanical properties of sound receiver

(A) Time traces of displacement of sound receiver during free fluctuation. Fluctuations are shown for dead fly (blue), live wild type fly (green), and live wild type fly in deteriorative physiological condition. (B) Respective power spectra of fluctuation are shown. (C) Respective intensity characteristics of the receiver are shown. The respective sensitivity gains at low stimulus intensities are depicted by arrows. (Adapted after [36])

1.5. Active amplification

As mentioned in the section 1.4, the fly's sound receiver displays a compressive nonlinearity that is frequency specific and can oscillate spontaneously in the absence of sound stimulation. Both these properties can be found in vertebrate auditory systems, where they are ascribed to the cochlear amplifier [37]. The concept of the cochlear amplifier posits that the vertebrate cochlea is endowed with a force-generating process that feeds mechanical energy into sound-induced basilar membrane motion [38-41]. Four key characteristics define the cochlear amplifier [30, 39]: (1) compressive nonlinearity, (2) frequency specific amplification, (3) active amplification / power gain, and (4) self sustained oscillations. An existing active amplifier must exhibit the power gain, i.e. more energy must be dissipated by the amplifier than is originally fed in. A rigorous way to test for power gain is to demonstrate the violation of the fundamental principle in equilibrium thermal dynamics, the equipartition or the fluctuation-dissipation theorem. Using this method, the sensory hair-bundles of bullfrog's inner hair cells and the fly's sound receiver have been shown to violate the fluctuation-dissipation theorem (Figure 5) [42-44], demonstrating that they are active and exhibit power gain. In *Drosophila*, the total energy that is pumped into

the vibration of the antennal sound receiver by the active process has been estimated by comparing the energy of receiver's free fluctuation between dead and live flies [28]. This active energy has been found to correspond to ca. 20zJ.

1.6. Motility of sound receptors of *Drosophila*

By monitoring and analyzing the mechanics of the antennal sound receiver in *Drosophila* mutants, the cellular basis of the active process of the fly's auditory system has been traced down to the chordotonal sensory neurons of Johnston's organ. Fly mutants with hearing defects have been identified in behavioral screens [8, 45]. One of the respective genes is *no-mechanoreceptor-potential A (nompA)*. Flies carrying null alleles of *nompA* fail to produce the

mechanical evoked electrical response in the tactile bristles [46] and, as well, lack the sound evoked electrical response in the antennal nerves [46, 47]. The gene *nompA*, reportedly, encodes an extracellular linker protein, which is expressed in the cap (Figure 3) that connects the sensory cilia of the neurons of Johnston's organ to the antennal sound receiver [46]. In *nompA* nulls, the attachment is broken and the neurons in Johnston's organ are disconnected from the sound receiver [46]. Along with this anatomical defect, the compressive nonlinear behavior in the mechanics of the sound receiver and active amplification are lost, which suggest that the source of the active mechanical energy are in the sensory

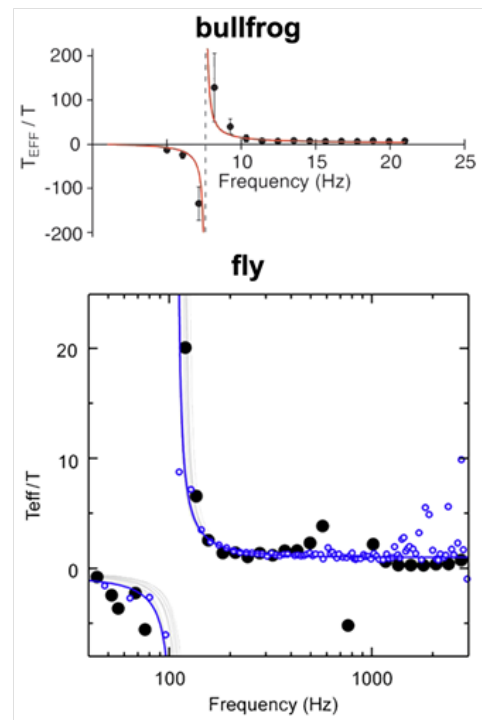


Figure 5: Violation of the fluctuation-dissipation theorem demonstrates the active process

At the thermal equilibrium the ratio between the effective temperature and the ambient temperature is one. The hair bundle of the bullfrog (upper panel) and the fly's sound receiver (lower panel) violate the fluctuation-dissipation theorem at 8 Hz and 120 Hz, respectively, demonstrating the active property. [42, 44]

Molecular mechanisms of the sensory neurons

neurons of Johnston's organ [27, 28]. Furthermore, evidences that *insensitive-larva B (tilB)* and *Beethoven (btv)* mutants lost the receiver's nonlinearity and activity supported the theory that the neurons of Johnston's organ generate motions and actively pump energy into the vibrations of the antennal sound receiver [27, 28]. Mutants in both *tilB* and *btv* affect the structure of the sensory cilia of the neurons of Johnston's organ. Anatomically, the *btv* mutants show defects in the ciliary dilation (Figure 3) [47]. The *tilB* mutants fail to develop ciliary dynein arms and to produce motile sperm [47]. This combination suggests that the force-generating machinery is located in the proximal region of the sensory cilia of the neurons of Johnston's organ, because the ciliary dynein arms have been shown only to exist in this region [48].

1.7. Molecular mechanisms of the sensory neurons

Hair cells display two kinds of active motions: prestin-mediated somatic electromotility and the active hair bundle motility that is powered by the molecular machinery for auditory transduction [40, 41, 49]. Somatic electromotility seems restricted to mammalian outer hair cells, while active hair bundle motility is more widespread to characterize the hair cells of both mammalian and non-mammalian vertebrates. As explained in the preceding subsections, the chordotonal sensory neurons in *Drosophila* demonstrate similarity to the hair cells in vertebrates: they are motile and play both the transducing and the actuating roles. According to the *Drosophila* genome sequence, a prestin ortholog is expressed in Johnston's organ [50], yet more evidences suggest that the auditory transduction machinery promotes the active amplification in the sensory neurons of Johnston's organ.

1.7.1 Candidate transducer is required for the active amplification

By analyzing the auditory mechanics in flies carrying mutations in transient receptor potential family (TRP-family) ion channels, it has been shown that active amplification in fly hearing requires candidate transducer components. In *Drosophila*, three members of the TRP-family have been identified that are expressed in Johnston's organ and are involved in hearing in flies: *No-mechanoreceptor-potential C (NompC)* (= TRPN1) and the TRPVs, *Nanchung (Nan)* and *Inactive (Iav)*. *Nan* and *Iav* are deemed to form a heteromultimeric Nan-Iav channel [51-53]. Investigations of *Drosophila* tactile bristles have shown that NompC might be a transduction channel [54]. NompC harbors a predicted pore region and a N-terminal ankyrin spring, and therefore seems structurally qualified for being a mechanically gated (gating-spring) ion channel as implicated in auditory transduction [25, 55-58]. Furthermore, NompC is required for the mechanoreceptors in *Drosophila* and nematode [51, 59-61] and is essential for hearing in drosophila [62]. Based on these evidences, it has been speculated that NompC could also be one of the transduction channels for hearing [51, 63-66]. Yet, loss of NompC does not turn out the sound-evoked electric potentials in nerves completely. Remnant potentials persist in NompC mutants [47]. On the other hand, the potentials are completely abolished by null alleles of *nan* and *iav*, which could be the evidence that it is the TRPV which forms the transduction channel for hearing [52,

Figure 6: Model of TRP-channel function in *Drosophila* ear

Nan-Iav acts downstream of NompC in auditory pathway. The feedback amplification requires NompC and is controlled by Nan-Iav. A NompC independent mechanotransduction channel (X) is responsible for remnant compound action potentials (CAPs) in *nompC* mutants. Disrupting Nan-Iav breaks the signal propagation. After [36]

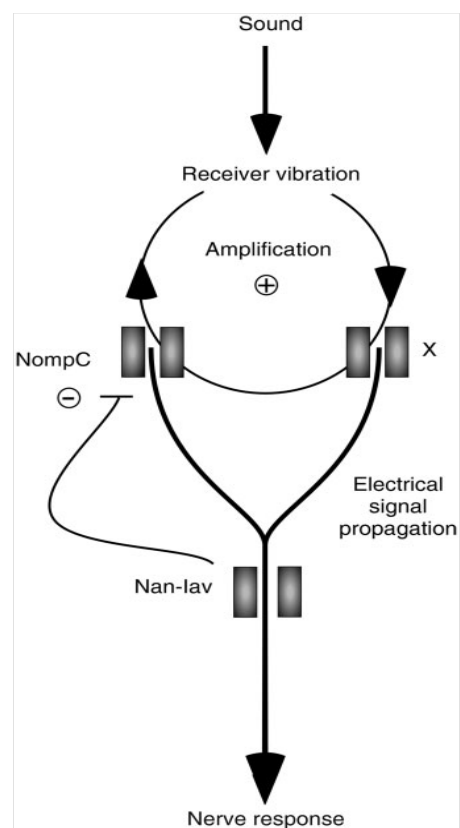


Figure 6: Model of TRP-channel function in *Drosophila* ear

Nan-Iav acts downstream of NompC in auditory pathway. The feedback amplification requires NompC and is controlled by Nan-Iav. A NompC independent mechanotransduction channel (X) is responsible for remnant compound action potentials (CAPs) in *nompC* mutants. Disrupting Nan-Iav breaks the signal propagation. After [36]

Molecular mechanisms of the sensory neurons

53]. However, disrupting the NompC channels abolishes active amplification, which is facilitated by the disruption of Nan-Iav [29]. Epistatic analysis indicates that Nan-Iav acts downstream of NompC in auditory pathway, facilitating active amplification in a NompC-dependent way (Figure 6). According to this theory, both NompC-dependent and NompC-independent transduction mechanisms exist and NompC but not Nan-Iav might be the transduction channel. The remnant action potentials in *nompC* mutants can be ascribed to the NompC-independent way. This notion was supported by the finding that neurons in Johnston's organ are grouped for 2 different tasks: sound-detection and gravity/wind-detection [67, 68].

As these genetic studies have shown that the active amplification in the auditory system of *Drosophila* requires components of candidate transduction channels, biophysical modeling demonstrated that the active amplification in fly's ear can be explained by transducer-based force generation [44].

1.7.2 Transducer-based model of *Drosophila* hearing organ

Mechanical signatures that are consistent with a direct mechanotransducer gating have been identified in fly's ear [23]. These signatures conform to those of the gating-spring model of vertebrate auditory transduction [23]. The gating-spring model describes mechanotransduction in hair cells [69-71]. According to this model, deflections of hair bundles in vertebrate hair cells directly gate mechano-electrical transduction channels (MET-channels). The MET-channels are attached to elastic elements, the gating-springs. This channel-spring-complex is serially coupled to adaptation motors (Figure 7). Forces acting on the channel (gate) are conducted by the spring. According to this model, the extension of the gating-spring and the open probability of the channel alter, when the force acting on the gating-spring changes. The channels operate in parallel and each of these channels is assumed to have two states: open or closed. At resting position, the open probability is ca. 0.5. When the transducer is actuated by a pulling force, the tension of the spring increases and more channels are opened. In the open state, extracellular ions flow into the sensory cell and interact with the gating spring-

channel-complex, so that the channel gate is closed, which can be ascribed to fast adaptation of the channel. After this closure, the channel gate cannot be reopened for a short time [72-74], followed by a motor driven slow adaptation [71] (Figure 7). This motor driven adaptation reduces the spring tension and restores the open probability of the channel (Figure 7).

To test whether this molecular arrangement of gating spring model also explains the active amplification in the auditory system of *Drosophila*, a biophysical model for the fly's auditory system was devised. In this model, transducer modules as for the vertebrate auditory hair cells coupled to a simple harmonic oscillator that represents the fly's antennal sound receiver [44] (Figure 8). In accordance with the anatomy of the *Drosophila* hearing organ (section 1.3), two opposing populations of transducer modules are arranged symmetrically. The harmonic oscillator twists about the a2/a3 joint (Figure 8). Mathematically, the model is described by a set of coupled differential equations. Simulation of this model captures the mechanics of the fly's antennal sound receiver including its response to force, its free fluctuation, and its frequency characteristics.

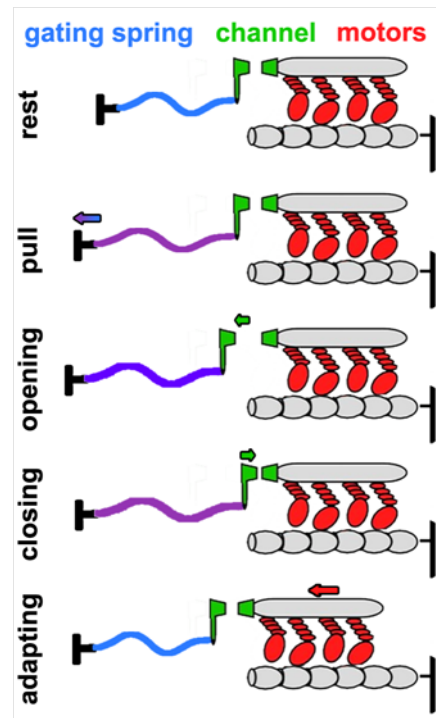


Figure 7: Gating-spring model and activation of the MET-channel

The gating-spring, channel and adaptation motors are connected in series. At resting position, the spring is not extended, open probability of the channels is ca. 0.5. When actuated, the tension of the spring and the open probability alter. When fully adapted, the spring tension and open probability of the channels are restored. Colors of the spring denote different tension of the gating spring. After [97]

Molecular mechanisms of the sensory neurons

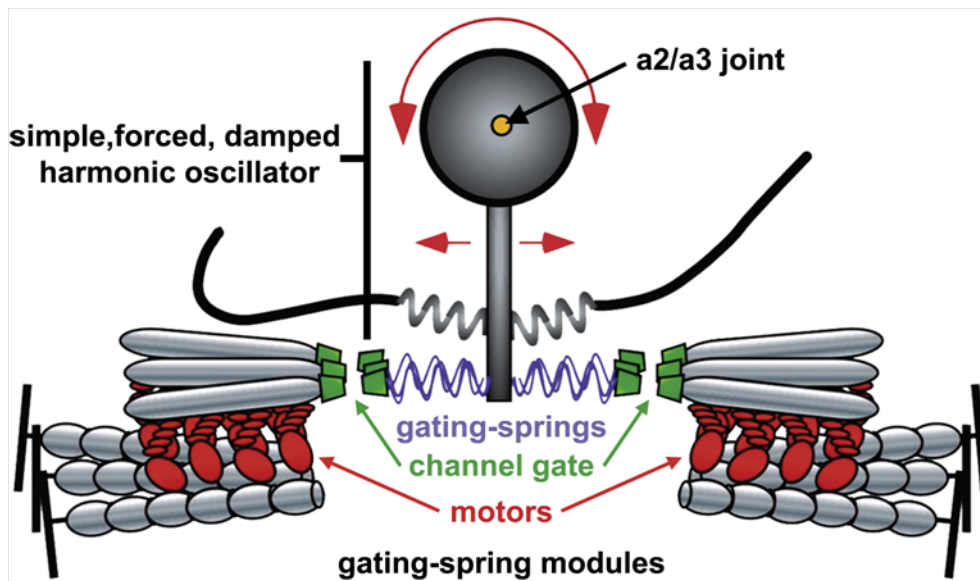


Figure 8: Model of Drosophila hearing organ

In accordance with the anatomy of the fly's hearing organ, the hair cell-like transducer modules are symmetrically arranged in to opposing populations and coupled with a simple harmonic oscillator that represents the antennal sound receiver of fly. When the sound receiver is actuated, the harmonic oscillator twists about the a2/a3 joint, and the transducer modules in both sides are stretched and compressed, respectively. After [44]

Comparing simulated and measured responses revealed that this model suffices to quantitatively reproduce the active properties of the fly's sound receiver and properties of the sound-evoked potentials in the antennal nerve [25, 44]. Analysis with this model revealed that active amplification in the fly's auditory system arises from the interplay between the transduction channels and associated adaptation motors [44], analogous to active hair bundle motions.

1.8. Aim of this study

The biophysical model for fly's hearing organ mentioned in the preceding subsections has helped to understand and explain the active process in the neurons of Johnston's organ, linking the macroscopic measurements to parameters on molecular level, and providing valuable means for analyzing mechanics of fly's antennal sound receiver and the auditory functions of fly's ear. However, running the models and simulations is highly time-consuming, preventing a systematic analysis of auditory function in a large number of flies. During my doctoral thesis I have established a computational framework, the "Virtual Fly Ear" that facilitates the analysis via models, providing the means to systematically compare this function between hearing-impaired mutants and respective controls. Furthermore, multiple models: (1) two-state model, (2) simple harmonic oscillator model with floating joint, (3) two-state model with floating joint, (4) two-state model with nonlinear parallel stiffness, and (5) four-state model are implemented in this framework. Based on these models, the hearing mechanics of mutant flies can be explained in a more specific way. Comparing the model's fit results may help to identify and verify the defects in the auditory machinery. In addition to the modeling, a novel method for analyzing auditory function is presented that allows to quantify power fluxes in the ear

Aim of this study

2. Material and methods

2.1. Fly lines

Table 1 of mutants/wide types used during the thesis

fly	Full genotype
Canton-S (CS)	wild-type
NompA	w;cn bw nompA[2]/ Cy P{Ubi-GFP},
TilB	yw tilB[2]/FM4
NompC	;NompC(3)/CyO;

2.2. Fly preparation for mechanical measurement

Movements of the 3rd antennal segment (funicle) were measured at the tip of the

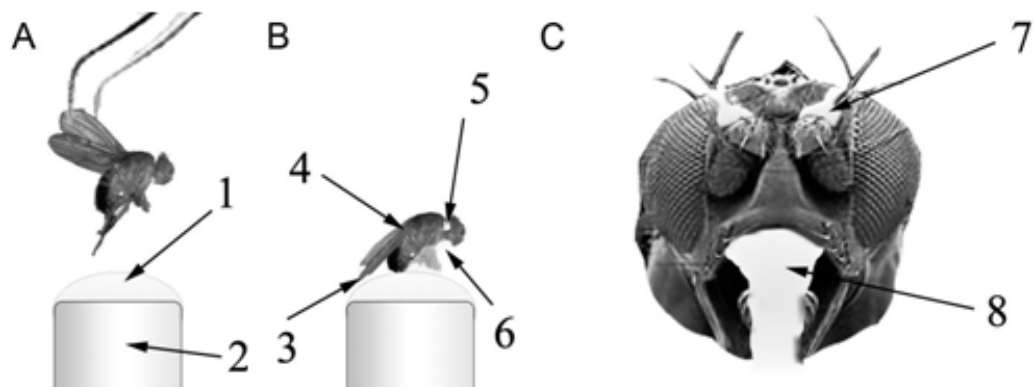


Figure 9: Fixation of the fly

Flies were anesthetized with CO₂. Then they were taken by the wings and affixed with their legs (1, beeswax/paraffin) on top of a Teflon rod (2). The head (5), the wings (3), the halteres (4), and the thorax (6) were stabilized with the wax. The pedicels (7) and the mouthparts (8) were affixed to the head by dental glue. After [97]

antennal arista. Environmental vibrations were canceled by the use of an air table. Unwanted animal movements were prevented by a thorough stabilization of the animal using wax and dental glue. The only possible movement was the rotation of the 3rd segment about its longitudinal axis relative to the 2nd segment (Figure 2). Techniques were adapted and refined according to references of [23, 28, 29].

Mechanical Measurements

2.3. Mechanical Measurements

2.3.1 Free fluctuations of the sound receiver

In absence of external force, the fly's sound receivers fluctuate due to the Brownian motion of air particles and the active movements of JO neurons. The LDV was used to measure the free fluctuations by focusing the laser beam on the tip of the arista. The LDV allows precise measurements of the velocity of the sound receiver on nm/s level. The velocities of the fluctuation were recorded as time trace with a sampling rate of 8192 Hz. To analyze the fluctuation, a python script (psd_plot.py) was used, which converts the velocity time trace $\dot{X}(t)$ into a displacement time trace $X(t) = \int \dot{X}(t)dt$. The displacement power spectral density (PSD) was calculated with the displacement time trace by applying the Wiener-Khinchin theorem [75]. (For detail of definitions for FFT please see Appendix A.) The LDV software allows for the evaluation of the one sided PSD as well. To exclude out-of-focus data, all fluctuation data in the thesis was calculated with own python scripts, and the LDV software only serves as control.

Individual best frequencies (iBF) of each sound receiver were determinate from velocity spectra obtained with the software.

2.3.2 Sound-induced intensity characteristic of the sound receiver

To assess the mechanical response of the fly's sound receiver in to acoustic stimuli, pure tones at the iBF with different amplitudes (ranging over 96 dB) were broadcast via with a loudspeaker/HiFi-system. Resulting stimulus practical velocities at the animal's position were measured by an Emkay NR 3158 pressure-gradient microphone as described [27]. The time trace of the displacement of the tip of the arista was measured with a Polytec PSV-400 Laser Doppler Vibrometer equipped with an OFV-700 close-up unit and digitalized at a rate of 12.1 kHz. The phase-locked displacement amplitude at the stimulus frequency was measured as Fourier amplitude, $\tilde{X}(\nu)$. CAPs were recorded with an electrolytically tapered tungsten electrode inserted between the 1st antennal segment and the head. A non-differential electrode for CAP recording was placed in the thorax. The CAP amplitudes were read at twice the stimulus frequency because of the frequency-

doubling of the CAPs produced by JO [23]. The individual CAP response was normalized($\frac{V-V_{min}}{V_{max}-V_{min}}$), where V denotes the voltage recorded by the electrode. The normalized CAP signals were fitted with a Hill-equation with 4 free parameters: y_{min} , y_{max} , m and n . The fit equation reads

$$f(x) = y_{min} + \frac{y_{max}-y_{min}}{1+\left|\frac{x}{m}\right|^n},$$

where y_{min} is the minimum, y_{max} the maximum, m a constant defining intensity at half-maximal response and n a measure of the dynamic phase [76].

Thresholds were defined as the sound particle velocity/antennal displacement amplitude at which 5% of the $y_{max} - y_{min}$ was reached. The dynamic range was defined as 5%-95% of the $y_{max} - y_{min}$.

2.3.3 Passive receiver mechanics

To determine the passive mechanical properties of the fly's antennal receiver, animals were anesthetized with CO_2 ([14, 27]). The PSD of the receiver's passive fluctuations were fitted with a simple harmonic oscillator (SHO) function. The elastic properties of the JO and the antennal joint are well described by the constants of the harmonic oscillator. A driven damped harmonic oscillator can be defined by

$$m\ddot{x} + \gamma\dot{x} + Kx = F, \quad (1)$$

where m is the mass, γ is the friction constant and K is the stiffness constant, x and F are displacement and external force, respectively.

In the absence of external stimulation, the sound receiver is driven by thermal force $F = \eta$. According to the equipartition theorem of the fluctuation-dissipation theorem, the thermal force in the near of the thermal equilibrium [42] can be defined by

$$\langle \eta(t)\eta(0) \rangle = 2k_B T \gamma \delta(t),$$

where k_B denotes the Boltzmann constant, T the ambient temperature, δ the delta function and the brackets the autocorrelation operator.

Mechanical Measurements

On the basis of the definition for the harmonic oscillator equation 1, the linear response function can be deduced as

$$\tilde{\chi}(\omega) = \frac{\tilde{X}(\omega)}{\tilde{F}(\omega)} = \frac{1}{-m\omega^2 + i\omega\gamma + k}. \quad (2)$$

And by replacing the driven force in equation 1 with $\tilde{F}(\omega) = \tilde{\eta}(\omega)$, we obtain

$$\tilde{X}(\omega) = \frac{\tilde{\eta}(\omega)}{-m\omega^2 + i\omega\gamma + k}. \quad (3)$$

Knowing the Fourier transformed displacement as a function of frequency $\tilde{X}(\omega)$, the power spectral density can be deduced by applying the Wiener-Khinchin theorem:

$$\tilde{S}(\omega) = \frac{2k_B T \gamma}{m^2 \left((\omega^2 - \omega_0^2)^2 + \left(\omega \frac{\omega_0}{Q} \right)^2 \right)} = 2k_B T \gamma |\tilde{\chi}(\omega)|^2, \quad (4)$$

where Q is the quality factor and equals to $\frac{\omega_0 m}{\gamma}$ and ω_0 is the natural angular frequency of undamped system and equals to $\sqrt{K/m}$.

According to the definition of discrete Fourier transform (Appendix A) the discrete form of equation 4 reads

$$\frac{X^2(\omega)}{\Delta\omega} = \frac{2k_B T \gamma}{m^2 \left((\omega^2 - \omega_0^2)^2 + \left(\omega \frac{\omega_0}{Q} \right)^2 \right)} \quad (5)$$

and

$$\frac{X^2(\omega)}{\Delta\omega} = 2k_B T \gamma |\tilde{\chi}(\omega)|^2, \quad (6)$$

where the $X^2(\omega)$ is the squared Fourier transformed amplitude of measured displacement.

Integrating the function (equation 5) for frequencies between zero and infinity yields the fluctuation power, i.e. the mean-square displacement, $\langle X^2 \rangle$, of the

receiver's fluctuations [42]. Fits were performed by an automatic fit program using the Nelder-Mead algorithm [77], which is called Downhill-Simplex-Algorithms as well.

2.3.4 Sound-induced vibrations

External stimulus forces can entrain active receiver vibrations, suggesting that the active energy that is dissipated by the receiver might redistribute in the presence of sound. To investigate how sound alters dissipation, the receiver was exposed to tones at its individual best frequency and the tone intensity was varied. To separate active and passive components in the receiver's response, responses were measured before and during anesthetization with CO_2 .

2.3.4.1 Fitting sound-induced vibrations

When exposed to tones, the receivers of anesthetized flies vibrate in response to the external stimuli and, in addition, fluctuate due to thermal and background noise. By fitting the PSD of the receiver with equation 5 while neglecting the stimulus frequency and higher harmonics, we isolated its thermal fluctuations from its tone-induced vibrations and background noise. By re-adding its vibration response at the stimulus frequency to the resulting fit-function, the PSD of its vibrations was reconstructed, yielding a "clean" PSD that does not include higher harmonics and background noise.

The model (equation 5) describes neither the peak amplitudes nor the amplitudes at the stimulus frequency's harmonics. To simplify the calculation of the PSD of such a stimulated fluctuation, we divided the PSD into a base spectrum (spectrum without the amplitudes at the stimulus frequency and its harmonics) for the thermal fluctuation and background noise and the peak amplitude at stimulus frequency. The amplitudes at the harmonics of the stimulus frequency have only minor impact on the energy distribution, thus they are not included in the calculations.

Mechanical Measurements

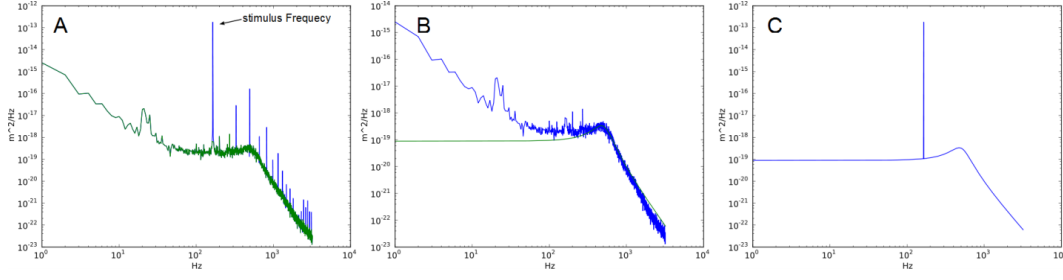


Figure 10 Fitting stimulated PSD

Illustration of fitting PSD of sound induced vibration. After the Peak amplitude at stimulus frequency (A, black arrow) and the higher harmonics were removed (A blue line before and green line after). The base spectrum (B, blue line) was fit to the model (equation 5). Subsequently, the peak amplitude (A, black arrow) was re-added to the fit curve for reconstruction (C).

2.3.4.2 Estimating the force exerted by sound stimulation

The passive receiver mechanics of anesthetized flies can be deduced by fitting model of simple harmonic oscillator (equation 5) to the corresponding receiver fluctuations. Because the fluctuations result from thermal bombardment and the thermal driving force η_0 satisfies

$$\langle \eta_0(t' + t)\eta(t') \rangle = D_0 \delta(t), \quad (7)$$

where the angle bracket denotes the autocorrelation function, and $D_0 = 2k_B T \gamma$, the Fourier amplitude of the force can be written as

$$\frac{F^2}{\Delta \nu} = 2k_B T \gamma. \quad (8)$$

Because the system is linear, the Fourier amplitude of the force exerted by a tone stimulus at the frequency of stimulation can be directly deduced from the Fourier amplitude of the receiver's displacement at the corresponding frequency if its mechanics are known. Fitting the receiver's vibrations with simple harmonic oscillator (equation 5) provides information about this mechanics, so the Fourier amplitude of the force exerted by the stimulus can be deduced:

For a specific frequency ν , we thus obtain

$$\frac{|X_{0v}|^2}{\Delta v} = D_0 \cdot |\tilde{\chi}(v)|^2. \quad (9)$$

The linear response function (LRF) is defined as

$$\tilde{\chi}(v) = \frac{\tilde{X}(v)}{\tilde{F}(v)}, \quad (10)$$

where $\tilde{X}(v)$ denotes the Fourier transformed displacement and $\tilde{F}(v)$ the Fourier transformed stimulus.

When the sound receiver is additionally driven with white noise so that force it experiences is $D_T = n \cdot D_0$, the discrete form the of the PSD is given by

$$\frac{|X_{Tv}|^2}{\Delta v} = D_T \cdot |\tilde{\chi}(v)|^2. \quad (11)$$

Therefore

$$\frac{|X_{0v}|^2}{|X_{Tv}|^2} = \frac{D_0}{D_T}. \quad (12)$$

Combining equations 9-11, the force amplitude is

$$|F_0| = \sqrt{\Delta v \cdot D_0}, |F_T| = \sqrt{\Delta v \cdot D_T}, \quad (13), (14)$$

where $|F_0|$ and $|F_T|$ have the unit N. Substituting D_0 and D_T in the equation 12 with the equations 13 and 14, we obtain the following equation:

$$|F_T| = \sqrt{2k_B T \Delta v \cdot \frac{|X_{Tv}|^2}{|X_{0v}|^2}}. \quad (15)$$

Equation15 is used to deduce the force exerted by pure tones with the unit N.

Mechanical Measurements

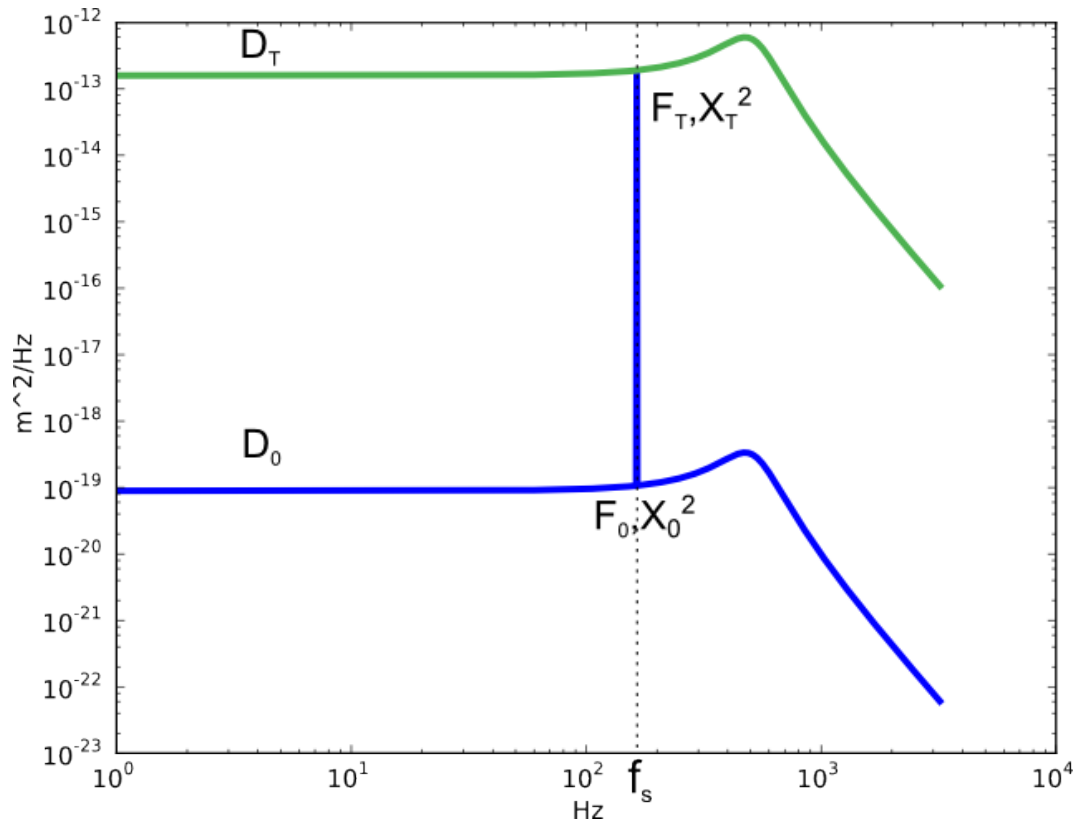


Figure 11 Illustration of force estimation for the sound induced stimulation

The PSD of a sound receiver actuated by pure tone stimulus with frequency f_s , (Blue line), which is described by the thermal constant D_0 . The PSD described by constant D_T (green line) has the same amplitude as the peak amplitude of the stimulated PSD (blue) at the frequency f_s .

2.3.5 Mechanical & nerve response to step stimulus

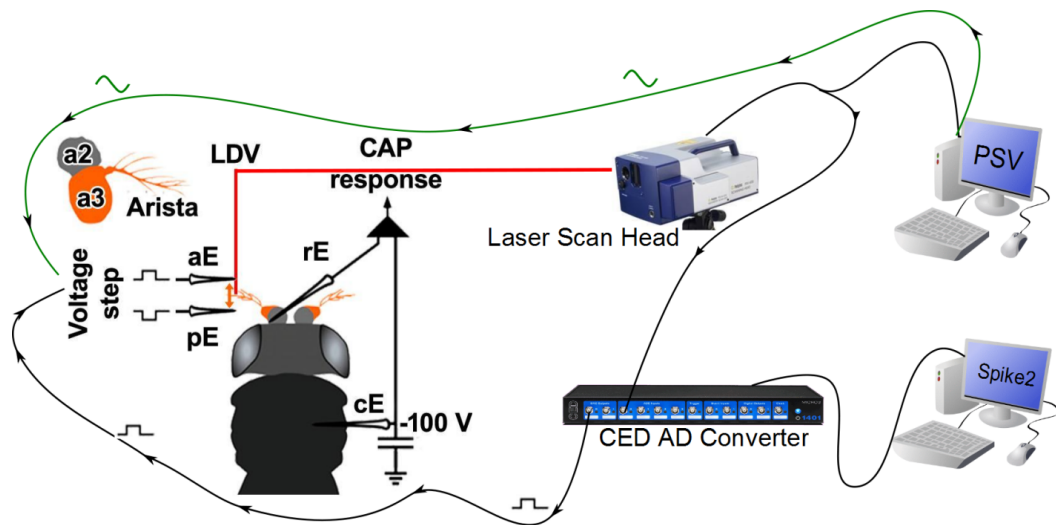


Figure 12 Setup for electrostatic measurements

Two bipolar electrodes were positioned to both anterior (aE) and posterior (pE) to the arista. The fly was charged with -100 V above ground by a charging/indifferent electrode (cE). Mechanical responses (displacements) of the arista were recorded by LDV. A recording electrode (rE) allowed for a simultaneously record of the nerve responses (CAP). Modified from [23]. The laser scan head and AD converter were connected for the input and output of the signal. Measurement data were monitored and analyzed online with connected computers. Pictures of laser scan head and CED AD converter are adapted from the webpage of Polytec and Cambridge Electronic Design, respectively.

The gating compliance and the parallel stiffness of the antennal sound receivers can be deduced by measurements of mechanical responses to step forces to the receivers. The step forces were generated electrostatically so that a non-touched stimulus can be achieved. Similar technique has been described by Dr. Jörg Albert [23]. This technique was adapted and improved by introducing another electrostatic probe, so that electrostatic actuation could come from both anterior and posterior side of the antennal receiver (Figure 12), and the pushing and pulling forces were much more equal. In addition, the flies were loaded with a static potential of 100 V over ground by an electrode inserted into the thorax. Through the loading, the polarization effects were compensated. These modifications improved the linearity of applied forces in relative to the distance between the sound receiver and the electrodes.

Mechanical Measurements

The bipolar tungsten stereotrodes (WE3ST31.0A5 and WE3ST31.0A10, Micro Probe, Inc.) were used as actuator probes. The probes were aligned to the laser beam axis of LDV optically and positioned to the anterior and posterior sides of the arista equally. During the measurements the probes could be charged up to ± 400 V. This high loading increased the possible forces acting on the sound receiver and allowed more space for the positioning of the electrodes, which contributed the compensation of the quadratic effect between the stimulus voltage and the generated force. To obtain the values of step forces multiple steps were generated and a quadratic fit with equation,

$$Force = f(v) = p_0 + p_1v + p_2v^2,$$

was applied.

To measure the mechanical responses to the step forces 28 digital steps were generated by a script of the Spike2 software. A CED micro3 (Cambridge Electronic Devices, Cambridge, UK) were used for AD conversion at a sampling frequency 13.1 kHz, which is controlled by the software Spike2. As described above the converted voltages/electric fields were experienced by the arista. The laser scan head detected and recorded the motion of the arista, data were monitored and stored by the computer running the software PSV, which controlled the laser scan head. The recorded data were cleaned and analyzed by multiple scripts and programs (see section 2.4).

We distinguished two different kind of stiffness from the measured data: K_{peak} and K_{steady} . K_{steady} Describes only the combined stiffness of the a2/a3 joint and the structures that suspend JO, doesn't describe the mechanical stimulus coupling [24] from the sound receiver to the mechanotransduction channel. Therefore, K_{steady} is constant. K_{peak} describes the gating spring and the dynamic stiffness changes that is based on the opening and closing of the mechanotransduction channels. Thus, K_{peak} isn't constant and depends on the external force, the number of channels, their open probabilities, the gating swing and the energy needed to gate a single channel.

2.3.5.1 Force estimation of electrostatic steps

Theoretically the electric field $E(r)$ at a distance r from the actuator electrode is proportional to the command voltage V_c fed to the electrode. And the force F experienced by the sound receiver depends on the receiver's polarization p . Although we used double bipolar electrodes as actuators to minimize the polarization, minor polarization effect still remained. And this polarization is proportional to the electric field $p \propto E(r)$. This leads to a quadratic relation between command voltage and the force [23].

To obtain the explicit value of force acting on the sound receiver, 28 step stimuli with different V_c were produced. The onset accelerations a_{on} was calculated by the pre-analysis programs. A fit to the following equation was carried out:

$$\frac{F}{m} = a_{on} = \frac{p_1}{m}(v_c - v_0) + \frac{p_2}{m}(v_c^2 - v_0^2),$$

where m = effective mass of the arista,

a_{on} = onset acceleration,

p_1, p_2 = parameters of the quadratic equation,

v_c = command voltage,

v_0 = base voltage.

After the fit, the parameters p_0, p_1, p_2 combined with were v_c used to deduce the external force for the fitting of the models.

Mechanical Measurements

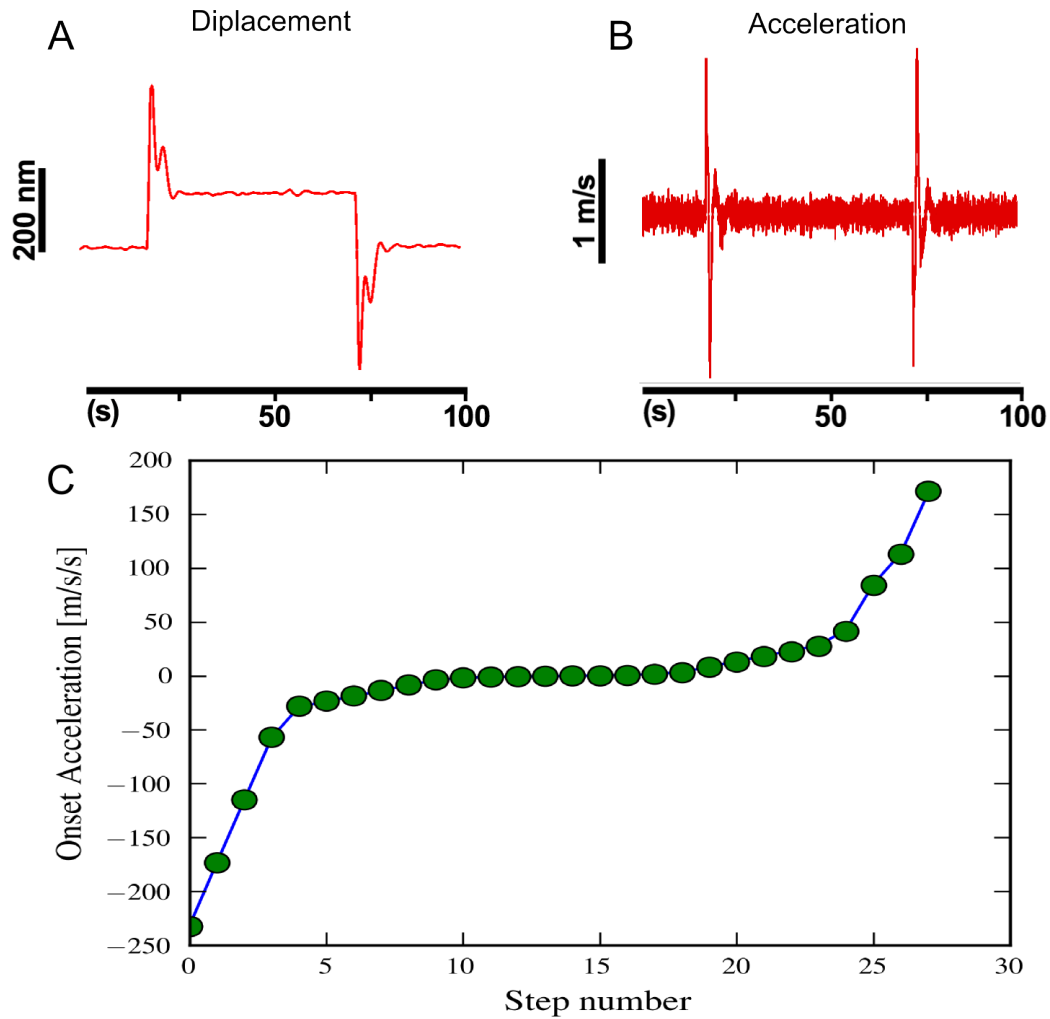


Figure 13 Displacement response and its time trace of acceleration

(A) Illustration of displacement response of step force stimulus. (B) The calculated acceleration. The accelerations of every single step stimulus were plotted in (C) as green dots, and the fit as blue curve. Experimental data provided by Dr. Thomas Effertz.

2.3.6 Receiver's linear response function for weak sinusoidal forcing

To determine the linear response function, defined as $\tilde{\chi}(f) = \tilde{F}(f)/\tilde{X}(f)$, we actuate the sound receiver electrostatically with a multiple-sine stimulus consisting of n sinusoids of identical force amplitude A . For very small stimuli, the linear response function is independent of the forcing amplitude. During the measurement the fly was mounted and positioned between electrodes as described in section 2.3.5 and Figure 12.

Experimentally a voltage sequence generated by script “reizfileproducer.py” was fed to the PSV Scanning Vibrometer Software, which in turn produced the command voltage and therefore the electric field to actuate the receiver (Figure 12 green data stream). The displacement response was recorded by LDV with a sampling rate of 8192 Hz. The recorded data was cleaned and analyzed by further programs.

2.4. Pre-processing of experimental data

The resulting dataset from force steps measurements containing time traces of stimuli, mechanical and nerve responses with duration of 2h were recorded by Spike2 computer. After exporting the data into a smr file the raw data were subsequently processed by C/C++ and python programs. To access the compiled binary smr file a self-made python [78] wrap of “C++ son library” was used, which is provided by the company CED upon request.

The experimental data measured for PSDs and linear response functions were recorded by the software PSV, which was controlling LDV. The exported data holding file extension unv were stored in Universal File Format (UFF) [79], which contained the time traces and FFT data of the measurements. A python program “unv_extractor.py” converted the unv file into binary and ASCII file for subsequent cleaning processes.

2.4.1 Drift correction

Since the measurements took a long period of time, the recorded time trace was slightly drifted. The following approaches were applied to correct the drifts:

For fluctuation and linear response measurements the low frequency baseline drifts were corrected. The complete time trace was Fourier transformed, low frequencies were removed from the frequency domain. After the inverse Fourier transform, the baseline was corrected.

Pre-processing of experimental data

For force steps the drift correction was achieved by fitting the baseline before the stimulus and after the stimulus linearly and the subsequent subtraction of the fit equation.

2.4.2 Outlier detection

Disturbances in the experimental data, for example the data out of the laser beam focus or sudden motion of the fly, were detected using outlier detection and excluded from the analysis. The python program “cutoffdetection_qt.py” and several more programs carry out the outlier detection based on the Grubb’s test [80].

To carry out the outlier detection for triggered data i.e. the step measurements, time traces of each of the 28 step stimuli were extracted, the mean values and standard deviations for each stimulus were computed. For continuous data i.e. the fluctuation and linear response function, each complete second was swept and its mean value and standard deviation were calculated.

Two z-scores [80] were defined:

For the mean value,

$$Z_{mean} = \frac{|X_i - \bar{X}|}{s},$$

with X_i being the tested value for measurement i , and \bar{X} the mean of complete trigger or sweep time unit and s the standard deviation.

For the maximal distance to mean value,

$$Z_{max} = \frac{Q_i - \bar{X}}{s},$$

with $Q_i = |\max (X_i - \bar{X})|$.

When

$$z > \frac{N - 1}{\sqrt{N}} \sqrt{\frac{t_{\alpha/(2N), N-2}^2}{N - 2 + t_{\alpha/(2N), N-2}^2}},$$

the hypothesis of no outliers is rejected at significance level of $\alpha/(2N)$ (in our case $\alpha = 0.5$), where $t_{\alpha/(2N), N-2}^2$ denotes the upper critical value of the t-distribution with N-2 degrees of freedom (in our case the number of measured points).

Data fragments which couldn't pass any of the both tests were excluded from further analysis.

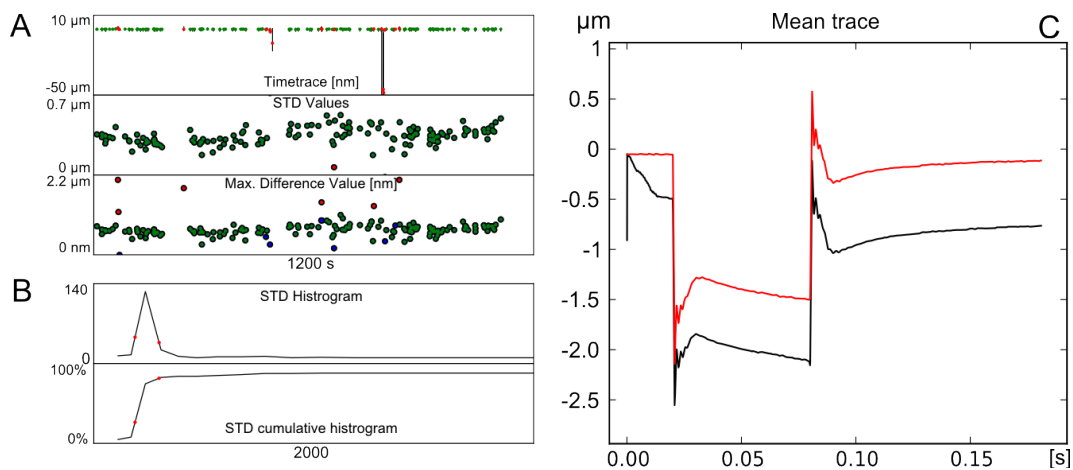


Figure 14 Data cleaning

The displacement response as a time trace is plotted (A. upper plot). On the time trace each of the same step events (A. upper plot green dots) is depicted. The standard deviation (A. middle plot) and maximal difference to the mean value (A. lower plot) of each step displacement responses are calculated. The Grubb's test was carried out for both of the conditions. Events excluded from the test are colored red, excluded by the other test blue. The distribution of the standard deviations of the data is shown in B. The selection boundaries of the standard deviation test are marked as red points. The displacement mean value of this step stimulus was calculated before (C. black line) and after (C. red line) the cleaning for validation. Experimental data provided by Dr. Thomas Effertz

2.4.3 Averaging

The displacement and nerve response of each individual force step were extracted, sorted after the 28 stimuli. After the outliers were filtered away one average time trace was generated (Figure 15). Time traces for fluctuation and linear response function were split into fragments of 1 sec. An average time trace and the standard deviation and standard error for each measured data point were computed as well.

Pre-processing of experimental data

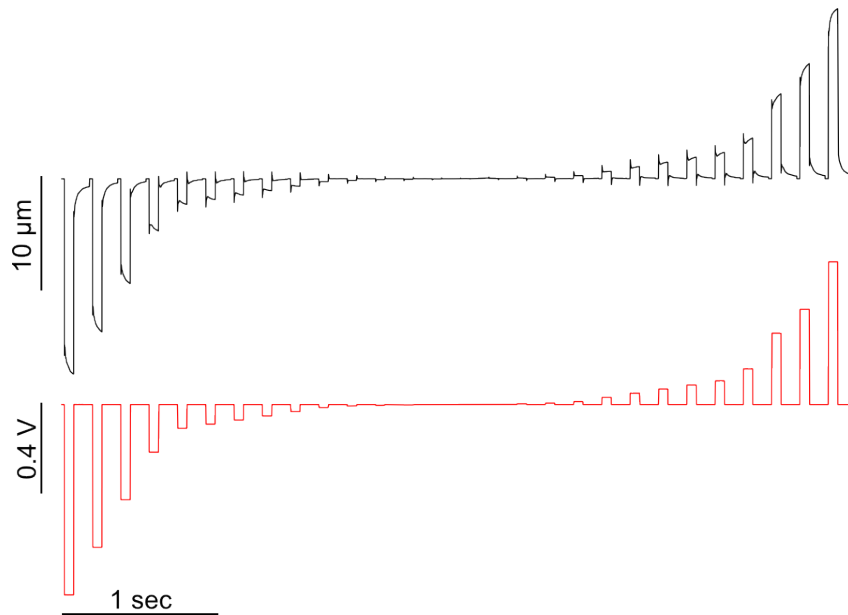


Figure 15 Averaged time trace

Demonstration of the averaged time trace for the displacement response (black) and the command voltages for the stimuli (red). Experimental data provided by Thomas Effertz

2.4.4 Data smoothing

To achieve the optimal data set for fit process the experimental data of fluctuation and linear response function after filtering of outliers and averaging should be smoothed. Smoothing algorithms range from the simple moving average to very sophisticated techniques involving Fourier transformation, frequency filtering, and Bach transformation. Depending on the quality two of the smoothing approaches could be optionally applied.

1. Smoothing based on the convolution of a scaled window function [81] with the signal itself. The moving average is the special case when the “flat window” is chosen. For more detail of the implementation please see the python function “`Lib.Smoothing.smooth(x, window_len, window)`”.

Savitzky-Golay (SG) smoothing: The Savitzky-Golay [82] removes high frequency noise from data. It has the advantage of preserving the original shape and features of the signal better than other types of filtering approaches, such as moving averages techniques. The SG is a type of low-pass filter, particularly suited for smoothing noisy data. The main idea behind this approach is to make

for each point a least-square fit with a polynomial of high order over an odd-sized window centered at the point.

2.5. Summary of experimental data

After the pre-processing we cleaned and averaged the experimental data. The following table summarizes all used experimental data.

Table 2 Summary of experimental data

Measurement	Function	Unit	Use of the data
Displacement response to electrostatic force step	$X(t)$	nm	Feed to the fit module of virtual ear
Nerve response to electrostatic force step	$N(t)$	mV	Analysis of Virtual Ear
Electrostatic stimulated Linear response function	$\tilde{\chi}(\nu)$	nm/pN	Feed to the fit module of virtual ear
PSD of free fluctuation of the arista	$\tilde{S}(\nu)$	nm ² /Hz	<ul style="list-style-type: none"> • Feed to the fit module of virtual ear • Analysis of energy flux
PSD of actuated anesthetized receiver	$\tilde{S}_s(\nu)$	nm ² /Hz	Analysis of energy flux

2.6. System requirement and integrated libraries for the programs

To carry out the pre-process and the fit of the experimental data and the subsequent analysis, a set of programs and scripts were involved. The “Virtual Fly Ear” and its peripheral scripts integrate a list of scientific and graphical libraries in multiple programming languages for the tasks like scientific computing, parallel computing, visualization, etc. These libraries, compilers and programs needed by the “Virtual Ear” and its peripheral scripts are listed in the following table.

System requirement and integrated libraries for the programs

Table 3 Libraries and description

Library	Description
Needed for C/C++	
GNU Scientific Library (GSL) [83]	GSL is a numerical library for C and C++ programmers under GNU General License, which provides a wide range of mathematical routines. The optimization calculation of “Virtual Fly Ear” is based the GSL function.
Qt4 [84]	Qt is a cross-platform UI framework. Programs in the “Virtual Fly Ear” with the graphical user interface are based on components of Qt.
SON Library	The library offers a set of functions to access the smr data files exported from the software Spike2. It is provided by the company CED upon request.
Qt widgets for technical applications (QWT) [85]	This library contains GUI components and utility classes which are primarily useful for programs with technical background. Some of the plotting tools of the “Virtual Fly Ear” are based on the QWT components.
Needed for Python	
Scipy [86]	The scientific computing tool for Python
PyQt [87]	PyQt is a set of platform independent Python bindings for Qt framework. It is used for the Python part of the programs
Numeric [88]	Numeric is a Python module for high-performance, numeric computing.
PyGSL [89]	This package provides a Python interface for the GSL.
ScientificPython [90]	A collection of Python modules those are useful for the scientific computing.
Matplotlib [91]	A Python plotting library
Python-sqlite [92]	A Python wrapper for the Sqlite library in C/C++ that empowers the Python to access Sqlite Databases.
Python-configobj [93]	A config-file reader and writer for Python.

Table 4 System requirements

System program	required	Linux/Unix	Windows
C/C++		Compiler g++	MinGW, MSYS
Python interpreter [78]		Python2.6 (version)	(tested Python(x,y) 2.6 (tested version)

System requirement and integrated libraries for the programs

3. Results

Modeling and simulation have provided detailed insights into the function of the *Drosophila* ear. However, running the models and simulations is time-consuming, preventing systematic analysis of auditory function in large number of flies. During my doctoral thesis I established a computational framework, the “Virtual Fly Ear”, which allows for high-throughput analysis of auditory function, providing the means to systematically compare this function between hearing-impaired mutants and respective controls. The Virtual Fly Ear integrates modules for the

1. pre-processing of experimental data,
2. modeling of this data and simulation that can be accessed via a graphical user interface.

The Virtual Fly Ear is described in the following sections (3.1-3.4) and was used to analyze auditory function in mutant flies (section 3.3). In addition, a novel method for analyzing auditory function is presented that allows quantifying power fluxes in the ear (section 3.4).

The virtual fly ear

3.1. The virtual fly ear

3.1.1 Structure and workflow of the programs

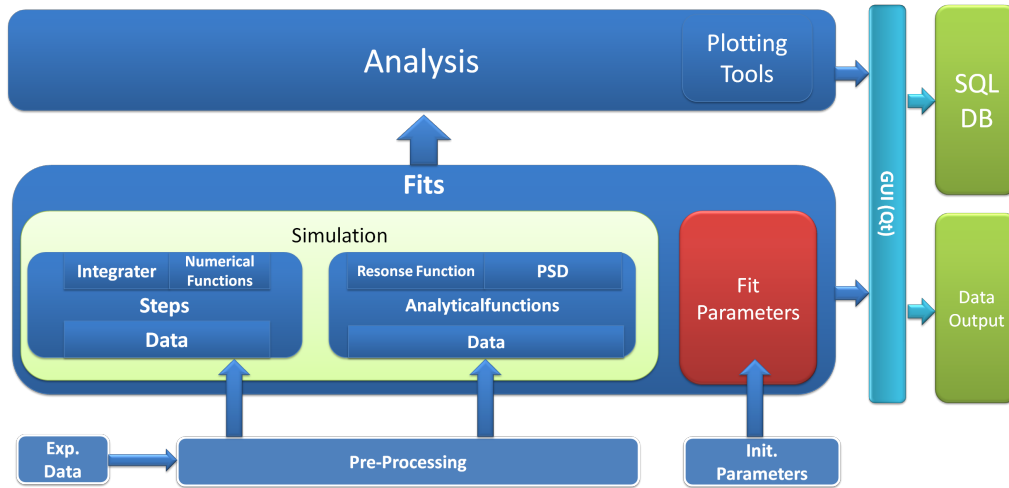


Figure 16: The workflow of the programs

The program framework “Virtual Fly Ear” consists of a set of modules covering numerical and analytical calculations, fitting, analysis and graphical user interfaces. The Figure 16 illustrates the program components and the arrangement.

The experimental data (see Table 2 in subsection 2.5) were processed via the pre-processing modules (for more details please see subsection 3.1.2) and then fed to the simulation modules where the mechanical response to step forces, the linear response function and the power spectral density (PSD) was simulated. For the fits, 64 or 128 sets of initial parameters were randomly generated. The respective fits, which run in parallel, were compared using the cost-function.

The mechanical response to step forces, the linear response function and the PSD were fed to the analysis modules to deduce gating compliance, parallel stiffness and the active work due to neurons exertion of the sound receiver. The results were plotted and data files in plain text format were produced.

To facilitate the usage and coordinate these programs, a GUI was programmed on the base of the Qt4 framework (see Table 3). Several windows were designed to guide the performance. For the parallel fit, which cannot be carried out via the GUI, a CLI command was generated.

The resulting parameter sets and the respective experimental data were stored in a database based on SQLite (see Table 3).

3.1.2 Post-processing of the experimental data

Experimental data of electrostatic experiment includes the time traces of mechanical and the electrical responses to force steps with 28 different forcing amplitudes in randomized order. After cleaning of the data, it was fed into the post-processing module. This post-processing included the averaging of the respective time traces, the sorting of force steps (and respective responses) with respect to forcing amplitude, the rearrangement of the time traces with rank numbers, which were assigned to steps of different amplitudes (with No. 1 being the largest negative amplitude and No. 28 being the largest positive amplitude; Force with direction away from the fly's body was defined positive and, respectively, force with direction towards the fly's body was defined negative.), detection of the forcing onsets and stationary states and the baseline correction. And at the end the time traces of each force step were truncated to a proper size for the fit procedure.

Furthermore the post-processing modules calculate the PSDs from fluctuation measurements and the linear response functions from the displacement responses to multi-sinusoidal stimuli.

The programs of the pre-processing packages were partially contributed by Dr. Björn Nadrowski (step recognition, step onset detection and acceleration determination).

3.1.2.1 Step recognition with edge detection

Step stimuli display edges. This property is used for automatically detection of the steps. The steps were recognized by applying the Discrete Wavelet Transform (DWT) according to the references [94] and [95]. A Python implementation was encoded in the package "edge_detection.py". The result of such edge detection is shown in Figure 17 illustrating this procedure highlighting the stimulus on- and offsets (data was measured with a wild type *Drosophila*, CS, with 28 force steps).

The virtual fly ear

The DWT edge-detection provided a significant range for the step candidates. With the given range, a local sigmoidal fit to the equation

$$V(t) = A_1 + \frac{A_2 - A_1}{1 + e^{\frac{t_0 - t}{\delta}}} \quad (16)$$

was performed. Here, $V(t)$ denotes the voltage used to provide the electrostatic force as a function of time. Five free parameters were fitted, A_1 corresponds to the left asymptote, A_2 to the right asymptote, t_0 to the time offset defining the voltage value at the halfway between A_1 and A_2 and δ to the steepness of the sigmoid curve

A significance coefficient, defined as

$$\frac{|amplitude\ of\ plateau - amplitude\ of\ baseline|}{\max(STD\ of\ baseline, STD\ of\ plateau)}$$

was calculated (STD stands for standard deviation). A cutoff value for the significance coefficient was defined. After dropping step candidates with a significance coefficient smaller than 5, true step stimuli were robustly recognized (Figure 17 lower panel).

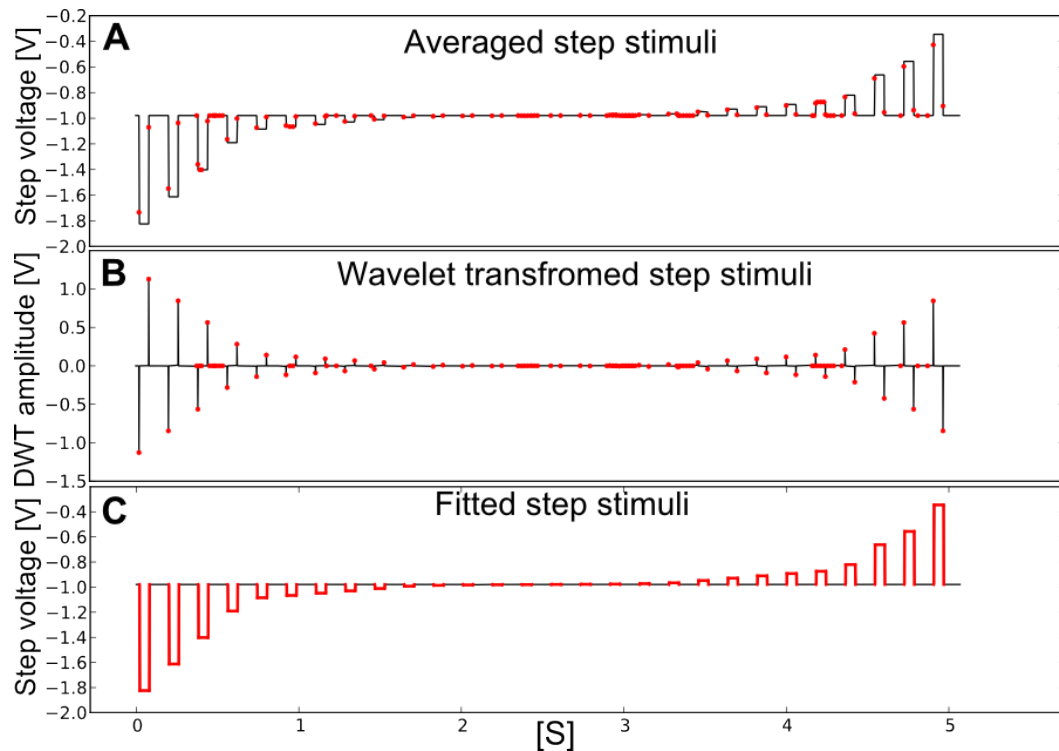


Figure 17: Applying DWT edge detection on step stimuli

The DWT of the averaged step stimuli (A) was calculated (B). The local extrema of the DWT were localized on the time trace and marked (red dots in A and B) both for the original and the transformed time traces. A subsequent sigmoidal fit was performed in the regions estimated via DWT. Step candidates that passed the cutoff condition, significance coefficient > 5 , are shown in C (red lines). Experimental data provided by Dr. Thomas Effertz

3.1.2.2 Determination of the onset of the steps

The onset of each step was determined by using the parameters of the sigmoidal fit (equation 16). A tangent of the sigmoid function at time point t_0 has an intercept with the lower asymptote. The point measured right before this intercept (marked with a star in Figure 18) was defined as the onset of the step.

According to the fit equation 16, the tangent (Figure 18, blue dashed line) at $t = t_0$ has the slope of $1/(4 \cdot \delta)$ and passes the point $(t_0, (A_2 - 2A_1)/2)$. Therefore, we can calculate the intercept with the asymptote $f(t) = A_1$, when $t = 2\delta(2A_1 - A_2) + t_0$. This is illustrated in Figure 18 using experimental data from a canton-S wild type fly. For the 20th force step, parameters were obtained:

The virtual fly ear

$A_1 = -0.979152$ V, $A_2 = -0.947501$ V, $t_0 = 3.45958$ s and $\delta = 3.5 \times 10^{-6}$ V. The slope of the tangent was 1.4×10^{-5} V/s and the step began at 3.459572 s, because the sampling frequency was 13.1 kHz.

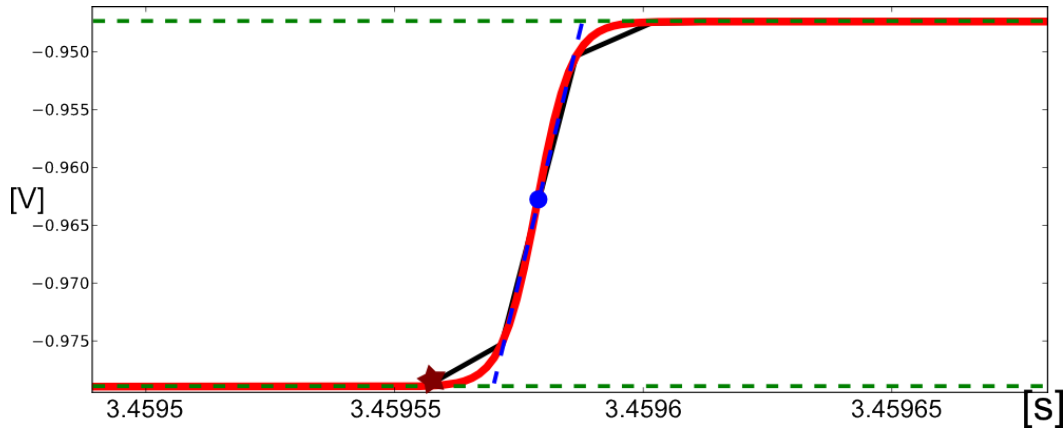


Figure 18: Fitting the step onset with sigmoidal function

The step stimulus (black line) was fitted to the sigmoid function (fit curve shown as red line). The tangent at $t = t_0$ (marked as blue dot) was calculated (blue dashed line). The asymptotes of the sigmoid function are shown as green dashed line. The last measured data point (marked as star) before the intercept of the lower asymptote and the tangent was defined as the step onset. Experimental Data provided by Dr. Thomas Effertz.

3.1.2.3 Determination of the onset acceleration and the stationary state of the response

Because the mass of the sound receiver can be assumed to be constant and was unknown before the fit, the onset accelerations of its response to force steps were calculated and used to estimate the electrostatic force. The onset accelerations were evaluated by a post-processing module (Python package “ResponseStepDetector.py”).

Using this package, the acceleration of the antennal displacement around the onset of the step stimuli was fitted with the equation

$$X(t) = X_B + X_0[1 - e^{-\lambda(t-t_0)} \cos(\omega(t-t_0))]. \quad (17)$$

Here, $X(t)$ corresponds to the displacement response to the step at time t , X_B to the baseline amplitude, X_0 to the maximal amplitude, λ to the decay constant, ω to the natural angular frequency and t_0 to the time point where the stimulus event occurs. The five free parameters, $X_B, X_0, \lambda, \omega$, and t_0 , were fitted with the Orthogonal Distance Regression Algorithm. The onset acceleration was estimated as

$$a(t_0) = \frac{d^2X}{dt^2}(t_0) = X_0(\omega^2 - \lambda^2).$$

To determine the response displacement at stationary state, additionally, the measurement points around the offset of the step response were fit with the exponential equation

$$X(t) = Ae^{-t/B} + C, \quad (18)$$

in which A, B and C are free parameters. The asymptote, $X(t_s)=C$, was defined as the stationary displacement of the receiver's response. Also here, the Distance Regression Algorithm was used for the fit.

3.1.2.4 *Baseline correction and truncation of the time trace*

At the end of the post-processing of the data, the baselines of step responses were corrected to 0 nm. Stimuli and responses were isolated (Figure 19).

The virtual fly ear

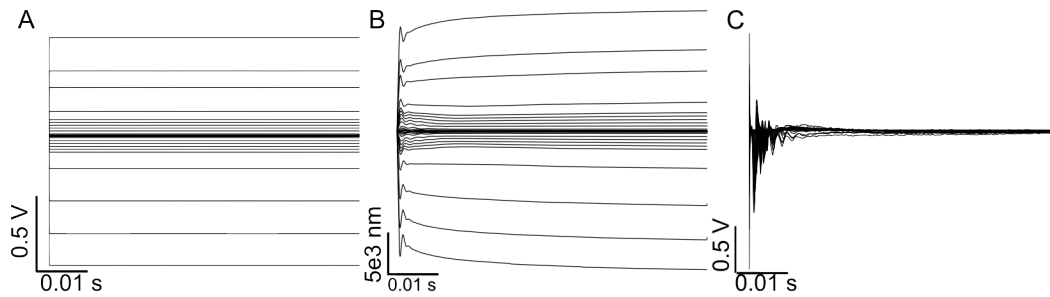


Figure 19: Separated step stimuli and responses

The step stimuli (A) and responses (B for displacement response; C for CAP responses) were truncated according to the onset/offset time points. The base lines before stimulus onsets and onset time points were zeroed. For details of the data behind these figures please see Table 5. Experimental data provided by Dr. Thomas Effertz.

Once finished, a text file containing the result of the post-processed steps measurements is automatically produced. For instance, the information about the stimuli and responses of a measured wild type fly (CS) is overviewed in the following table:

Table 5: Result file produced by the post-processing modules

Step- No.	Time of Step Onset	Time of Step Offset	Stimulus Amplitudes	Onset Accelerations	Peak Displacements	Stationary Displacements	Onset CAP Amplitudes	CAP Peak Amplitudes	...
	[s]	[s]	[V]	[m/s**2]	[nm]	[nm]	[mV]	[mV]	
1	0.02	0.08	5.43E-04	-232.59	-15538.56	-17230.62	0.28	-0.83	
2	0.20	0.26	4.31E-04	-173.34	-11979.40	-13567.36	0.36	-0.79	
3	0.38	0.44	2.76E-04	-114.69	-8403.68	-9330.44	0.41	-0.78	
4	0.56	0.62	1.51E-04	-56.69	-4827.47	-4704.90	0.38	-0.74	
5	0.74	0.80	7.05E-05	-27.89	-2873.49	-2328.96	0.38	-0.68	
6	0.93	0.99	6.07E-05	-23.08	-2478.38	-1884.18	0.42	-0.69	
7	1.11	1.17	5.36E-05	-18.26	-2093.97	-1512.61	0.42	-0.66	
8	1.29	1.35	4.01E-05	-13.14	-1662.31	-1079.09	0.39	-0.63	
9	1.47	1.53	2.96E-05	-8.31	-1196.68	-685.09	0.41	-0.58	
10	1.65	1.71	2.41E-05	-3.51	-641.10	-266.04	0.39	-0.47	
11	1.83	1.89	2.13E-05	-1.73	-414.63	-139.13	0.38	-0.33	
12	2.01	2.07	2.10E-05	-0.78	-269.22	-77.62	0.41	-0.16	
13	2.19	2.25	1.89E-05	-0.54	-186.19	-50.21	0.42	-0.06	
14	2.37	2.43	1.36E-05	-0.28	-97.07	-22.95	0.45	-0.02	
15	2.55	2.61	1.71E-05	0.15	49.59	12.36	0.41	0.00	
16	2.74	2.80	1.42E-05	0.35	136.30	38.52	0.39	-0.03	
17	2.92	2.98	1.56E-05	0.70	236.85	63.83	0.42	-0.11	
18	3.10	3.16	2.29E-05	1.52	393.18	130.90	0.40	-0.29	
19	3.28	3.34	2.51E-05	3.28	630.72	278.20	0.37	-0.45	
20	3.46	3.52	3.20E-05	8.29	1186.09	678.05	0.42	-0.54	
21	3.64	3.70	3.68E-05	12.86	1665.25	1155.63	0.41	-0.59	
22	3.82	3.88	5.25E-05	18.01	2107.64	1514.70	0.43	-0.63	
23	4.00	4.06	6.50E-05	22.48	2519.85	1976.31	0.40	-0.67	
24	4.18	4.24	6.87E-05	27.49	2900.68	2394.87	0.38	-0.67	
25	4.36	4.42	1.08E-04	41.61	3972.58	3773.29	0.38	-0.71	
25	4.55	4.61	1.75E-04	84.09	6936.90	7767.27	0.40	-0.79	
27	4.73	4.79	2.50E-04	112.95	8894.17	10321.61	0.44	-0.83	
28	4.91	4.97	4.91E-04	171.40	12926.28	14999.64	0.42	-0.88	

For reasons of clarity, only some of the parameters are shown.

3.1.2.5 Power spectral density and linear response function

Apart from the response to step stimuli, also the receiver's fluctuation and the responses to multi-sine-stimulation are post-processed. Frequencies that will be

The virtual fly ear

used for fitting are selected and outliers in the experimental data can be removed (e.g. 50 Hz and its multiples).

The results are output to plain text files, which will be registered in a database and used for fits.

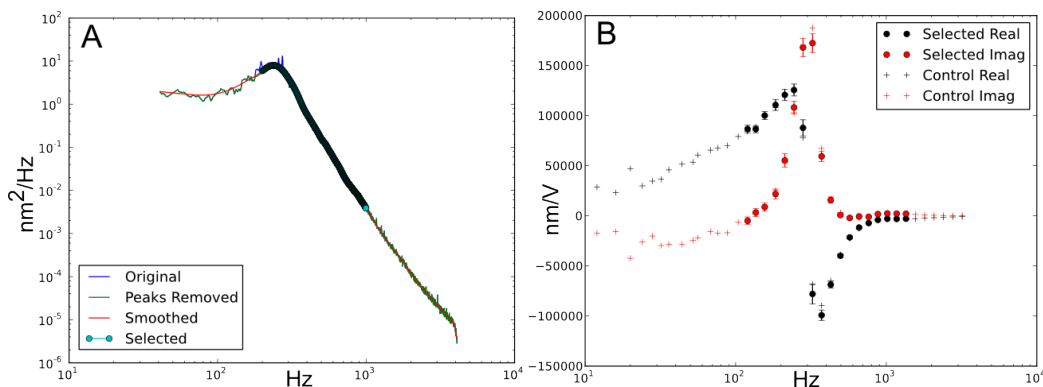


Figure 20: The pre-processing of the PSD and the linear response function

A. the PSD from the original recording was calculated (blue line), the outlying points were removed, the missing data points after deletion were linearly interpolated (green lines) the result data were then smoothed (red line) and selected (turquoise dots and line).

B. linear response function at selected frequency is calculated based on the cleaned time trace (black dots marked the real part of the function and red dots the imaginary part). The result was compared with the calculation of Polytec software (+ marked points).

Experimental data provided by Dr. Thomas Effertz.

3.1.3 Data storage (database structure)

To organize experimental data and result files, a relational database was established that is based on SQLite (Table 3), which is adequate for the portability as well.

This database consists of two data tables and three reference tables. Information about the experiment animals is stored in the data table “Fly”. Each data record in the table “Fly” can be linked to multiple fit and analysis results that are stored in

the data table, “Parameters”, which is linked to the table “Fly” via the indexing field “Fly.id“(see Figure 21). Additional information about the animals (e.g. synonyms of genotype names) is provided by reference tables, which are again linked to data tables via the indexing fields.

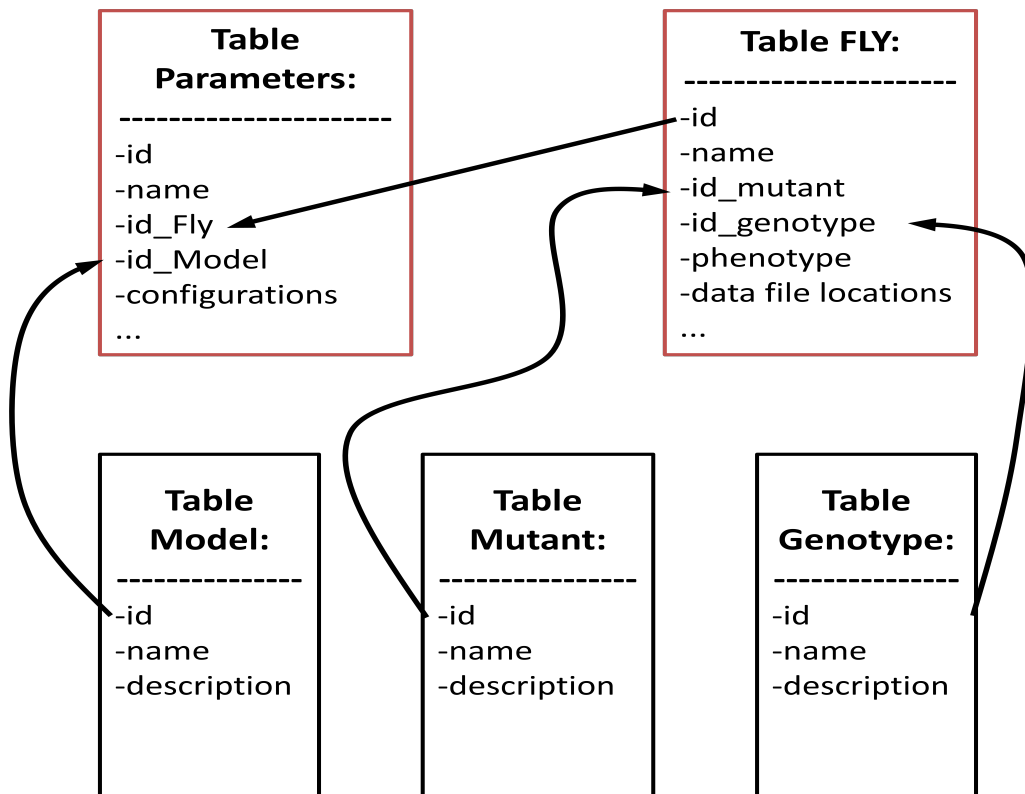


Figure 21 database structure

The database consists of 5 tables: two data tables (red boxes) and three reference tables (black boxes). The tables are connected together with their key indices. Arrows show the joining directions of the connection constraints of the SQL-Statement.

The virtual fly ear

3.1.4 Graphical user interfaces

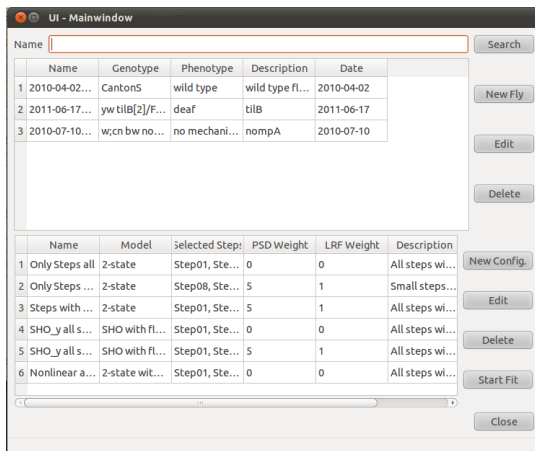


Figure 22 GUI: Main window

The GUI window overviews of the database table “Fly” and the daughter table “Parameters”, which can be modified by the buttons.

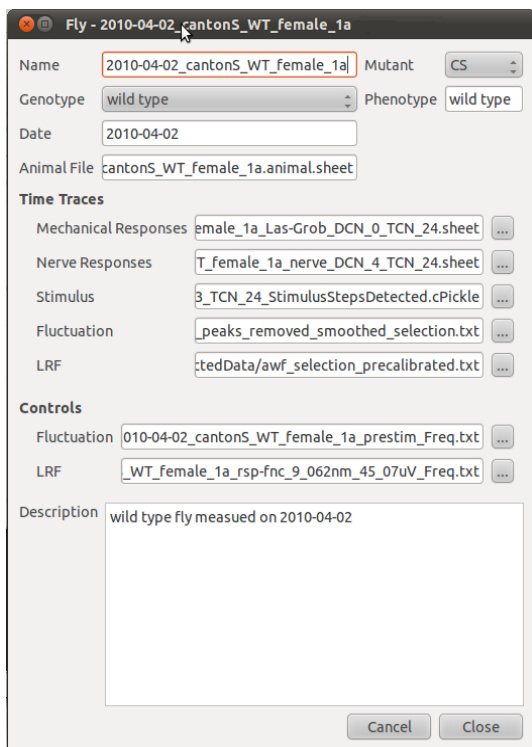


Figure 23 GUI: Flies Management

The content of table “Fly” can be administrated by using this window

In the framework of the “Virtual Fly Ear” each *Drosophila* ear is represented by its fit parameters. After post-processing Experimental data is fitted. The fit parameters are then stored in a database for further analysis. To simplify fitting and storing, graphical interfaces are designed and implemented in Python and Qt (Python package PyQt [87]) and C++. In this subsection, the work flow of data fitting and storing with the help of graphical user interfaces (GUI) is illustrated by screenshots.

Figure 22 is a screenshot taken from the main window of the “Virtual Fly Ear”. The upper table is an overview of the records in the database table “Fly” providing information about different animals. For instance, information of the genotype and location of associated data is registered in this table. Each of the records can maintain more than one parameter sets according to the configuration of the fit. The respective fit parameters and configuration are stored in the table “Parameters”, which is shown in the lower table of this window. Records can be added,

edited, or deleted by clicking the buttons (right). Picking a fit configuration from the table and clicking the button “Start Fit” carries out the fit with the chosen model.

The records in table “Fly” are managed with the help of the window shown in Figure 23. There, all the information about the fly and the links to associated data that are registered in the data base can be accessed.

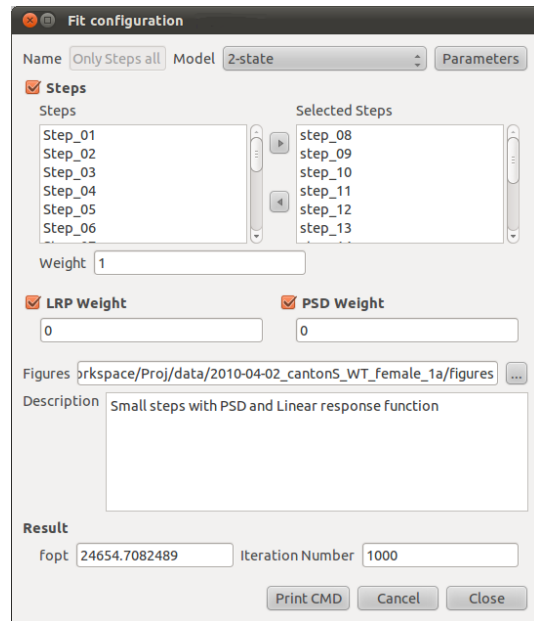


Figure 24 GUI: Fit configuration

Fit configurations (shown in the lower table on the main window,

Individual fit configurations are set.

Figure 22) are set by means of the window “Fit configuration”, shown in Figure 24. One can choose: the fit model from a dropdown list; the desired force step stimuli from a list of available steps; whether the fit to PSD and LRF should be included, and at which location output figures and parameter settings are stored

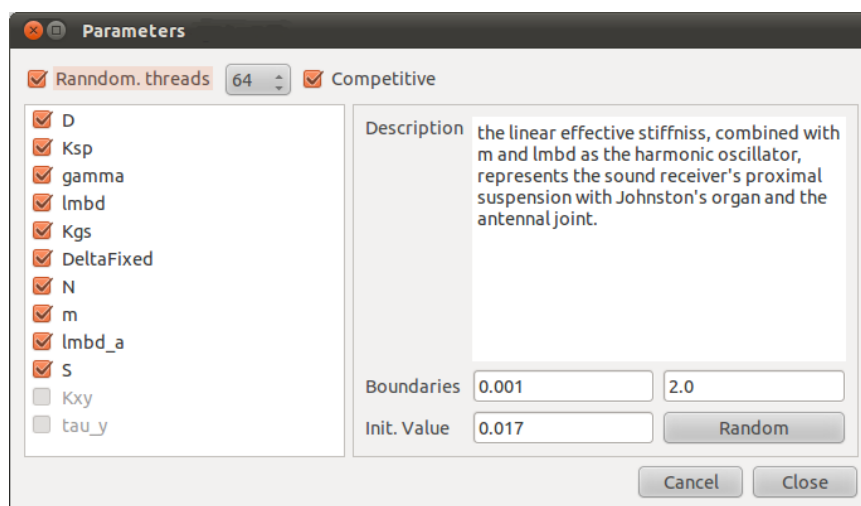


Figure 25 GUI: Parameters

Free parameters are selected and their initial parameters can be estimated randomly. The number of fit threads and competition mode are set.

The virtual fly ear

(Figure 25). If one chooses to carry out the fit process by clicking the button “Start Fit” on the main window, the fit program only runs with one CPU-thread (without parallel algorithms) due to the restriction of the Qt library. An alternative way to run the fit using the parallel algorithms would be via the command line interface: by clicking the button “Print CMD” on the window for fit configuration, a command line is returned, which can be copied to the command line interface and run directly. Depending on the CPU architecture, using the parallel algorithms can reduce the run-time of the fit program by multiple times.

Clicking the button “Parameters” on the window “Fit configuration” opens the window for parameter settings (Figure 25). To obtain a good estimation of the initial parameters for the Downhill-Simplex-Algorithms [77], 2^n (n for 0, 1, 2 ...) initial simplexes (parameter sets) can be randomly generated inside reasonable boundaries. Depending on the configuration, each of these initial simplexes runs in his own thread until the end (the stop condition) or until a certain station is reached. The number of these initial simplexes is set in the window “Parameters” (Figure 25) via a dropdown input box, provided the check box “Random. threads” (upper left corner) is checked. One can choose the “Competitive” mode by ticking the check box right behind the dropdown list. When the “Competitive” mode is chosen, the optimization threads started with the randomized initial simplexes will make a stop at a certain point, which is predefined as 100 iterations performed by the Downhill-Simplex-Algorithm. At this point, the threads are sorted according to the values of cost-function, which is described in section 3.1.5.8. Based on these values, half of the threads with high cost are discarded. The surviving threads are allowed to further compete until only 4 threads are left. These four threads are run till the end. The result parameter set of the thread with the best cost-function value will be stored in the database; information about other threads can be found in a log-file. All available parameters for the fit are listed in a list box where unsuitable parameters combinations are grayed out. The checked parameters will vary in the fit; others will be fixed to their initial values. When the check box “Random. Threads” is unchecked, the specified initial values in the input box “Init. Value” will be used. By clicking on the button “Random”, a random value is suggested with respect to the boundaries, which follows:

$$\text{Parameter Value} = e^{\ln B_l + (\ln B_u - \ln B_l)r},$$

where B_l corresponds to the lower boundary, B_u to the upper boundary, and r to a uniformly distributed random number.

Reference tables are managed via the window “Preferences” (Figure 26). A dropdown list helps to choose the desired reference table. By clicking the button “New”, a distinct key for the new record is generated. It can then be edited or deleted. These reference tables prevent multiple entries due to different synonyms of mutants, genotypes, etc.

When the fit process is finished, the result parameters are stored in the database table “Parameters” with the corresponding fit configuration. Experimental data and the simulations are plotted (Figure 27). The figures are saved at a specified storage location (Figure 24).

In order to gain a more intuitive understanding of the dynamics of the model, a visualization tool based on the two-state general model (see section 3.1.5.1) was implemented (Figure 28). Model components like the antennal joint, the parallel spring, the gating-spring modules with transduction channel and the gating spring are scaled, symbolized and visualized with a

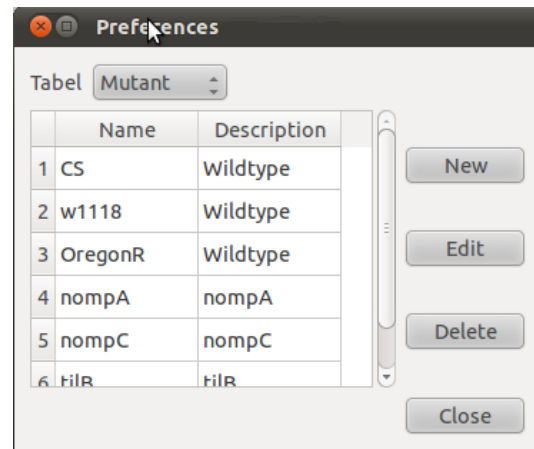


Figure 26 GUI: Reference tables

The reference tables are administrated.

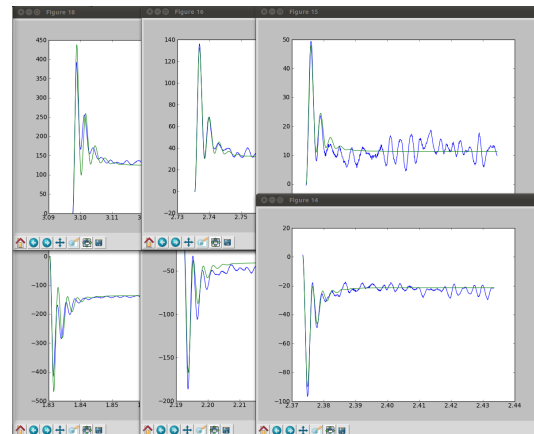


Figure 27 GUI: Plots of the fit result

After the fit processing is finished, the experimental data and simulation data resulting from the best fit parameters are plotted and saved. Experimental data provided by Dr. Thomas Effertz

The virtual fly ear

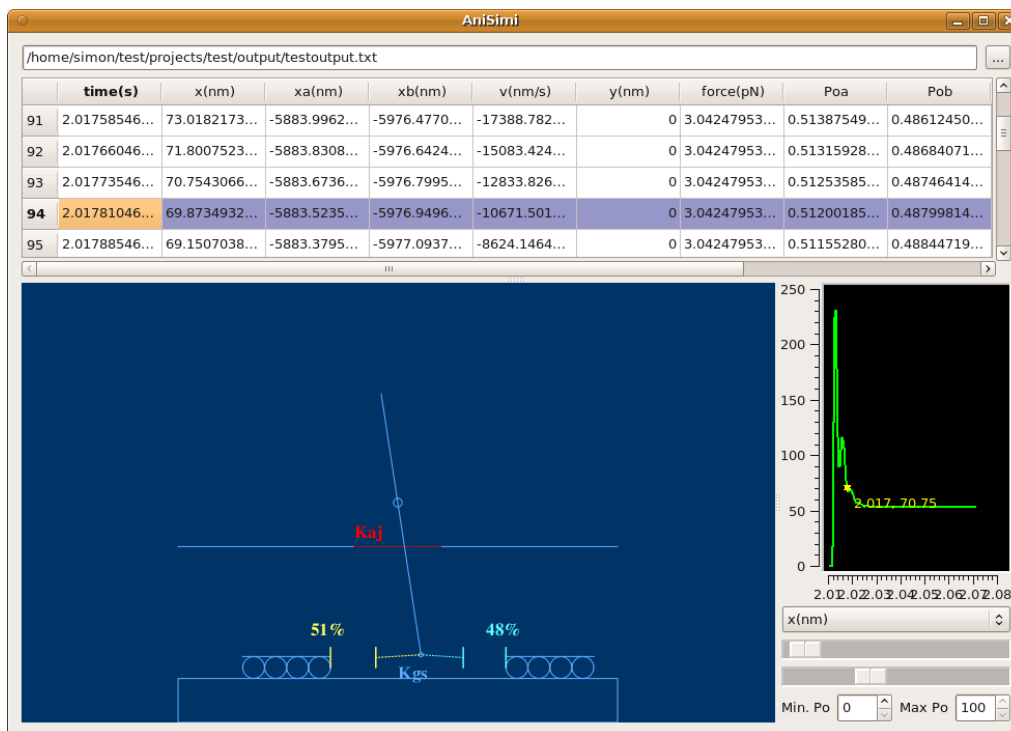


Figure 28 GUI: Visualization tool for the simulations

Demonstration of a simulation: based on the simulation data (upper table) an animation with symbolized model components was dynamically generated. Time traces of chosen variables of the model differential equations were monitored in the lower right corner.

dynamically generated animation. The time signals can be followed visually while the program scrolls through the data.

3.1.5 The models

The GUI described in the last subsection interfaces between user, database, and the mathematical core of the “Virtual Fly Ear” (see also Figure 16). Programs and scripts defining the GUI and the mathematical core are kept separately, so that they also can be used alone either through the command line interface or a recombined script.

In the mathematical core, the revised and modified gating spring model [69-71, 74] for the fly’s ear [44] (section 1.7.2) and four extended models were implemented. The biophysical models are mathematically described by a set of coupled differential equations that are encoded in the Python package “ode_funcs”. The routines for integrating the functions are encoded in the Python

package “integrator”. Depending on the selected model, the fourth-order Runge-Kutta method [96] or the Euler method are used for evaluating the solutions of the ordinary differential equations.

3.1.5.1 The two-state model

This model is described by Nadrowski et al. 2008 ([44]). A schematic illustration including 2 states of the channel is shown in Figure 29.

In this model, only one type of transducer channel is involved (Figure 29, green markers). Each channel can assume 2 states: open or closed. Two identical populations of the transducer modules, which is composed of one gating spring, one transduction channel and adaptation motors, are symmetrically coupled with a simple harmonic oscillator that represents the fly’s antennal receiver [44] (Figure 29).

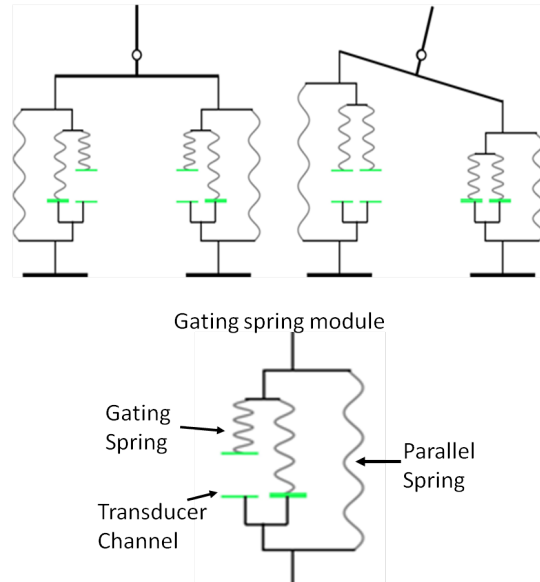


Figure 29: The cartoon of two-state model for *Drosophila* hearing organ

Opposing gating spring modules are arranged symmetrically and are attached to the a2/a3 joint (black circle). Each module contains one transduction channel (marked green). The channel can assume 2 states: open or closed. At the resting position, the open probability is c.a. 0.5 (upper left panel). Lower panel: sketch of a single transducer module. Adaptation motors are not shown.

The dynamics of the model are described by four coupled first-order differential equations:

$$\begin{aligned} \dot{X} &= V \\ \lambda_a \dot{X}_a &= K_{GS}(X - X_a - DP_o(X - X_a)) + F_{max}(SP_o(X - X_a) - 1) \\ \lambda_a \dot{X}_p &= K_{GS}(-X - X_p - DP_o(X - X_p)) + F_{max}(SP_o(-X - X_p) - 1) \end{aligned}$$

The virtual fly ear

$$m\dot{V} = -K_{GS}(X - X_a - DP_o(X - X_a)) + K_{GS}(-X - X_p - DP_o(X - X_a)) - \lambda V - K_{AJ}X + F_{ext}$$

The first equation couples the velocity and the displacement of the arista tip.

The dynamics of the anterior and posterior transducer modules are described by the 2nd and the 3rd equations, where K_{GS} denotes the combined gating spring stiffness, X_a and X_p the projected position of anterior and posterior adaptation motor onto the tip of arista, D the projected gating swing, $P_o(X - X_a)$ and $P_o(-X - X_p)$ the open probabilities of anterior and posterior channel population, respectively. The adaptation motors display a linear force-velocity relation, which is characterized by the projected slope λ_a . The maximal force that the adaptation can generate is denoted by F_{max} .

The harmonic oscillator and the symmetrically coupled transducer modules are described by the 4th equation, where X denotes the arista position, m the effective mass of the sound receiver, V the velocity of the arista, λ the friction constant of the antennal joint, K_{AJ} the stiffness of antennal joint, and F_{ext} the external force experienced by the arista tip.

In these differential equations the open probability P_o is defined as [69, 74]:

$$P_o(Y) = \frac{1}{1 + Ae^{-\frac{Y}{\delta}}} \quad (19)$$

with

$$\delta = \frac{Nk_B T}{K_{GS}D}, \quad (20)$$

where δ is the typical distance the receiver has to move in order to change the state of the channels, N is the number of transducer modules in one corresponding transducer population and A is a factor that accounts for the intrinsic energy difference between the channel states:

$$A = e^{\frac{\Delta G + K_{GS}D^2/(2N)}{k_B T}}, \quad (21)$$

Here, ΔG denotes the intrinsic energy difference and k_B and T are the Boltzmann constant and the ambient temperature, respectively.

To describe stimulus-evoked electrical response of the fly's ear, open probabilities that exceed the resting P_o are summed up for both transducer populations, and are defined as: $P_e = \max(P_{o,a} - P_{o,s}, 0) + \max(P_{o,p} - P_{o,s}, 0)$, where $P_{o,a}, P_{o,p}$ denote the open probabilities of the anterior and posterior channel populations, respectively. The stationary open probability at rest is denoted as $P_{o,s}$.

To fit the experimental data that is used for testing mechanical correlates of transducer gating and adaptation (the experiment is described in section 2.3.5), $P_{o,s}, S, K_{AJ}, \delta, \lambda, K_{GS}, \lambda_a, m$, and N are free fit parameters, D and F_{max} were calculated using equation 19 and equation 24 in section 3.1.5.6.

Mechanical measurements revealed that the displacement response of the sound receiver to the step force display a characteristic pattern [23]. The time trace of the displacement response shows an initial overshoot in the forcing direction that is followed by a rebound and a damped oscillation. After certain time, a constant steady-state position is reached (Figure 30 A). The height of the initial displacement peak at stimulus onset is nonlinearly related to the stimulus force (Figure 30 B and C, blue curve for simulated and dots for experimental data): the corresponding dynamic stiffness of the antennal receiver decreases, when the external force declines (Figure 30 C). The displacement of steady-state scales linearly with the stimulus force (Figure 30 B and C, black curve for simulated and dots for experimental data). Within the limit of small stimulus forces ($F_{\text{external}} = 0$ to 10 pN), these force-displacement characteristics are accurately reproduced with the 2-state model.

The virtual fly ear

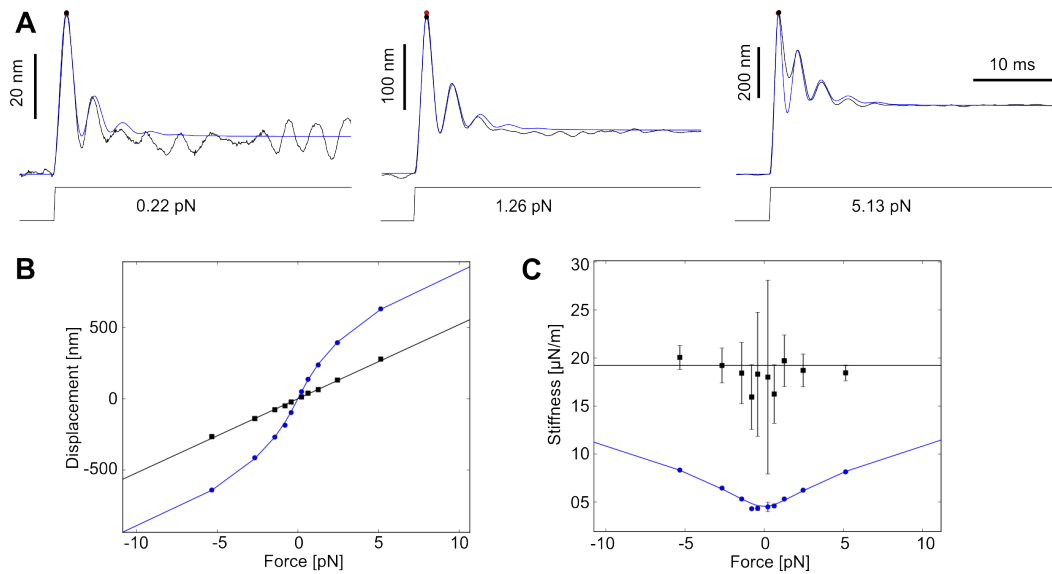


Figure 30: Mechanical responses of wild type fly fitted with 2-state model

(A) Time traces of receiver's displacement in response to force steps. Experimental data (black) and simulated data (blue) showed same characteristic pattern. The automatically detected onset peak displacements are marked as dots (black dots for experimental data and red dots for simulated trace)

(B) Displacements are plotted against external forces. Onset displacements (blue) displayed nonlinear relation with external forces. Displacement responses of steady-state (black) scaled linearly with external force. Measured data are marked by dots and simulations are shown as curve.

(C). Slope stiffness at initial displacement peak (blue) and at steady-state (black) are plotted against force. Measured data are marked by dots and simulations are shown as curve. The transient nonlinearity at initial displacement peaks is well fitted.

All measured data represent of 200-300 repetitions and error bars indicate standard deviation. Experimental data provided by Dr. Thomas Effertz.

By using the “Virtual Fly Ear”, motor movements and channel open probabilities can be predicted (Figure 31). For small force steps, the predicted excess open probability well describes the amplitude characteristics of the measured CAPs [44].

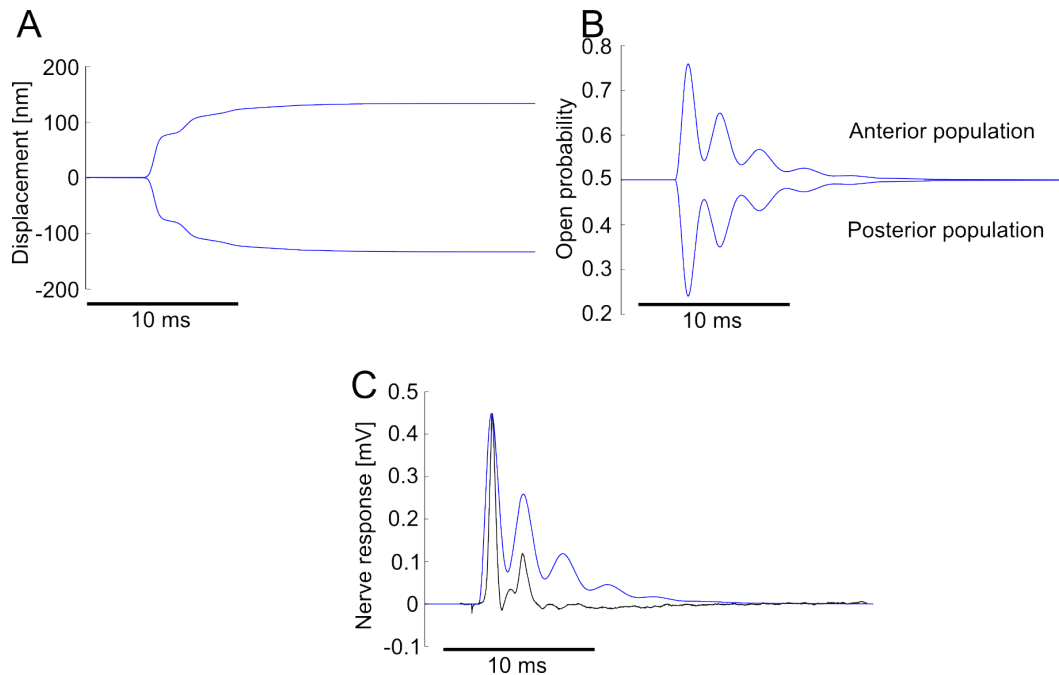


Figure 31: Deduced motor movement and channel open probabilities of wild type fly by 2-state model

Simulation with 2-state model and corresponding fit parameters predicts the motor movements (A) and channel open probabilities (B) of anterior and posterior transducer populations. Predicted excess open probability (C, blue) is compared with CAP (C, black). Experimental data provided by Dr. Thomas Effertz.

(a) Limitation of the 2-state model: large forcing amplitude

In wild-type flies, antennal displacements equal to or greater than ~ 50 nm are sufficient to elicit CAPs [62]. The maximum amplitudes of CAP increase monotonously for displacements between ~ 50 nm and ~ 60 nm [62], defining the dynamic range of the CAP response. The force-displacement characteristics in this range are accurately reproduced by the simulation with 2-state model (Figure 30). To test whether the two-state model can describe the force-displacement characteristics beyond this dynamic range, larger step forces (up to 400pN in both posterior and anterior directions) were applied. The results of a general fit (section 3.1.5.8) are shown in Figure 32.

Although the details of the time traces (Figure 32 A) were qualitatively reproduced, small quantitative deviations occurred (Figure 32 B and C). In the

The virtual fly ear

following subsections (3.1.5.2-3.1.5.5), the model is modified to also obtain a quantitative description of the measured data. To get a better idea about the system mechanics and how it can be modeled, I analyzed auditory mechanics in mutant flies.

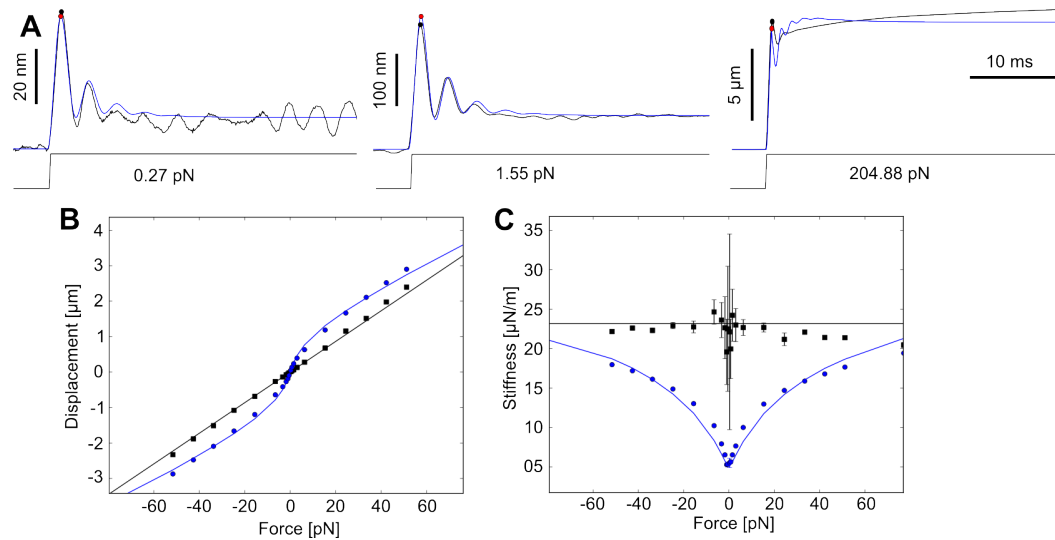


Figure 32: Force-displacement characteristics of wild-type fly (Canton-S) with large stimuli fitted by 2-state model

(A) Time traces of receiver's displacement in response to force steps. Experimental data are shown in black, simulated data in blue. (B) Initial peak displacements (blue dots) and steady-state displacements (black squares) are plotted against external forces. Experimental data are shown as discrete points, simulated data as curve. (C) Slope stiffness at initial displacement peak (blue dots) and at steady-state (black squares) are plotted against force. Discrete data points and curve as in (B). All measured data represent of 200-300 repetitions and error bars indicate standard deviation (partly not visible due to their small size). Experimental data provided by Dr. Thomas Effertz.

(b) Limitation of the 2-state model: creep in the receiver mechanics

Mutations in *tilB* and *nompA*, cause anatomical defects in Johnston's organ due to aberration of dendritic cilia of the mechanosensory neurons (*tilB* [47]) or due to disconnection between the mechanosensory neurons and the antennal receiver (*nompA* [46]). Because of the loss of the connection between the receiver and the neurons, the nonlinearity of initial overshoots breaks down (Figure 33). This nonlinearity is abolished in the simulations using the two-state model with corresponding fit parameters (Figure 33 C and F). Furthermore, receivers of *tilB* and *nompA* mutants slowly crept towards the displacement at steady-state. This

creep could not be reproduced with the 2-state model and simulations still displayed nonlinearity (Figure 33 A and D). Apparently, the 2-state model in its present form does not allow describing the receiver mechanics of *nompA* and *tilB* mutants. In section 3.1.5.2, I will show that good fits can be obtained when the model is supplemented with a floating joint.

The virtual fly ear

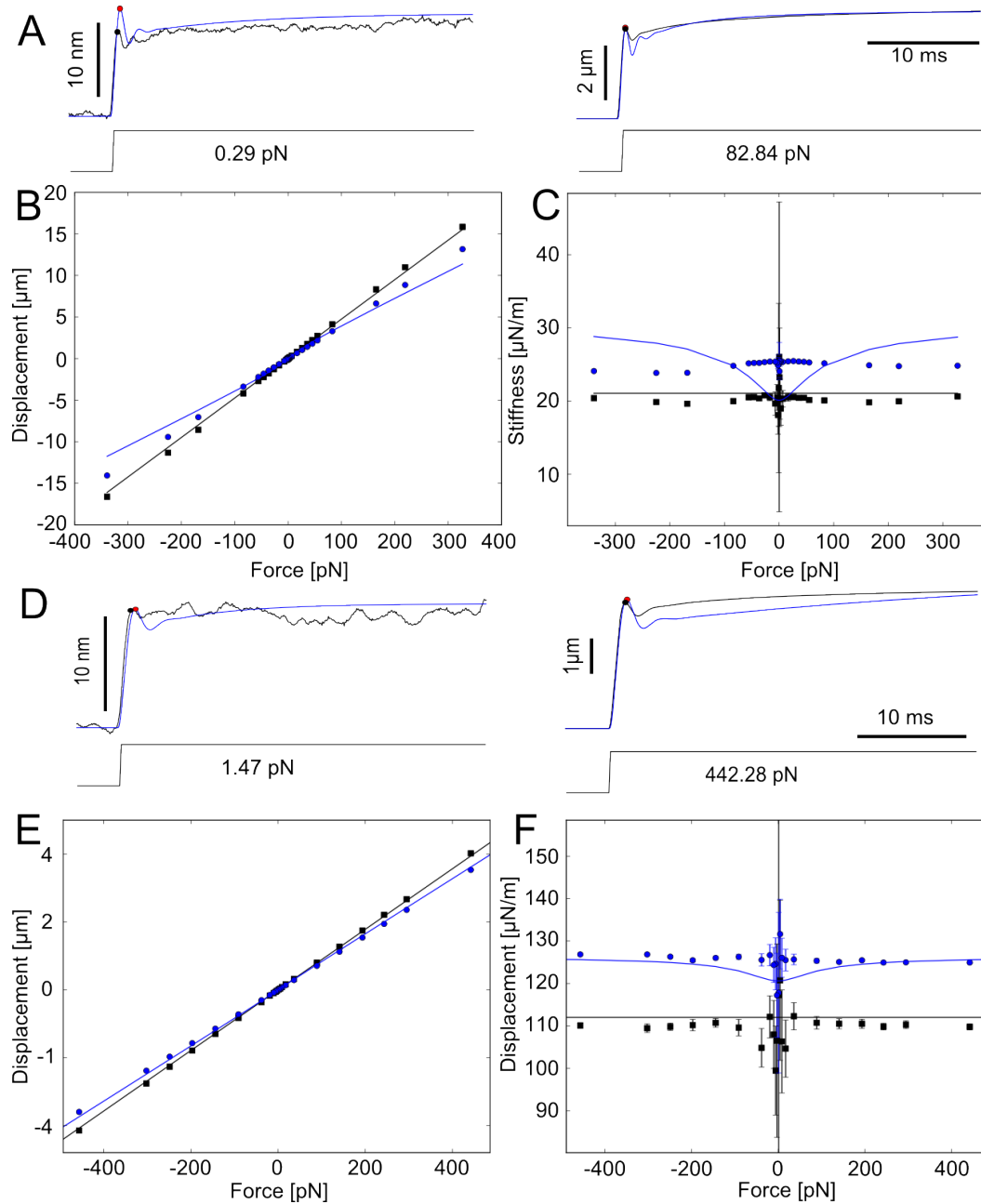


Figure 33: Fit results of *tilB* and *nompA* mutants with 2-state model

(A) and (D): Time traces of *tilB* mutant and *nompA* mutant, respectively. Experimental data are shown in black, and simulated data are shown in blue. Detected stimulus onset peak displacements are marked as dots, black for experimental and red for simulated data. (B) and (E): Displacement-force relation for mutant of *tilB* and *nompA*, respectively. Onset peak displacements (blue) and steady-state displacement (black) are plotted against the corresponding force stimuli. Experimental data are shown as discrete data points, and simulated data are shown as curve. (C) and (F): Plot of slope stiffness against the corresponding force stimuli for *tilB* mutant and *nompA* mutant, respectively. Experimental and simulated data are shown as in (B) and (E). All measured data represent of 200-300 repetitions and error bars indicate standard deviation. Experimental data provided by Dr. Thomas Effertz.

NompC is a candidate auditory transduction channel [51, 63-66]. Measurements of the auditory mechanics in *nompC³* nulls revealed that the initial overshoot in the receiver's response to force steps is absent and that the nonlinearity is reduced. This residual nonlinearity was not well described by the two-state model. Because only one half of the neurons of the fly's JO seem to require NompC function, a four-state model with two distinct NompC-dependent and -independent channels was developed, which yields fits to measurements obtained from wild-type flies with lower cost-function values (see section 3.1.5.5).

Simulations with the fit parameters could just reproduce the temporal evolution of the time traces for each step (Figure 34 A). Stiffness of the onset displacement peak and steady-state showed large deviations to the experimental data.

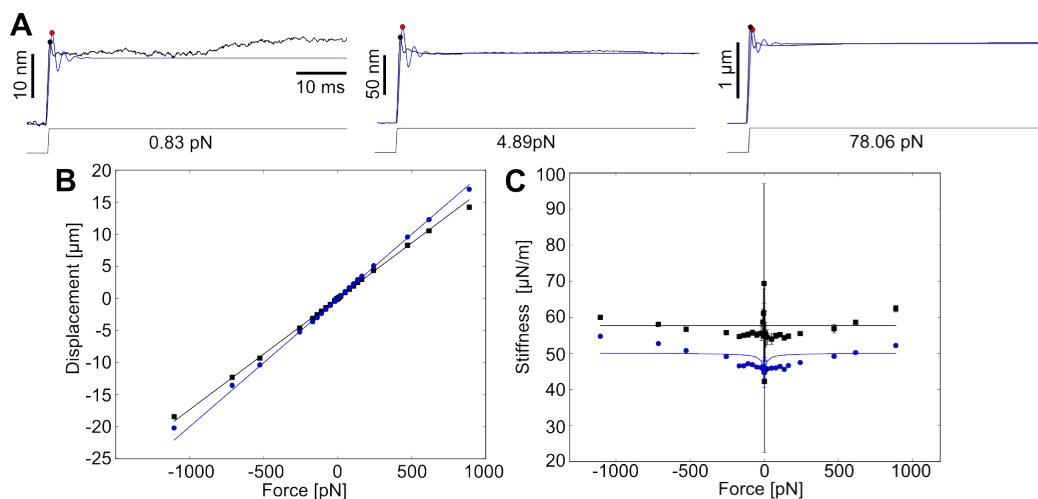


Figure 34: Fit results of *nompC* mutants with 2-state model

(A) Time traces of receiver's displacement in response to force steps. Experimental data are shown in black, simulated data in blue. (B) Initial peak displacements (blue dots) and steady-state displacements (black squares) are plotted against external forces. Experimental data are shown as discrete points, simulated data as curve. (C) Slope stiffness at initial displacement peak (blue dots) and at steady-state (black squares) are plotted against force. Discrete data points and curve as in (B). All measured data represent of 200-300 repetitions and error bars indicate standard deviation. Experimental data provided by Dr. Thomas Effertz.

The virtual fly ear

3.1.5.2 Harmonic oscillator with floating joint

As mentioned in the previous subsection, *tilB* and *nompA* mutations cause anatomical defects at the connection between the mechanosensory neurons and the antennal receiver. Notwithstanding these connection defects, their mechanical response to step stimulus display a creep towards the stationary state (Figure 33), which could not be explained only by K_{AJ} , but could be ascribed to floating of the entire pedicel. Therefore, an additional spring with stiffness K_y and friction constant λ_y was introduced to the model. The projected relative deflection of joint with respect to the enclosing pedicel Y is dependent on the arista deflection, X .

In addition to the creep of the displacement time traces, the mutant flies do not display the gating compliance and their receiver mechanics are completely linear (Figure 33). Following the law of succinctness, components accounting for the gating compliance in the 2-state model were removed, leading to a linear model, whose dynamics are described by

$$\begin{aligned}\dot{X} &= V \\ m\dot{V} &= -\lambda V - K_{AJ}X(1 + \text{Frac}_y) + F_{ext} \\ \lambda_y\dot{Y} &= -K_yY + K_{AJ}X,\end{aligned}$$

with $\text{Frac}_y = \frac{K_y}{K_{AJ}}$.

Here, Y denotes the projected relative deflection of the joint with respect to the pedicel. λ_y corresponds to the projected friction constant of the additional spring, and K_y to the additional combined stiffness. The new differential equation introduced two additional free parameters: K_y and τ_y , where $\tau_y = \frac{\lambda_y}{K_y}$, m, λ, K_{AJ}, K_y and τ_y are fit parameters.

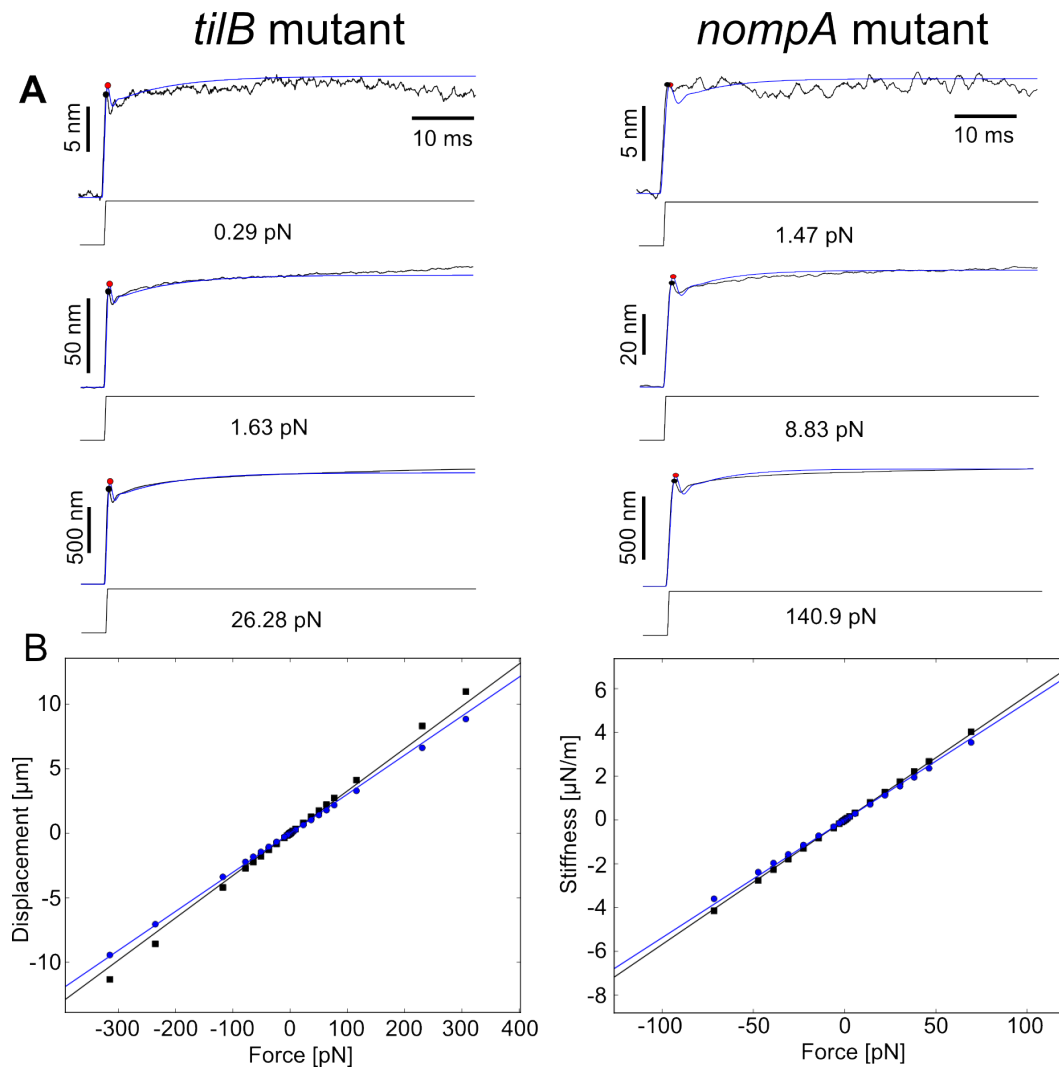


Figure 35: Fit results of *tilB* and *nompA* mutants with harmonic oscillator with floating joint

(A) Displacement time traces in response to step stimuli. Experimental data are shown in black, and simulated data are shown in blue. Detected stimulus onset peak displacements are marked as dots; black for experimental and red for simulated data. (B) Displacement-force relation for mutant of *tilB* and *nompA*, respectively. Onset peak displacements (blue) and steady-state displacement (black) are plotted against the corresponding force stimuli. Experimental data are shown as discrete data points, and simulated data are shown as curve. All measured data represent of 200-300 repetition. Experimental data provided by Dr. Thomas Effertz.

Fit results for *tilB* and *nompA* mutants (Figure 35) show that this linear model is sufficient to describe the receiver's force-displacement characteristics. Peak displacements and stationary displacements and also the creep of the receiver during maintained deflection were accurately reproduced.

The virtual fly ear

The assumption that the elasticity of the cuticle of the pedicel could affect the evolution of the displacement response, suggests that this floating motion of the antennal joint ought to exist in the sound receivers of wild-type flies as well, when the sound receiver is strongly actuated. However, this simple model fails to describe the channel opening and the associated gating-compliance (Figure 36). It is, therefore, necessary to implement another model, which includes not only the floating joint but also the nonlinearity of the onset peak displacements and adaptation motor activity.

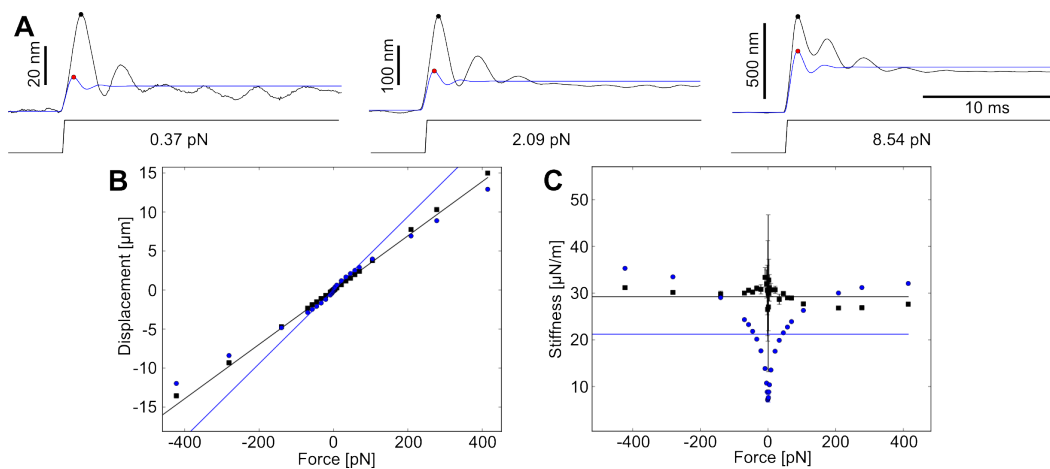


Figure 36: Fit results of wild-type fly with harmonic oscillator with floating joint

(A) Displacement time traces in response to step stimuli of CS wild-type fly. Experimental data are shown in black, and simulated data are shown in blue. Detected stimulus onset peak displacements are marked as dots; black for experimental and red for simulated data. (B) Displacement-force relation of CS wild-type fly. Onset peak displacements (blue) and steady-state displacement (black) are plotted against the corresponding force stimuli. Experimental data are shown as discrete data points, and simulated data are shown as curve. (C) Plot of slope stiffness against the corresponding force stimuli for CS wild-type fly. Experimental and simulated data are shown as in (B). All measured data represent of 200-300 repetitions and error bars indicate standard deviation.

3.1.5.3 The two-state model with floating joint

To introduce the floating joint into the two-state model, a spring was added by a series connection to the transducer modules on both sides, which accounts for the relative deflection of the whole Johnston's organ (JO) with respect to the pedicel (Figure 37). The property of this additional spring was described in previous subsection (3.1.5.2).

To this end, the differential equations were modified to:

$$\dot{X} = V$$

$$\lambda_a \dot{X}_a = K_{GS}(X - X_a - DP_o(X - X_a)) + F_{max}(SP_o(X - X_a) - 1)$$

$$\lambda_a \dot{X}_p = K_{GS}(-X - X_p - DP_o(X - X_p)) + F_{max}(SP_o(-X - X_p) - 1)$$

$$m\dot{V} = -K_{GS}(X - X_a - DP_o(X - X_a)) + K_{GS}(-X - X_p - DP_o(X - X_a)) - \lambda V \\ - K_{AJ}X(1 + Frac_y) + F_{ext}$$

$$\lambda_y \dot{Y} = -K_y Y + K_{AJ}X$$

The definition of the open probability remains unchanged. Due to the new differential equation, two new fit parameters, K_y and τ_y , (defined by $\tau_y = \frac{\lambda_y}{K_y}$), are appended to the list of fit parameters.

Using this model, wild type flies (Canton-S), *tilB* mutants and *nompA* mutants were fitted. Fit results of wild-type fly (Figure 38) showed improved fitness for moderate stimuli (10-150 pN). Yet, for the external forces that are larger than 150 pN, the onset peak displacements and stationary displacement at steady-state deviated. The force-displacement characteristics of *tilB* mutant were accurately reproduced. For *nompA* mutant, the nonlinearity of the model caused high

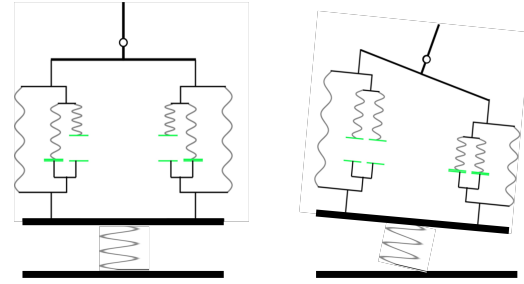


Figure 37: The cartoon of two-state model with floating antennal joint

A spring stiffness component was added to the two-state model, so that the relative deflection of the Johnston's organ can get explained. Adaptation motors are not shown.

The virtual fly ear

deviation for small stimuli ($F_{ext} < \sim 300$ pN). (For goodness of fits, please see section 3.2)

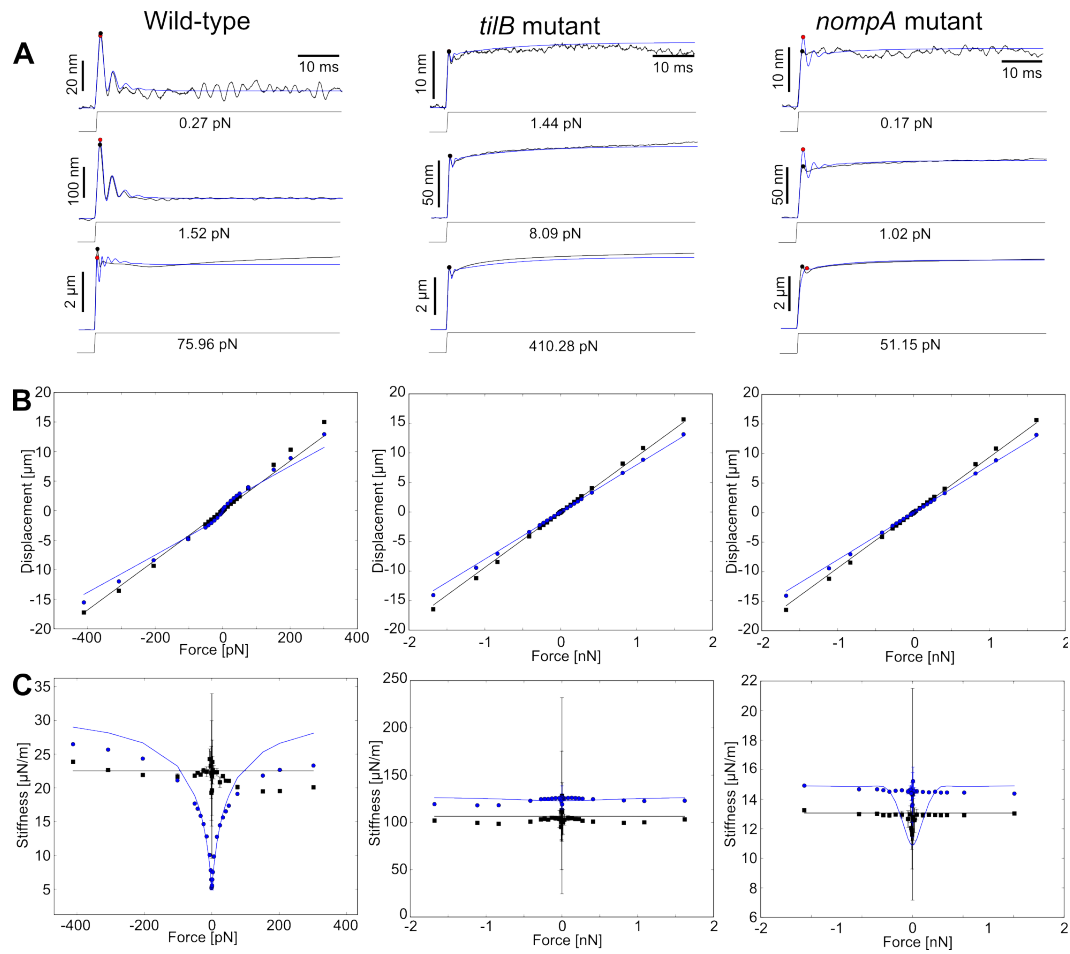


Figure 38: Fit results of wild-type fly, *tilB* mutant, and *nompA* mutant with two-state model with floating joint

(A) Displacement time traces in response to step stimuli. Experimental data are shown in black, and simulated data are shown in blue. Detected stimulus onset peak displacements are marked as dots; black for experimental and red for simulated data. (B) Displacement-force relation. Onset peak displacements (blue) and steady-state displacement (black) are plotted against the corresponding force stimuli. Experimental data are shown as discrete data points, and simulated data are shown as curve. (C) Plot of slope stiffness against the corresponding force stimuli. Experimental and simulated data are shown as in (B). All measured data represent of 200-300 repetitions and error bars indicate standard deviation. Experimental data provided by Dr. Thomas Effertz.

3.1.5.4 The two-state model with nonlinear parallel stiffness

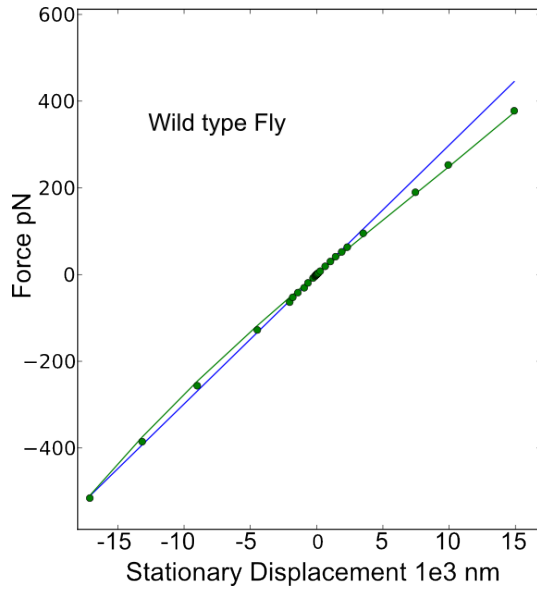


Figure 39: Stimulus forces plotted against stationary displacement

The forces of step stimuli were plotted against measured stationary displacement (green dots). Fit curve with linear stiffness (blue line) and nonlinear-elastic function (green line) were plotted as well.

($K_{AJ}=0.02985\text{pN/nm}$ obtained from fit with two-state model; $K_1=0.02560\text{pN/nm}$, $K_2=-1.32737\text{e-}7\text{pN/nm}^2$, $K_3=6.52496\text{e-}12\text{pN/nm}^3$ obtained from fit with nonlinear model.) Experimental data provided by Dr. Thomas Effertz.

The two-state model assumes that the parallel stiffness due to the antennal joint (symbolized by a parallel spring in Figure 29) is linear-elastic following the Hooke's law. However, biological processes usually involve nonlinear elastic functions, which, in effect, show a slight nonlinearity (Figure 39). This also applies to the flies' system.

To describe this nonlinearity, a simple nonlinear elastic function is introduced defined as:

$$F = K_1X + K_2X^2 + K_3X^3.$$

After substituting $K_{AJ}X$ of the two-state model with the nonlinear function, the dynamical differential equations read:

$$\begin{aligned} \dot{X} &= V \\ \lambda_a \dot{X}_a &= K_{GS}(X - X_a - DP_o(X - X_a)) + F_{max}(SP_o(X - X_a) - 1) \\ \lambda_a \dot{X}_p &= K_{GS}(-X - X_p - DP_o(X - X_p)) + F_{max}(SP_o(-X - X_p) - 1) \\ m\dot{V} &= -K_{GS}(X - X_a - DP_o(X - X_a)) + K_{GS}(-X - X_p - DP_o(X - X_a)) - \lambda V \\ &\quad - K_1X - K_2X^2 - K_3X^3 + F_{ext} \end{aligned}$$

The definition of the open probability remains unchanged. In the new model, parameters K_1 , K_2 and K_3 replace K_{AJ} as new fit parameters in the model.

The virtual fly ear

In comparison with the fit with the two-state floating joint model (Figure 38, wild-type), the results of the fit to experimental data of the same wild-type fly (CS) revealed remarkably improved fitness for the force-displacement relation (Figure 39) and force-stiffness relation (Figure 40 B). Both the gating compliance and the stationary nonlinearity are better described, even for large scale of stimulus forces (Figure 40 B). The temporal evolution of the time traces is also well reproduced (Figure 40 A).

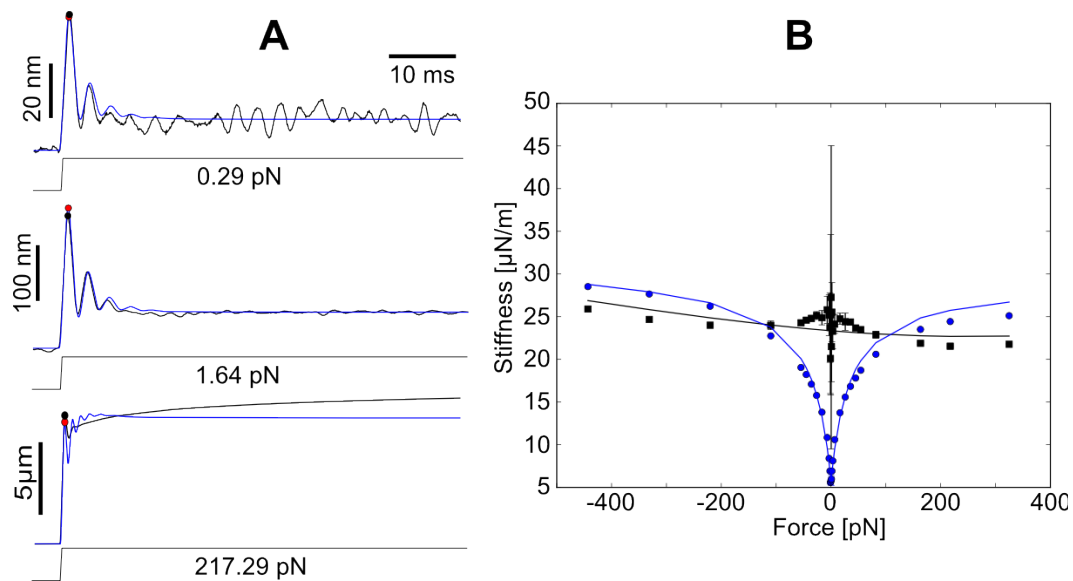


Figure 40: Fit results of wild-type fly with two-state model with nonlinear parallel stiffness

(A) Displacement time traces in response to step stimuli. Experimental data are shown in black, and simulated data are shown in blue. Detected stimulus onset peak displacements are marked as dots; black for experimental and red for simulated data. (B) Plot of slope stiffness against the corresponding force stimuli. Stiffness at onset displacement peak (blue) and at steady-state (black) are plotted against the corresponding force stimuli. Experimental data are shown as discrete data points, and simulated data are shown as curve. All measured data represent of 200-300 repetitions and error bars indicate standard deviation. Experimental data provided by Dr. Thomas Effertz.

3.1.5.5 The four-state model

To model both the NompC-dependent and -independent channel types, the 2nd channel type was introduced [97] (section 1.7.1).

With this additional transducer channel, a total of four states are assumed: (1) both channels open, (2) both channel types closed, (3) first channel type open and second channel type closed, (4) first channel type closed and second channel type open. To model both the mechanotransduction channels, two additional differential equations were introduced. Thus, the model's dynamics for the four-state model reads:

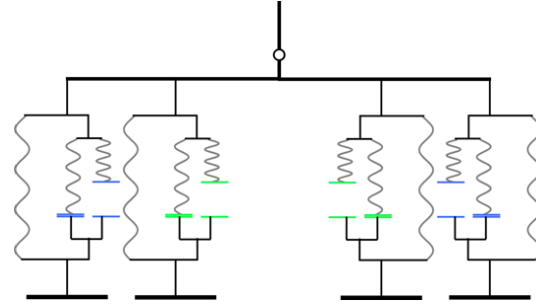


Figure 41: The cartoon of four-state model for *Drosophila* hearing organ

The 2nd gating-spring modules (blue) were introduced beside the first mechanotransduction channels (green). The new model assumes a total of 4 states. Adaptation motors are not shown.

$$\dot{X} = V$$

$$\begin{aligned} m\dot{V} = & -K_{GS}(X - X_a - DP_o(X - X_a)) + K_{GS}(-X - X_p - DP_o(X - X_a)) \\ & - K_{GS2}(X - X_{a2} - D_2P_{o2}(X - X_{a2})) \\ & + K_{GS2}(-X - X_{p2} - D_2P_{o2}(X - X_{a2})) - \lambda V - K_{AJ}X + F_{ext} \end{aligned}$$

$$\lambda_a \dot{X}_a = K_{GS}(X - X_a - DP_o(X - X_a)) + F_{max}(SP_o(X - X_a) - 1)$$

$$\lambda_a \dot{X}_p = K_{GS}(-X - X_p - DP_o(X - X_p)) + F_{max}(SP_o(-X - X_p) - 1).$$

$$\lambda_{a2} \dot{X}_{a2} = K_{GS2}(X - X_{a2} - D_2P_{o2}(X - X_{a2})) + F_{max2}(S_2P_{o2}(X - X_{a2}) - 1)$$

$$\begin{aligned} \lambda_{a2} \dot{X}_{p2} = & K_{GS2}(-X - X_{p2} - D_2P_{o2}(X - X_{p2})) \\ & + F_{max2}(S_2P_{o2}(-X - X_{p2}) - 1). \end{aligned}$$

The virtual fly ear

Along with these two differential equations, 4 free parameters were introduced for the 2nd channel: K_{GS2} , λ_{a2} , S_2 , N_2 , with respective meanings as for the first channel. D_2 and F_{max2} were calculated using equation 19 and equation 24 (in section 3.1.5.6), and the definition of the channel open probability reads:

$$P_{02}(Y) = \frac{1}{1 + A_2 e^{-\frac{Y}{\delta_2}}}$$

with:

$$\delta_2 = \frac{N_2 k_B T}{K_{GS2} D_2},$$

$$A_2 = e^{\frac{\Delta G_2 + K_{GS2} D_2^2 / (2N_2)}{k_B T}}.$$

To fit the mechanics of the wild-type (Canton-S) fly's sound receiver with the four-state model, fit parameters from the *nompC* mutant have been set as the initial parameters for the second transduction channel, so that searching for the local minimum began closely to the parameter set of the fit with *nompC* mutant. The fit results (Figure 42) do not display remarkable improvement in comparison to the fit results with two-state model (Figure 32). In section 3.2, the "goodness" of fits will be compared quantitatively by using the Akaike's Information Criterion (AIC).

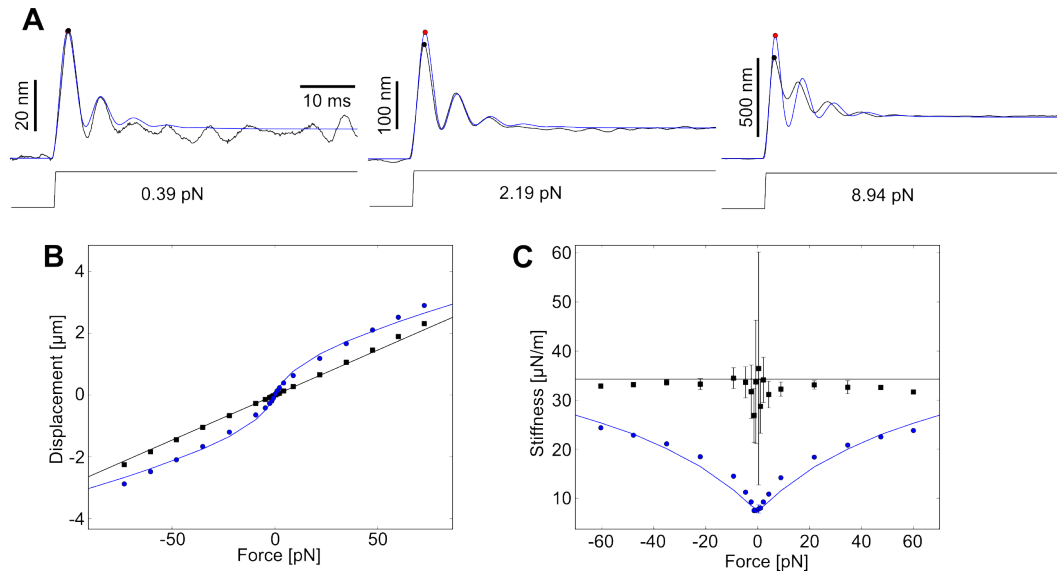


Figure 42: Fit results of wild-type fly with four-state model

(A) Displacement time traces in response to step stimuli of CS wild-type fly. Experimental data are shown in black, and simulated data are shown in blue. Detected stimulus onset peak displacements are marked as dots; black for experimental and red for simulated data. (B) Displacement-force relation of CS wild-type fly. Onset peak displacements (blue) and steady-state displacement (black) are plotted against the corresponding force stimuli. Experimental data are shown as discrete data points, and simulated data are shown as curve. (C) Plot of slope stiffness against the corresponding force stimuli for CS wild-type fly. Experimental and simulated data are shown as in (B). All measured data represent of 200-300 repetitions and error bars indicate standard deviation. Experimental data provided by Dr. Thomas Effertz.

3.1.5.6 Stationary states

To evaluate of the dynamics of each model, I first analyzed the stationary state of the corresponding model. Stationary states with or without stimulus were calculated analytically by the following relations:

$$X_s = \frac{F_{ext}}{K_{AJ}} \quad (22)$$

and

$$X_{p,s} = -2X_s + X_{a,s}, \quad (23)$$

where X_s is the displacement at the stationary state and $X_{a,s}$ is a solution of

The virtual fly ear

$$P_{o,s} = P_o(X_s - X_{a,s}) = \frac{K_{GS}(X_s - X_{a,s}) - F_{max}}{K_{GS}D - F_{max}S}. \quad (24)$$

Equation 24 can have 1 to 3 solutions, because the Boltzmann-like function (left side of the equation) and the linear function (right side of the equation) can have 1 to 3 intersections. Solutions referring to unstable states were discarded.

3.1.5.7 Stochastic noise sources for simulations of free fluctuation

For simulations with noise in the background, stochastic forces were added to the model equations. The influence of stochastic forces on the dynamical movements of the sound receiver was taken into account by adding noise terms to the equations describing the dynamics of the harmonic oscillator and the adaptation motors. For instance, the equations of the two-state model (see section 3.1.5.1) was altered into

$$\begin{aligned} \dot{X} &= V \\ \lambda_a \dot{X}_a &= K_{GS}(X - X_a - DP_o(X - X_a)) + F_{max}(SP_o(X - X_a) - 1) + \eta_a \\ \lambda_a \dot{X}_p &= K_{GS}(-X - X_p - DP_o(X - X_p)) + F_{max}(SP_o(-X - X_p) - 1) + \eta_p \\ m\dot{V} &= -K_{GS}(X - X_a - DP_o(X - X_a)) + K_{GS}(-X - X_p - DP_o(X - X_a)) - \lambda V \\ &\quad - K_{AJ}X + F_{ext} + \eta, \end{aligned}$$

where η_a, η_p and η are the stochastic noise terms having zero mean. The characteristics of these noise terms following fluctuation-dissipation theorem [43] are defined as [44]

$$\langle \eta(t)\eta(0) \rangle = 2k_B T \lambda \delta(t)$$

$$\langle \eta_a(t)\eta_a(0) \rangle = 2k_B T \lambda_a \delta(t)$$

$$\langle \eta_p(t)\eta_p(0) \rangle = 2k_B T \lambda_a \delta(t)$$

where the brackets are the autocorrelation operator and δ the delta-function.

3.1.5.8 *Fitting procedure and the cost-function*

Individual fits were performed by numerically integrating the corresponding model equations for a single force step of given amplitude and polarity and by comparing predicted and measured receiver displacements. Depending on the program configuration chosen by the user, the measurement points used for the fits were distributed logarithmically or linearly. When logarithmically distributed, the density of points gradually decreased from the beginning to the end of the step. When linearly distributed, the points scattered uniformly.

The cost-function used for individual fit of single force step was

$$\sum_{i=1}^{N_p} \frac{(S_i - Y_i)^2}{N_p}, \quad (25)$$

where N_p is the number of the measured points and S_i and Y_i are simulated and measured receiver displacement, respectively.

More general fits were performed by simultaneously fitting the displacement responses to multiple force steps chosen by the user in program (typically 10 smallest steps with peak displacement < 800 nm for small range fitting and all 28 steps for large range fitting), the linear response function and the power spectral density of the free fluctuations. The predicted values of the linear response function and the power spectral density were analytically calculated for reduction of program run time. The simulation of the power spectral density was performed analytically as well with the noise defined in the subsection 3.1.5.7.

The cost-function for the general fit was defined as

The virtual fly ear

$$\begin{aligned}
 W_s & \left(\sum_{i=1}^{N_S} \frac{\sum_{j=1}^{N_{i,p}} \left(\frac{S_{i,j} - Y_{i,j}}{E_{S,i,j}} \right)^2}{N_{i,p}} \frac{1}{P_i^2} \right) \frac{\sum_{i=1}^{N_S} P_i^2}{N_S} \\
 & + W_\chi \left(\frac{\sum_{k=1}^{N_\chi} \left(\frac{\tilde{\chi}'_{0,c}(f_k) - \tilde{\chi}'_0(f_k)}{E_{\chi',k}} \right)}{N_\chi} + \frac{\sum_{k=1}^{N_\chi} \left(\frac{\tilde{\chi}''_{0,c}(f_k) - \tilde{\chi}''_0(f_k)}{E_{\chi'',k}} \right)}{N_\chi} \right) \\
 & + W_C \frac{\sum_{l=1}^{N_C} \left(\frac{\tilde{C}_C(f_l) - \tilde{C}(f_l)}{E_{C,l}} \right)}{N_C}.
 \end{aligned}$$

Here, N_S is the number of force steps, $N_{i,p}$ is the number of measured points in step i , $S_{i,j}$ and $Y_{i,j}$ are the simulated and measured receiver displacement for point j in step i , P_i is the peak displacement in response to step i , W_s is the weight of steps fitting and $E_{S,i,j}$ is the standard error of the j -th measured point in step i . Furthermore, $\tilde{\chi}_{0,c}$ is the linear response function calculated for the corresponding model, N_χ is the number of points used for fitting the linear response function, $E_{\chi',k}$ and $E_{\chi'',k}$ are the standard error of the real part and imaginary part of the measured linear response function at point k and W_χ is the weight for fitting the linear response function. Similarly for the power spectral density, \tilde{C}_C is the calculated power spectral density of free fluctuation, N_C is the number of measurements of power spectral density, E_C and W_C are the standard error of measured points and the weight for the power spectral density fitting.

As mentioned in previous subsections, the initial guess of the parameters were generated randomly and the Nelder-Mead Simplex were used for minimizing the value of cost-function. The parallel and single threaded implementations were stored in the Python package “vfit”.

3.2. Model selection and Akaike's information criterion

3.2.1 Akaike's Information Criterion (AIC).

To assess the “goodness” of a fit, various numerical measures can be used. A simple and straightforward way is to calculate the cost-function (section 3.1.5.8). Yet, the value of cost-function does not take the number of free parameters into account. A problem arises when different models are compared: the model with more free parameters usually fits the data better, tending to produce better cost-function value, which eventually causes overfitting.

When selecting a model, overfitting can be prevented by using measure for goodness of fit that takes the number of free parameters into account. One of such measures is the Akaike's Information Criterion (AIC). The AIC is defined as

$$AIC = -2 \ln(\text{likelihood}) + 2k,$$

where (*likelihood*) is the probability that the data is exactly reproduced by the model and k is the number of free parameters in the model. AIC can be calculated using residual sums of squares from regression:

$$AIC = n \ln \left(\frac{RSS}{n} \right) + 2k,$$

where n is the number of data points (observations), and RSS is the residual sum of squares. RSS is calculated by

$$RSS = \sum_{i=0}^n (y_i - f_i)^2,$$

with f denoting the simulated value and y denoting the measured value.

For infinite sample sizes, it is highly recommended by Burnham & Anderson [98] to use the AIC with bias adjustment (AIC_c: corrected AIC):

$$AIC_c = -2 \ln(\text{likelihood}) + 2k + \frac{2k(k+1)}{n-k-1}.$$

Hence, the AIC used to compare the models is calculated as

Model selection and Akaike's information criterion

$$AIC_c = -n \ln \left(\frac{RSS}{n} \right) + 2k + \frac{2k(k+1)}{n-k-1}.$$

The AICc makes it possible to compare fits from different models that have a different number of parameters. The model with the lowest AICc can be selected as the model that explains the data best without overfitting.

A better means of interpreting the AICs is to normalize the relative likelihood value as:

$$w_i = \frac{L_{R,i}}{\sum_{i=1}^m L_{R,i}},$$

where $L_{R,i}$ is the relative likelihood of model i (from m models), which is defined as:

$$L_{R,i} = e^{-0.5\Delta_i}.$$

Here, Δ_i is the difference between the AICc values of model i and of the best model, i.e. $\Delta_i = AICc_i - AICc_{min}$.

w_i is the weight of the evidence that model i is the model that describes the data best, given the data and set of candidate models. Alternatively, the w_i can be interpreted as the ratio of likelihood for model i .

3.2.2 Model selection by using AIC

The mechanical response of the fly's sound receiver includes the initial overshoot, the rebound and damped oscillation, and the steady-state. The initial displacement peak displays nonlinear relation to the external force, which is a good measure for the existence of gating-compliance, i.e. the channel activity, while the stationary displacement at steady-state is an indicator of the passive properties, when the adaptation motors and active processes of the neurons in JO reach their stationary state. We, therefore, choose both these measures for comparing the models based on the goodness of fits.

3.2.2.1 Selecting model for wild-type flies

The AICs of wild-type fly (Canton-S) are calculated for the slope stiffness at initial displacement peak and for the stationary state separately (Table 6 and Table 7). Both results indicate that, among the different models examined, the two-state model provides the best fits.

Table 6: Model selection for initial displacement peak of wild-type fly's sound receiver

Model	K	AICc	Δ_i	$L_{R,i}$	w_i
Two-state	9	-289.51	0	1	0.9999
SHO with floating joint	5	-197.28	92.24	9.36e-21	9.36e-21
Two-state with floating joint	11	-254.26	35.25	2.22e-8	2.22e-8
Two-state with nonlinear parallel stiffness	11	-267.18	22.33	1.41e-5	1.41e-5
Four-state	14	-186.13	103.39	3.5e-23	3.55e-23

Table 7: Model selection for stationary state of wild-type fly's sound receiver

Model	K	AICc	Δ_i	$L_{R,i}$	w_i
Two-state	9	-272.24	0	1	0.9999
SHO with floating joint	5	-244.61	27.63	9.97e-7	9.99e-7
Two-state with floating joint	11	-228.21	44.03	2.74e-10	2.74e-10
Two-state with nonlinear parallel stiffness	11	-217.47	54.77	1.28e-12	1.28e-12
Four-state	14	-171.96	100.28	1.67e-22	1.67e-22

Model selection and Akaike's information criterion

3.2.2.2 Model selection - *tilB* mutants

Three models were applied to the *tilB* mutants. According to the AIC calculation (Table 8 &

Table 9), the simple harmonic oscillator model with floating joint fits the initial displacement peak best, whereas the stationary state is best fitted by the two-state model, although with the simple harmonic oscillator model with floating joint, also good result were obtained (Table 9).

Table 8: Model selection for initial displacement peak of *tilB* mutant's sound receiver

Model	K	AICc	Δ_i	$L_{R,i}$	w_i
Two-state	9	-281.20	51.99	5.14e-12	5.14e-12
SHO with floating joint	5	-333.18	0	1	1
Two-state with floating joint	11	-283.50	49.68	1.63e-11	1.62e-11

Table 9: Model selection for stationary state of *tilB* mutant's sound receiver

Model	K	AICc	Δ_i	$L_{R,i}$	w_i
Two-state	9	-337.47	0	1	0.76
SHO with floating joint	5	-335.14	2.33	0.31	0.24
Two-state with floating joint	11	-243.82	93.65	4.62e-21	3.52e-218

3.2.2.3 Selecting model for *nompA* mutants

As for the *tilB* mutants, three models were also applied to describe auditory mechanics in *nompA* mutants. AIC identified the simple harmonic oscillator model with floating joint as the best model both for the initial displacement peak and for the stationary state (Table 10 and Table 11).

Table 10: Model selection for initial displacement peak of *nompA* mutant's sound receiver

Model	K	AICc	Δ_i	$L_{R,i}$	w_i
Two-state	9	-187.80	98.5438	3.99e-22	3.99e-22
SHO with floating joint	5	-286.35	0	1	1
Two-state with floating joint	11	-217.42	68.9238	1.08e-15	1.08e-15

Table 11: Model selection for stationary state of *nompA* mutant's sound receiver

Model	K	AICc	Δ_i	$L_{R,i}$	w_i
Two-state	9	-202.69	102.93	4.45e-23	4.45e-23
SHO with floating joint	5	-305.62	0	1	0.99
Two-state with floating joint	11	-281.29	24.33	5.2e-6	5.2e-6

Assessment of active process by calculation of energy flux

3.3. Assessment of active process by calculation of energy flux

Hearing in insects and vertebrates relies on active processes that improve the sensitivity and frequency selectivity [27, 99-101]. The mechanosensory neurons in the *Drosophila* ear actively pump energy into sound-induced vibration of the fly's receiver. This vulnerable physiological mechanism is suppressed when the animal is anesthetized by exposure to CO₂ [27].

In this subsection, an approach is presented to quantify the active energy flux in the fly's ear. The approach is based on the comparison of receiver fluctuations in anesthetized and unanesthetized flies and takes the advantage of the fact that fluctuations of the "passive" receiver of anesthetized flies can be described by a simple harmonic oscillator model [28].

3.3.1 The fluctuation of sound receiver of anesthetized fly

The free fluctuations of a wild type receiver were measured before and during anesthetization with CO₂. After exposure to CO₂ with 20s, the mechanics of the sound receiver reversibly linearizes and the active energy contributions are lost.

The flies were measured near the tip of the arista. In absence of the external stimulation, the fluctuation of the antennal receiver of an unanesthetized fly displayed spontaneous, irregular, noisy twitches, which disappeared after anesthetization (Figure 43, Vibration). With the model of a harmonic oscillator, the PSD of this latter, passive fluctuation was well fitted (Figure 43, PSD).

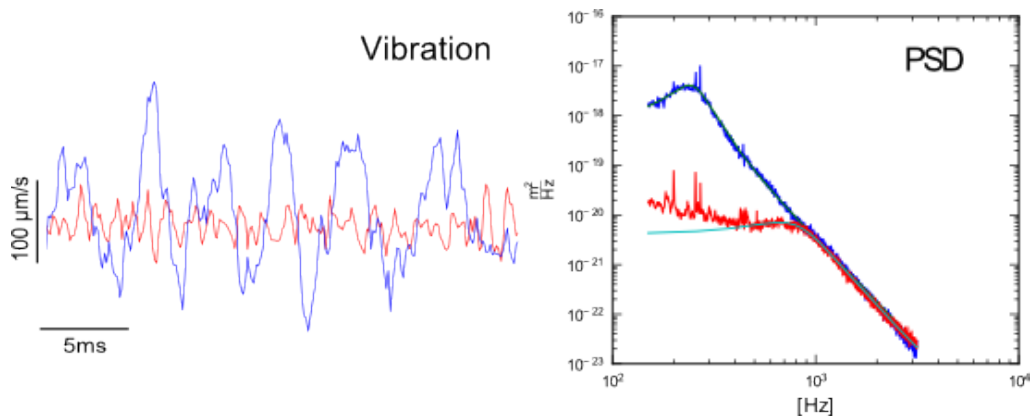


Figure 43: Mechanical fluctuation of the antennal sound receiver and corresponding PSD

Left panel: Time traces of the velocity of the anesthetized (red) and unanesthetized (blue) receiver. Right panel: The corresponding PSDs (red for the anesthetized receiver and blue for the unanesthetized receiver). The PSDs are fitted with a simple harmonic oscillator model (straight lines), turquoise line for the fit curve of anesthetized receiver and green line for the unanesthetized receiver.

3.3.2 The active and passive components betrayed by the sound receiver

By comparing the PSDs before and during anesthetization, the forcing acting on the sound receiver due to the active process of the auditory neurons can be isolated from the fluctuations.

For an unanesthetized receiver, the total driving force experienced by the receiver, $\langle |\eta_\omega|^2 \rangle$, can be described by

$$\langle |\eta_\omega|^2 \rangle = \langle |\eta_a|^2 \rangle + \langle |\eta_0|^2 \rangle. \quad (26)$$

Here, η_a corresponds to the forcing due to the active process and η_0 is the forcing due to thermal bombardment.

When the fly is anesthetized, the active process is reversibly lost, i.e. $\langle |\eta_a|^2 \rangle = 0$. The total force experienced by the sound receiver is thus described by $\langle |\eta_\omega|^2 \rangle = \langle |\eta_0|^2 \rangle$.

Assessment of active process by calculation of energy flux

Following the harmonic oscillator equation, the power spectral density of the fluctuation of the fly's receiver can be rewritten as:

$$\langle |X_\omega|^2 \rangle = \frac{\langle |\eta_\omega|^2 \rangle}{(K - m\omega^2)^2 + \gamma^2 \omega^2} \quad (27)$$

and

$$\langle |\eta_\omega|^2 \rangle = \langle |X_\omega|^2 \rangle ((K - m\omega^2)^2 + \gamma^2 \omega^2). \quad (28)$$

Here, $1/((K - m\omega^2)^2 + \gamma^2 \omega^2)$ corresponds to the passive component, which can be calculated by the fit parameters deduced for the anesthetized receiver. $\langle |X_\omega|^2 \rangle$ contains information about the active and the passive components.

The active forcing term $|\eta_a|^2$ can be deduced by measuring the PSDs of the unanesthetized receiver and the anesthetized receiver and calculating the amplitude difference in the frequency domain:

$$\begin{aligned} \langle |\eta_a|^2 \rangle = & ((K - m\omega^2)^2 + \gamma^2 \omega^2) (\langle |X_{\omega, \text{unanesthetized}}|^2 \rangle \\ & - \langle |X_{\omega, \text{anesthetized}}|^2 \rangle) \end{aligned} \quad (29)$$

3.3.3 The dissipation rate spectrum

For the fly's receiver, the forcing term due to the thermal noise and the active process can be described by

$$F(t) = F_0 e^{i\omega t} + c. c. ,$$

and its displacement can be described by

$$X(t) = X_0 e^{i\omega t} + c. c. .$$

The velocity, i.e. the derivative of the displacement, is described by

$$\dot{X}(t) = i\omega (X_0 e^{i\omega t} - c. c.).$$

Here, $F(t)$ is the force acting on the sound receiver and $X(t)$ is the resulting displacement response. F_0 and X_0 are the amplitudes of the periodical force and displacement, respectively. $c.c.$ denotes the complex conjugate of the complex number.

The dissipation rate of the sound receiver is calculated as following:

$$\begin{aligned}\dot{\theta}(\omega) &= \frac{1}{T} \int_0^T F(t) \cdot \dot{X}(t) dt \\ \dot{\theta}(\omega) &= \frac{1}{T} \int_0^T i\omega(F_0 e^{i\omega t} + c.c.)(X_0 e^{i\omega t} - c.c.) dt \\ \dot{\theta}(\omega) &= \frac{1}{T} \int_0^T i\omega(F_0 X_0 e^{2i\omega t} + F_0^* X_0 - F_0 X_0^* - F_0^* X_0^* e^{-2i\omega t}) dt \\ \dot{\theta}(\omega) &= \frac{1}{T} \int_0^T [i\omega(F_0^* X_0 - c.c.) + i\omega(F_0 X_0 e^{2i\omega t} - c.c.)] dt \\ \dot{\theta}(\omega) &= \frac{1}{T} \int_0^T i\omega(F_0^* X_0 - c.c.) dt + \frac{1}{T} \int_0^T i\omega(F_0 X_0 e^{2i\omega t} - c.c.) dt\end{aligned}$$

where $\dot{\theta}(\omega)$ denotes the dissipation rate spectrum as a function of frequency and T is the time window of the Fourier transform.

When the time window T equals to multiples of half the forcing frequency, i.e. $T = n \cdot \frac{\omega}{2}, n = 1, 2, 3 \dots$, the equation simplifies to $\frac{1}{T} \int_0^T i\omega(F_0 X_0 e^{2i\omega t} - c.c.) dt = 0$. The dissipation rate, therefore, can be further deduced as:

$$\begin{aligned}\dot{\theta}(\omega) &= \frac{1}{T} \int_0^T i\omega(F_0^* X_0 - c.c.) dt \\ \dot{\theta}(\omega) &= \frac{1}{T} i\omega(F_0^* X_0 - c.c.) \int_0^T dt \\ \dot{\theta}(\omega) &= i\omega(F_0^* X_0 - c.c.)\end{aligned}$$

According the definition of the linear response function $X_0 = \chi F_0$, we obtain:

Assessment of active process by calculation of energy flux

$$\dot{\theta}(\omega) = i\omega(\chi|F_0^2| - c.c.) = 2\omega\text{Im}(\chi)|F_0^2|$$

This calculated dissipation rate spectrum describes the power dissipated by the sound receiver per Hz. Because the passive component of the fluctuation of the sound receiver was isolated (section 3.3.2) and the force source has been described (equation 26), the dissipation rate spectrum due to the active process that is betrayed by the vibration of the sound receiver can be deduced as

$$\dot{\theta}(\omega) = \frac{-2\gamma\omega^2}{(K - m\omega^2)^2 + \gamma^2\omega^2} (|\eta_\omega|^2 - |\eta_0|^2). \quad (30)$$

Hence, the energy flux due to the active process, which is macroscopically betrayed by the fluctuation of the sound receiver, can be deduced as the integral of the dissipation rate spectrum over all frequencies.

$$\dot{\theta} = \int \dot{\theta}(\omega)d\omega$$

And it holds the unit [J/s].

This calculation is demonstrated in the Figure 44 by the results of 3 wild type flies (Canton-S).

3.3.4 Energy flux during the fluctuation of the sound receiver

In this experiment, the PSDs of the sound receivers of the anesthetized receiver and the unanesthetized receiver were measured subsequently. The PSDs were fitted with equation 5. The fit parameters of the anesthetized fly were used for calculating the passive components described in section 3.3.2. The parameters deduced from the fit to the unanesthetized receiver fluctuations were used for integrating over the frequencies. The total forcing η_ω was calculated according to the equation 29. Note, the η_ω of the anesthetized receiver contained only the thermal force. The force due to the active process of the auditory neurons was

isolated by subtracting the force due to thermal noise η_0 from η_ω , i.e. $\eta_{\omega,unanethetized} - \eta_{\omega,anethetized}$. Subsequently, the dissipation rate spectra were calculated by using the equation 30. At the end, the dissipation rate, which is a measure of the energy flux, was calculated by integrating the dissipation rate spectra over frequencies from 0 Hz to 3000 Hz (Table 12). In this table, dissipation is shown as multiple of $k_B T$ (k_B stands for Boltzmann constant and T for environmental temperature).

Assessment of active process by calculation of energy flux

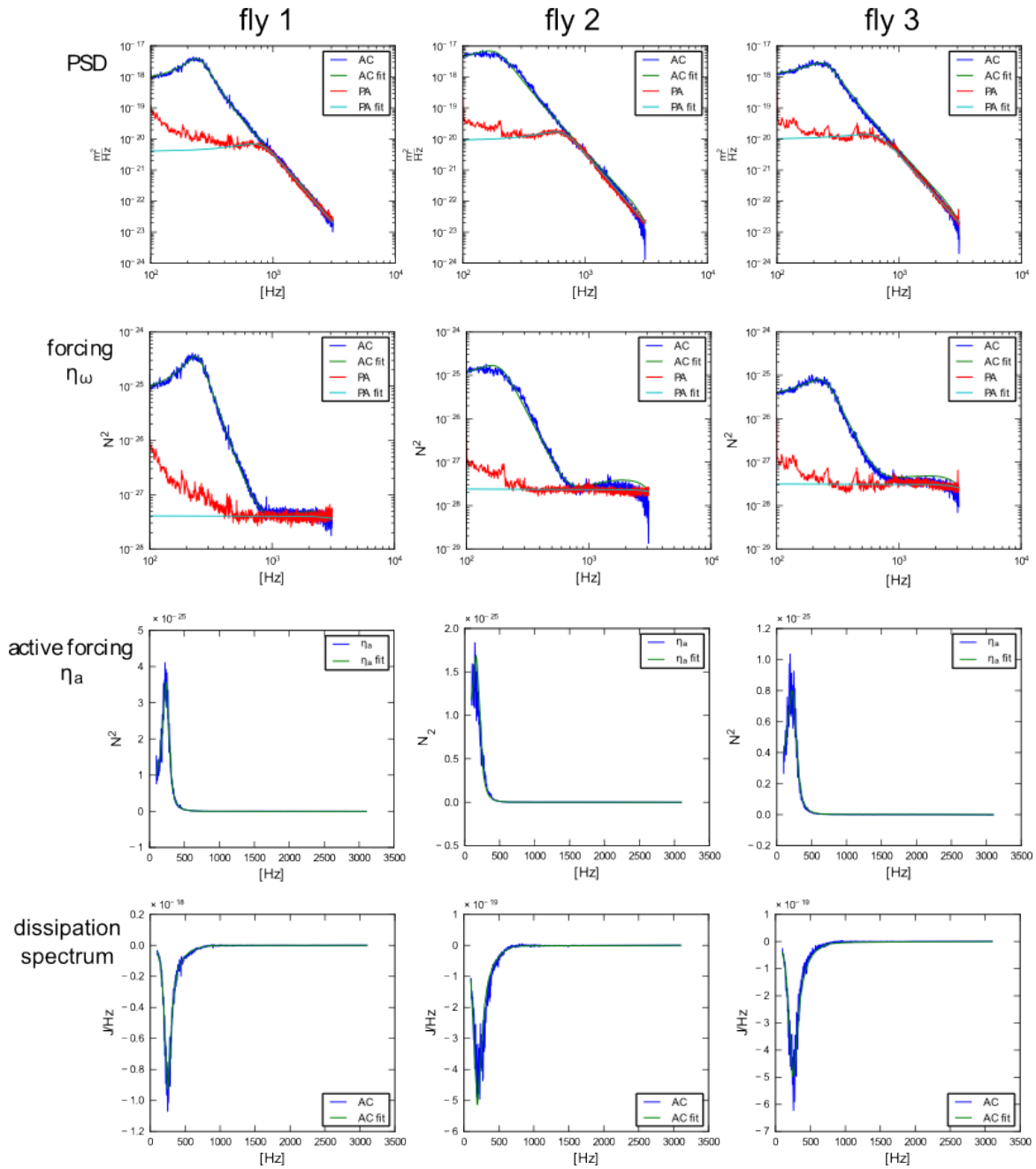


Figure 44 dissipation rate spectrum during fluctuation of the sound receiver

The dissipation spectra of 3 wild type flies were calculated. For each fly, the PSD of the free fluctuation of the anesthetized (red lines) and the unanesthetized (blue lines) receiver was fitted and plotted.

The total forcing including the thermal noise and the active process of the auditory neurons of the unanesthetized receiver was calculated (according to the equation 26), fitted and plotted. The forcing due to the active process was calculated using equation 30 and fitted. At the end the dissipation spectra were calculated and fitted. Note that negative dissipation means the sound receiver is absorbing energy from the environment. Legend AC denotes the data of unanesthetized receiver; PA the data of anesthetized receiver. Experimental data provided by Dr. Thomas Effertz.

Table 12: Fit parameters and the dissipation rates of measured flies

	m [kg]	γ [kg/s]	K [N/m]	Dissipation rate [k_BT/s]	Dissipation rate from fit [k_BT/s]
Fly 1	1.179e-11	5.093e-08	0.00031814	-36251.4	-37262.5
Fly 2	8.875e-12	2.995e-08	0.000162415	-22689.2	-23574
Fly 3	9.684e-12	3.939e-08	0.00017787	-23899.8	-26404.6
mean	1.01e-11±0.12e-11	4.01e-8±0.86e-8	2.19e-4±0.7e-4	-2.76e4±0.61e4	-2.91e4±0.59e4

According to the Table 12, for the animals shown we obtain dissipation rates due to active process of $2.91e4$ k_BT/s. The hydrolysis of 1 ATP yields an energy equivalent of 15 to 20 k_BT, so the $2.91e5$ k_BT/s translates into ca. 1455-1940 ATP/s for the active animals. The energy provided by a single molecular motor corresponds to ca. 100-1000 ATP/s, so 1-19 motors would be sufficient to generate the active energy flux observed in flies. The results could show that only tiny amount of the energy was fed into the antenna by the auditory neurons.

3.3.5 Energy flux and frequency tuning during sound stimulation

After assessing the energy flux during the free fluctuation of the sound receiver, the energy flux and the frequency tuning were investigated when the sound receiver was acoustically stimulated with pure tones. External stimulus forces can cause active receiver vibrations suggesting that the active energy emitted by the auditory neurons and dissipated by the sound receiver might redistribute and be tuned to the stimulus frequency in the presence of sound.

In this experiment, the fly's receiver was exposed to tones at the best frequency of fluctuations in the unanesthetized state. The tone intensity was varied in a range of 90 dB. During stimulation, the PSDs were measured alternatively in the unanesthetized and anesthetized states. These PSDs were fitted as described in section 2.3.4.1 and the apparent forces of the pure tone stimuli were estimated as described in section 2.3.4.2. For each stimulus intensity, the total driving force η_ω , the force due to the active process η_a , the dissipation rate spectrum $\dot{\theta}_\omega$, and

Assessment of active process by calculation of energy flux

the dissipation rate $\dot{\theta}$ were calculated as described in section 3.3.4. The results are shown in the left panel of Figure 45. For reasons of clarity, only data obtained from the fly 1 at a stimulus intensity of 60 fN (apparent force of the pure tone) is shown. Data of fly 2 and fly 3 can be found in the Appendix B. For fly 1, the stimulus frequency was 262 Hz, which is the best frequency of its antennal sound receiver in unanesthetized state. When anesthetized, the fly's sound receiver displayed a best frequency at 595 Hz. 14 stimulus intensities were tested. To investigate the frequency tuning of the active component, the stimulus frequency was neglected when calculating the dissipation rate spectrum (from 100 Hz to 3000 Hz). As shown in the right panel of Figure 45, the active energy, which appears as a negative dissipation, declined at frequencies other than the stimulus frequency when the stimulation intensity was raised. And the frequency with minimal dissipation rate (i.e. maximal active energy) shifted from 262 Hz, the best frequency observed in the unanesthetized state, to 595 Hz, the best frequency in the anesthetized state.

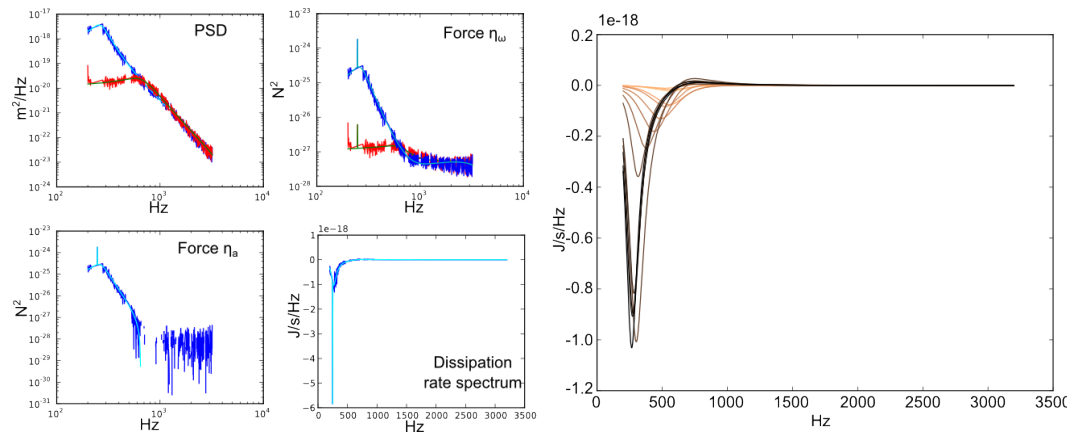


Figure 45: Dissipation rate spectrum of the sound receiver during sound-induced vibration

Left panel: The PSD of the sound-induced vibration was measured and fitted. Force η_ω and η_a and the dissipation rate spectrum was calculated and fitted (the measured data of the fly at anesthetized state were colored red and its fit data were colored green; the measured data of the fly at unanesthetized state were colored blue and its fit data in turquoise.)

Right panel: The dissipation rate spectra of 14 stimulus intensities were plotted. The spectrum at the lowest stimulus intensity (apparent force = 60 fN) was colored black and the spectrum resulted from the highest stimulus intensity (apparent force=25 pN) was colored light orange. Spectra of the other stimuli were colored according to the color gradient.

Data shown were measured with wild type fly Canton-S (fly 1); for left panel, the apparent force of the pure tone stimulus was 60 fN. Experimental data provided by Dr. Thomas Effertz.

The dissipation rate was calculated by integrating the dissipation rate spectrum from 0 Hz to 3000 Hz. Absolute dissipation rates were normalized to the applied apparent force and plotted separately with and without the stimulus frequency (Figure 46, left panel). When the stimulus intensity was increased, the dissipation rate declined at frequencies other than the stimulus frequency, while the dissipation rate at the stimulus frequency increased. The total dissipation rate remained unchanged. When the apparent force of the stimulus exceeded 10^{-12} N, the dissipation rate at the stimulus frequency dominated in the overall dissipation rate (Figure 46, right panel), suggesting all the dissipated energy due to the active process was fed into the frequency of stimulation.

Assessment of active process by calculation of energy flux

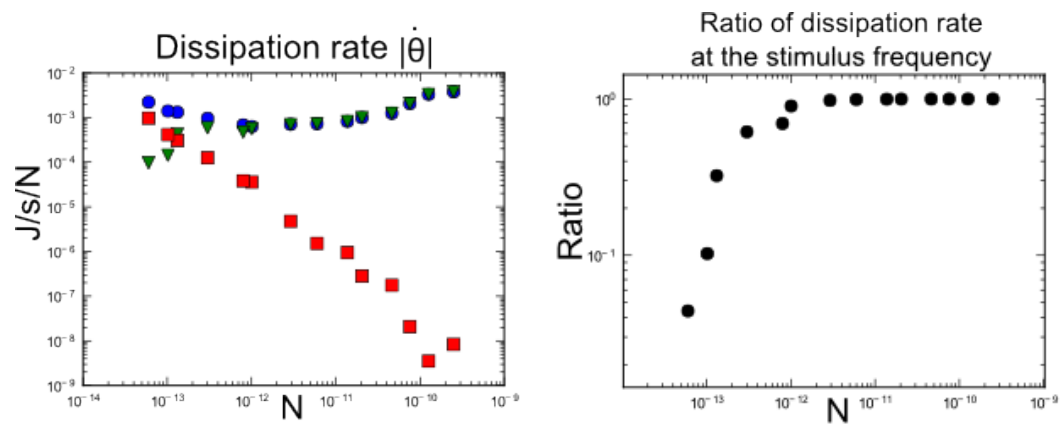


Figure 46: Dissipation rate and ratio of the dissipation rate at the stimulus frequency

Left panel: The absolute value of normalized dissipation rates were plotted against the apparent force exerted by the pure tone. The dissipation rates were normalized to the apparent force. The dissipation rate at the stimulus frequency is marked by green triangles; the dissipation rate at frequency other than the stimulus frequency by red squares and the total dissipation rate by blue circles.

Right panel: The ratio between the dissipation rate at the stimulus frequency and the total dissipation rate was plotted against the apparent force of the pure tone. Experimental data provided by Dr. Thomas Effertz.

4. Discussion

4.1. The framework “Virtual Fly Ear”

The models and simulations of the “Virtual Fly Ear” provide a useful tool to systematically analyze auditory functions in large numbers of flies. Using the models, the macroscopic measurements can be linked to parameters on molecular level. By using optimization algorithm, parameters are optimized to fit the experimental data, providing a list of parameters that reflect biophysical properties of the sound receiver and the transduction apparatus: the apparent mass of sound receiver (m), the open probability of transduction channels ($P_{o,s}$), the stiffness of the antennal joint (K_{AJ} of two-state model, K_1, K_2 and K_3 of two-state model with nonlinear parallel stiffness), the combined stiffness of the gating springs (K_{GS}), the friction constant of the antennal joint (λ), the combined friction constant of the adaptation motors (λ_a), the number of transducer modules (N) in each transducer population, (8) the projected gating swing of the transduction channels (D), the maximal projected force that the adaptation motors can generate (F_{max}), and the stiffness of the joint suspension (K_y of models with floating joint). Parameter values obtained by the fit seem reasonable, for instance, fitting the experimental data from a wild-type (Canton-S) fly with the two-state model predicts the mass of the sound receiver to be several nanograms, which is consistent with earlier reports [28, 44], and the number of transduction channel is several thousand (e.g. $N=11885$). Assuming that JO of *Drosophila* houses approximately 500 sensory neurons [22], this translates into 47 transduction channels per neuron.

The simulation program of the “Virtual Fly Ear” can reproduce the temporal evolution of mechanotransduction events. By integrating the differential equations numerically, the time traces of displacement response to stimulations, the power spectral densities of free fluctuation and the linear response function are reproduced. Furthermore, the motions of adaptation motors and the change of transduction channels are predicted. An associated program visualizes the temporal process, providing a more intuitive understanding of the dynamics, in

The framework “Virtual Fly Ear”

which the movements of the parallel spring, the gating spring and transduction channels are symbolized and scaled (see screenshot in Figure 28).

Following the anatomy of the fly’s auditory organ and mutant phenotypes, five models are implemented. Among these models, 4 models implement transducer modules displaying the compressive nonlinear behavior due to the gating compliance, 1 model implements the nonlinearity of stationary states, 1 model simultaneously implements 2 types of transduction channels with independent gating and adaptation properties and 1 model excludes any transducer module and, thus, is linearized. The best model without overfitting can be selected by AIC analysis. For a mutant fly, fitting experimental measurements with different models and subsequently comparing the models via AIC can help to narrow down the nature of the mutant defect. In this thesis, experimental data of *tilB* and *nompA* mutants has been explored. The AIC analysis revealed that the model without any transducer modules and their associated adaptation motors (model SHO with floating joint) is the best model, which is consistent with their linear antennal mechanics due to aberration of the sensory cilia of the auditory neurons in JO (*tilB* mutation, [47]) or the disconnection of the mechanosensory neurons and the antennal receiver (*nompA* mutation, [46]).

Programs have been developed to pre-process the experimental data, and extract relevant data automatically (see section 2.4). These programs facilitate the cleaning of large experimental datasets by automatic drift correction, outlier detection, and average calculation of time traces. These programs are also designed to be used as standalone applications. The post-processing programs of the “Virtual Fly Ear” (see section 3.1.2) extract and calculate relevant values (see Table 5) from the pre-processed experimental data and prepare the data for the fit. Assisted by the pre- and post-processing programs, the graphical user interfaces, the database and the parallel computation algorithm, the “Virtual Fly Ear” can be used as a high throughput application that allows analyzing mutant defect in auditory organ functions systematically.

4.2. Two-state model

The two-state model combines the gating-spring model, which describes mechanotransduction in hair cells [69-71], with the anatomy of the hearing organ of *Drosophila* [44]. Experimental measurements were shown that this model explains the active performance of fly's ear and quantitatively captures the displacement response, free fluctuation and nonlinearity of the fly's antennal sound receiver within the limit of small stimulus forces [44].

My analysis confirmed that, for small step forces ($F_{\text{external}} = 0$ to 10 pN), simulations with the 2-state model accurately reproduce the mechanics of the fly's sound receiver. Yet, the two-state model has its limitations: (1) General fits (including fit to displacement response to all step stimuli, free fluctuation and linear response function) only partially described the experimental data, especially when force amplitudes were high (Figure 32). When stimulated by larger stimuli, the stationary displacement at steady-state was slightly nonlinear (Figure 40). (2) The displacement response of the receivers of wild-type flies, *tilB* mutants and *nompA* mutants also displaced a slow creep that could not be described. (3) Applying the model to mutant flies with linearized auditory mechanics can cause overfitting or mislead the optimization process. As shown in Figure 33, the fit parameters of mutants revealed much smaller numbers of the transducer modules in each population ($N_{nompA1}=88$, $N_{cs1}=11885$), the projected gating swing on the tip of arista ($D_{nompA1}=65$ nm, $D_{cs1}=5331$ nm), and the coupling coefficient of the adaptation motors ($S_{tilB1}=1.68e-24$, $S_{cs1}=0.07$), indicating the absence of the transducer modules. Accordingly, a simplified model without transducer models was developed to fit their auditory mechanics.

Simulations also could not accurately reproduce the mechanics of *nompC*³ mutants. JO of *Drosophila* houses sound and gravity/wind receptors, about half of ~500 JO receptors preferentially respond to sound whereas the other half respond to static antennal deflection and mediate the detection of wind or gravity [67, 68, 102], and NompC is crucial for sound detection [62]. Accordingly, I developed a four-state model with 2 channel types, which can describe the wild-type fly better. Therefore, to obtain a better fit to experimental data of *nompC* mutants, the initial

Simple harmonic oscillator with floating joint versus 2-state model

parameters must be refined to match the properties of the machinery that detects static deflection.

4.3. Simple harmonic oscillator with floating joint versus 2-state model

To obtain a better description of the creep of displacement response to large stimuli, which is presumably caused by the movements of the pedicel, a floating joint was introduced into the model. Fits to experimental measurements of *tilB* and *nompA* mutants suggested the absence of transducer modules (see section 4.2). To prevent overfitting, all equations describing the transducer modules were removed.

AIC analysis revealed that, of the tested models, the simple harmonic oscillator with floating joint describes the mechanics of *nompA* receiver best and also describes the initial peak stiffness of the *tilB* receiver with ~100% probability and their steady-state stiffness with 24% probability. Although the two-state model is with 76% of probability the best model for *tilB* mutant, models having their AICc within 1–2 of the minimum have substantial support and should be taken into consideration [98].

4.4. Two-state model with floating joint or with nonlinear parallel stiffness versus 2-state model

To better describe the creep of the displacement response to step forces in wild-type flies, the two-state model was supplemented with a floating joint. Notwithstanding the reduced cost-function values, AIC analysis suggested that the two-state model is the best model without overfitting. This is because the AIC analysis in this thesis focused on the stiffness of the initial peak and steady-state. The temporal evolution of the time traces was not taken into account. An AIC analysis focusing on the time traces might yield different results.

The two-state model with a nonlinear parallel stiffness produced a better fit for wild-type fly than the one with linear parallel stiffness (Figure 40). Quantitatively, adding a nonlinear parallel stiffness to the model reduced the cost-function value by a factor of 1.2. However, the AIC is very sensitive with respect to the number

of free parameters indicating that the two-state model, which has 2 parameters less than the model with nonlinear parallel stiffness, is the best model.

4.5. Four-state model versus 2-state model

To fit the experimental data of wild-type fly with a four-state model, the fit parameters obtained from the fit to *nompC*³ mutants was taken as the initial parameters for the 2nd channel type. Because the fit to *nompC*³ mutant was already quite poor, possibly due to the initial parameter problem, fit with the four-state model to experimental data of wild-type flies did not yield satisfying result. Because the four-state model contains 5 more parameters than the two-state model, AIC indicated that this model is too complicated.

To improve the fit result, a better parameter set for the initial guess of 2nd channel type must be found.

4.6. Active process by energy flux

Apart from devising the “Virtual Fly Ear”, I devised a method to quantify the active energy flux in the fly’s ear. Hearing of *Drosophila* as for the other insects and vertebrates relies on active process to achieve the sensitivity and frequency selectivity [27, 99-101], which contributes to the fluctuation of the sound receiver and the sound-induced vibration. By comparing the power spectra of anesthetized and unanesthetized receivers, the active component was isolated from the fluctuation. The result of this calculation revealed that only a few motors are sufficient to generate the energy needed for the active process, which is consistent with previous results [28].

When actuated by an external force, the total energy flux due to the active process does not increase. The energy is redistributed into the frequency of the stimulus. This is consistent with the previous observation that the degree of phase-locking of the receiver’s vibration increases when the amplitude of stimulus increases [44].

Outlook

4.7. Outlook

A web-based version of the “Virtual Fly Ear” described in this thesis is currently being devised.

5. Abbreviations

AIC	Akaike's Information Criterion
AICc	corrected AIC
a1	1st antennal segment; scape
a2	2nd antennal segment; pedicel
a3	3rd antennal segment; funicle
CAP	compound action potential
CPU	Central Processing Unit
DWT	Discrete Wavelet Transform
FFT	Fast Fourier Transform (definition see Appendix A)
GUI	Graphical User Interface
<i>Iav</i>	<i>Inactive</i>
iBF	individual best frequency
iFFT	inverse Fast Fourier Transform
JO	Johnston's Organ
LDV	Laser Doppler Vibrometer
LRF	Linear Response Function
<i>Nan</i>	<i>Nanchung</i>
<i>NompA</i>	<i>no-mechanoreceptor-potential A</i>
<i>NompC</i>	<i>no-mechanoreceptor-potential C</i>
PSD	Power spectral density
SHO	simple harmonic oscillator
STD	Standard Deviation
TRP	Transient receptor potential
UFF	Universal File Format

6. Literature

- [1] R. D. Narda. Analysis of the stimuli involved in courtship and mating in *D. malerkotliana* (sophophora, drosophila). *Anim Behav*, 14 (2): 378–383, 1966.
- [2] H. H. Shorey. Nature of the sound produced by *Drosophila melanogaster* during courtship. *Science*, 137 (3531): 677–678, Aug 1962. doi: [10.1126/science.137.3531.677](https://doi.org/10.1126/science.137.3531.677). URL <http://dx.doi.org/10.1126/science.137.3531.677>.
- [3] Herman T. Spieth. *Mating behavior within the genus drosophila (diptera)*. Bulletin of american museum of natural history, 1952.
- [4] M. B. Sokolowski. *Drosophila*: genetics meets behaviour. *Nat Rev Genet*, 2 (11): 879–890, Nov 2001. doi: [10.1038/35098592](https://doi.org/10.1038/35098592). URL <http://dx.doi.org/10.1038/35098592>.
- [5] I. WALDRON. Courtship sound production in two sympatric sibling *Drosophila* species. *Science*, 144: 191–193, Apr 1964.
- [6] R. R. Hoy, A. Hoikkala, and K. Kaneshiro. Hawaiian courtship songs: evolutionary innovation in communication signals of *Drosophila*. *Science*, 240 (4849): 217–219, Apr 1988.
- [7] J. C. Hall. The mating of a fly. *Science*, 264 (5166): 1702–1714, Jun 1994.
- [8] D. F. Eberl, G. M. Duyk, and N. Perrimon. A genetic screen for mutations that disrupt an auditory response in *Drosophila melanogaster*. *Proc Natl Acad Sci U S A*, 94 (26): 14837–14842, Dec 1997.
- [9] ARTHUR W. EWING and H. C. BENNET-CLARK. The courtship songs of *Drosophila*. *Behaviour*, 31: 288–301, 1968.
- [10] Florian von Schilcher. The function of pulse song and sine song in the courtship of *Drosophila melanogaster*. *Animal Behaviour*, 24: 622–625, 1976. URL <http://www.sciencedirect.com/science/article/pii/S0003347276800760>.

- [11] Alt, Ringo, Talyn, Bray, and Dowse. The period gene controls courtship song cycles in *drosophila melanogaster*. *Anim Behav*, 56 (1): 87–97, Jul 1998. doi: [10.1006/anbe.1998.0743](https://doi.org/10.1006/anbe.1998.0743). URL <http://dx.doi.org/10.1006/anbe.1998.0743>.
- [12] Jennifer M Gleason. Mutations and natural genetic variation in the courtship song of *drosophila*. *Behav Genet*, 35 (3): 265–277, May 2005. doi: [10.1007/s10519-005-3219-y](https://doi.org/10.1007/s10519-005-3219-y). URL <http://dx.doi.org/10.1007/s10519-005-3219-y>.
- [13] Arthur W. Ewing and Jaleel A. Miyan. Sexual selection, sexual isolation and the evolution of song in the *drosophila repleta* group of species. *Animal Behaviour*, 34: 421–429, 1986. URL <http://www.sciencedirect.com/science/article/pii/S0003347286801129>.
- [14] Olena Riabinina, Mingjie Dai, Thomas Duke, and Jörg T Albert. Active process mediates species-specific tuning of *drosophila* ears. *Curr Biol*, 21 (8): 658–664, Apr 2011. doi: [10.1016/j.cub.2011.03.001](https://doi.org/10.1016/j.cub.2011.03.001). URL <http://dx.doi.org/10.1016/j.cub.2011.03.001>.
- [15] P. D Si Dong, Jennifer Scholz Dicks, and Grace Panganiban. *Distal-less* and *homothorax* regulate multiple targets to pattern the *drosophila* antenna. *Development*, 129 (8): 1967–1974, Apr 2002.
- [16] M. C. Göpfert and D. Robert. Biomechanics. turning the key on *drosophila* audition. *Nature*, 411 (6840): 908, Jun 2001. doi: [10.1038/35082144](https://doi.org/10.1038/35082144). URL <http://dx.doi.org/10.1038/35082144>.
- [17] Martin C Göpfert and Daniel Robert. The mechanical basis of *drosophila* audition. *J Exp Biol*, 205 (Pt 9): 1199–1208, May 2002.
- [18] Sokol V Todi, Yashoda Sharma, and Daniel F Eberl. Anatomical and molecular design of the *drosophila* antenna as a flagellar auditory organ. *Microsc Res Tech*, 63 (6): 388–399, Apr 2004. doi: [10.1002/jemt.20053](https://doi.org/10.1002/jemt.20053). URL <http://dx.doi.org/10.1002/jemt.20053>.

- [19] Jason C Caldwell and Daniel F Eberl. Towards a molecular understanding of drosophila hearing. *J Neurobiol*, 53 (2): 172–189, Nov 2002. doi: [10.1002/neu.10126](https://doi.org/10.1002/neu.10126). URL <http://dx.doi.org/10.1002/neu.10126>.
- [20] Andrew P Jarman. Studies of mechanosensation using the fly. *Hum Mol Genet*, 11 (10): 1215–1218, May 2002.
- [21] L.H. Field & T. Matheson. Chordotonal organs of insects. *Advances in Insect Physiology*, 17, 1998.
- [22] Azusa Kamikouchi, Takashi Shimada, and Kei Ito. Comprehensive classification of the auditory sensory projections in the brain of the fruit fly drosophila melanogaster. *J Comp Neurol*, 499 (3): 317–356, Nov 2006. doi: [10.1002/cne.21075](https://doi.org/10.1002/cne.21075). URL <http://dx.doi.org/10.1002/cne.21075>.
- [23] Jörg T Albert, Björn Nadrowski, and Martin C Göpfert. Mechanical signatures of transducer gating in the drosophila ear. *Curr Biol*, 17 (11): 1000–1006, Jun 2007. doi: [10.1016/j.cub.2007.05.004](https://doi.org/10.1016/j.cub.2007.05.004). URL <http://dx.doi.org/10.1016/j.cub.2007.05.004>.
- [24] Jörg T Albert, Björn Nadrowski, and Martin C Göpfert. Drosophila mechanotransduction–linking proteins and functions. *Fly (Austin)*, 1 (4): 238–241, 2007.
- [25] Björn Nadrowski and Martin C Göpfert. Modeling auditory transducer dynamics. *Curr Opin Otolaryngol Head Neck Surg*, 17 (5): 400–406, Oct 2009. doi: [10.1097/MOO.0b013e3283303443](https://doi.org/10.1097/MOO.0b013e3283303443). URL <http://dx.doi.org/10.1097/MOO.0b013e3283303443>.
- [26] Azusa Kamikouchi & Martin C. Gopfert Jörg T. Albert, Björn Nadrowski. Mechanical tracing of protein function in the drosophila ear. *nature protocols*, 2006. doi: [doi:10.1038/nprot.2006.364](https://doi.org/10.1038/nprot.2006.364). URL <http://www.nature.com/protocolexchange/protocols/58>.
- [27] M. C. Göpfert and D. Robert. Motion generation by drosophila mechanosensory neurons. *Proc Natl Acad Sci U S A*, 100 (9): 5514–5519, Apr

2003. doi: [10.1073/pnas.0737564100](https://doi.org/10.1073/pnas.0737564100). URL <http://dx.doi.org/10.1073/pnas.0737564100>.
- [28] M. C. Göpfert, A. D L Humphris, J. T. Albert, D. Robert, and O. Hendrich. Power gain exhibited by motile mechanosensory neurons in drosophila ears. *Proc Natl Acad Sci U S A*, 102 (2): 325–330, Jan 2005. doi: [10.1073/pnas.0405741102](https://doi.org/10.1073/pnas.0405741102). URL <http://dx.doi.org/10.1073/pnas.0405741102>.
- [29] Martin C Göpfert, Jörg T Albert, B. Nadrowski, and A. Kamikouchi. Specification of auditory sensitivity by drosophila trp channels. *Nat Neurosci*, 9 (8): 999–1000, Aug 2006. doi: [10.1038/nn1735](https://doi.org/10.1038/nn1735). URL <http://dx.doi.org/10.1038/nn1735>.
- [30] J. Ashmore, P. Avan, W. E. Brownell, P. Dallos, K. Dierkes, R. Fettiplace, K. Grosh, C. M. Hackney, A. J. Hudspeth, F. Jülicher, B. Lindner, P. Martin, J. Meaud, C. Petit, J. R Santos Sacchi, and B. Canlon. The remarkable cochlear amplifier. *Hear Res*, 266 (1-2): 1–17, Jul 2010. doi: [10.1016/j.heares.2010.05.001](https://doi.org/10.1016/j.heares.2010.05.001). URL <http://dx.doi.org/10.1016/j.heares.2010.05.001>.
- [31] T. Gold and R. J. Pumphrey. Hearing. i. the cochlea as a frequency analyzer. *Proceedings of the Royal Society of London*, 135: 462–491, 1948.
- [32] Azusa Kamikouchi, Jörg T Albert, and Martin C Göpfert. Mechanical feedback amplification in drosophila hearing is independent of synaptic transmission. *Eur J Neurosci*, 31 (4): 697–703, Feb 2010. doi: [10.1111/j.1460-9568.2010.07099.x](https://doi.org/10.1111/j.1460-9568.2010.07099.x). URL <http://dx.doi.org/10.1111/j.1460-9568.2010.07099.x>.
- [33] Björn Nadrowski, Thomas Effertz, Pingkalai R Senthilan, and Martin C Göpfert. Antennal hearing in insects—new findings, new questions. *Hear Res*, 273 (1-2): 7–13, Mar 2011. doi: [10.1016/j.heares.2010.03.092](https://doi.org/10.1016/j.heares.2010.03.092). URL <http://dx.doi.org/10.1016/j.heares.2010.03.092>.
- [34] R. Stoop, A. Kern, M. C. Göpfert, D. A. Smirnov, T. V. Dikanev, and B. P. Bezrucko. A generalization of the van-der-pol oscillator underlies active signal amplification in drosophila hearing. *Eur Biophys J*, 35 (6): 511–516, Aug

2006. doi: [10.1007/s00249-006-0059-5](https://doi.org/10.1007/s00249-006-0059-5). URL <http://dx.doi.org/10.1007/s00249-006-0059-5>.

[35] Björn Nadrowski and Martin C Göpfert. Level-dependent auditory tuning: Transducer-based active processes in hearing and best-frequency shifts. *Commun Integr Biol*, 2 (1): 7–10, 2009.

[36] Qianhao Lu, Pingkalai R Senthilan, Thomas Effertz, Björn Nadrowski, and Martin C Göpfert. Using drosophila for studying fundamental processes in hearing. *Integr Comp Biol*, 49 (6): 674–680, Dec 2009. doi: [10.1093/icb/icp072](https://doi.org/10.1093/icb/icp072). URL <http://dx.doi.org/10.1093/icb/icp072>.

[37] H. Davis. An active process in cochlear mechanics. *Hear Res*, 9 (1): 79–90, Jan 1983.

[38] L. Robles and M. A. Ruggero. Mechanics of the mammalian cochlea. *Physiol Rev*, 81 (3): 1305–1352, Jul 2001.

[39] Jonathan Ashmore and Jonathan Gale. The cochlear amplifier. *Curr Biol*, 14 (11): R403–R404, Jun 2004. doi: [10.1016/j.cub.2004.05.025](https://doi.org/10.1016/j.cub.2004.05.025). URL <http://dx.doi.org/10.1016/j.cub.2004.05.025>.

[40] Peter Dallos. Cochlear amplification, outer hair cells and prestin. *Curr Opin Neurobiol*, 18 (4): 370–376, Aug 2008. doi: [10.1016/j.conb.2008.08.016](https://doi.org/10.1016/j.conb.2008.08.016). URL <http://dx.doi.org/10.1016/j.conb.2008.08.016>.

[41] A. J. Hudspeth. Making an effort to listen: mechanical amplification in the ear. *Neuron*, 59 (4): 530–545, Aug 2008. doi: [10.1016/j.neuron.2008.07.012](https://doi.org/10.1016/j.neuron.2008.07.012). URL <http://dx.doi.org/10.1016/j.neuron.2008.07.012>.

[42] P. Martin and A. J. Hudspeth. Compressive nonlinearity in the hair bundle’s active response to mechanical stimulation. *Proc Natl Acad Sci U S A*, 98 (25): 14386–14391, Dec 2001. doi: [10.1073/pnas.251530498](https://doi.org/10.1073/pnas.251530498). URL <http://dx.doi.org/10.1073/pnas.251530498>.

[43] Björn Nadrowski, Pascal Martin, and Frank Jülicher. Active hair-bundle motility harnesses noise to operate near an optimum of mechanosensitivity. *Proc*

Natl Acad Sci U S A, 101 (33): 12195–12200, Aug 2004. doi: [10.1073/pnas.0403020101](https://doi.org/10.1073/pnas.0403020101). URL <http://dx.doi.org/10.1073/pnas.0403020101>.

[44] Björn Nadrowski, Jörg T Albert, and Martin C Göpfert. Transducer-based force generation explains active process in drosophila hearing. *Curr Biol*, 18 (18): 1365–1372, Sep 2008. doi: [10.1016/j.cub.2008.07.095](https://doi.org/10.1016/j.cub.2008.07.095). URL <http://dx.doi.org/10.1016/j.cub.2008.07.095>.

[45] M. Kernan, D. Cowan, and C. Zuker. Genetic dissection of mechanosensory transduction: mechanoreception-defective mutations of drosophila. *Neuron*, 12 (6): 1195–1206, Jun 1994.

[46] Y. D. Chung, J. Zhu, Y. Han, and M. J. Kernan. *nompA* encodes a pns-specific, zp domain protein required to connect mechanosensory dendrites to sensory structures. *Neuron*, 29 (2): 415–428, Feb 2001.

[47] D. F. Eberl, R. W. Hardy, and M. J. Kernan. Genetically similar transduction mechanisms for touch and hearing in drosophila. *J Neurosci*, 20 (16): 5981–5988, Aug 2000.

[48] Eugene Lee, Elena Sivan-Loukianova, Daniel F Eberl, and Maurice J Kernan. An *ift-a* protein is required to delimit functionally distinct zones in mechanosensory cilia. *Curr Biol*, 18 (24): 1899–1906, Dec 2008. doi: [10.1016/j.cub.2008.11.020](https://doi.org/10.1016/j.cub.2008.11.020). URL <http://dx.doi.org/10.1016/j.cub.2008.11.020>.

[49] Meredith LeMasurier and Peter G Gillespie. Hair-cell mechanotransduction and cochlear amplification. *Neuron*, 48 (3): 403–415, Nov 2005. doi: [10.1016/j.neuron.2005.10.017](https://doi.org/10.1016/j.neuron.2005.10.017). URL <http://dx.doi.org/10.1016/j.neuron.2005.10.017>.

[50] Thomas Weber, Martin C Gopfert, Harald Winter, Ulrike Zimmermann, Hanni Kohler, Alexandra Meier, Oliver Hendrich, Karin Rohbock, Daniel Robert, and Marlies Knipper. Expression of prestin-homologous solute carrier (*slc26*) in auditory organs of nonmammalian vertebrates and insects. *Proc Natl Acad Sci U S A*, 100 (13): 7690–7695, Jun 2003. doi: [10.1073/pnas.1330557100](https://doi.org/10.1073/pnas.1330557100). URL <http://dx.doi.org/10.1073/pnas.1330557100>.

- [51] R. G. Walker, A. T. Willingham, and C. S. Zuker. A drosophila mechanosensory transduction channel. *Science*, 287 (5461): 2229–2234, Mar 2000.
- [52] Janghwan Kim, Yun Doo Chung, Dae-Young Park, SooKyung Choi, Dong Wook Shin, Heun Soh, Hye Won Lee, Wonseok Son, Jeongbin Yim, Chul-Seung Park, Maurice J Kernan, and Changsoo Kim. A trpv family ion channel required for hearing in drosophila. *Nature*, 424 (6944): 81–84, Jul 2003. doi: [10.1038/nature01733](https://doi.org/10.1038/nature01733). URL <http://dx.doi.org/10.1038/nature01733>.
- [53] Zhefeng Gong, Wonseok Son, Yun Doo Chung, Janghwan Kim, Dong Wook Shin, Colleen A McClung, Yong Lee, Hye Won Lee, Deok-Jin Chang, Bong-Kiun Kaang, Hawon Cho, Uhtaek Oh, Jay Hirsh, Maurice J Kernan, and Changsoo Kim. Two interdependent trpv channel subunits, inactive and nanchung, mediate hearing in drosophila. *J Neurosci*, 24 (41): 9059–9066, Oct 2004. doi: [10.1523/JNEUROSCI.1645-04.2004](https://doi.org/10.1523/JNEUROSCI.1645-04.2004). URL <http://dx.doi.org/10.1523/JNEUROSCI.1645-04.2004>.
- [54] C. S. Walker, R. P. Shetty, K. Clark, S. G. Kazuko, A. Letsou, B. M. Olivera, and P. K. Bandyopadhyay. On a potential global role for vitamin k-dependent gamma-carboxylation in animal systems. evidence for a gamma-glutamyl carboxylase in drosophila. *J Biol Chem*, 276 (11): 7769–7774, Mar 2001. doi: [10.1074/jbc.M009576200](https://doi.org/10.1074/jbc.M009576200). URL <http://dx.doi.org/10.1074/jbc.M009576200>.
- [55] Jonathon Howard and Susanne Bechstedt. Hypothesis: a helix of ankyrin repeats of the nompc-trp ion channel is the gating spring of mechanoreceptors. *Curr Biol*, 14 (6): R224–R226, Mar 2004. doi: [10.1016/j.cub.2004.02.050](https://doi.org/10.1016/j.cub.2004.02.050). URL <http://dx.doi.org/10.1016/j.cub.2004.02.050>.
- [56] Marcos Sotomayor, David P Corey, and Klaus Schulten. In search of the hair-cell gating spring elastic properties of ankyrin and cadherin repeats. *Structure*, 13 (4): 669–682, Apr 2005. doi: [10.1016/j.str.2005.03.001](https://doi.org/10.1016/j.str.2005.03.001). URL <http://dx.doi.org/10.1016/j.str.2005.03.001>.

- [57] Gwangrog Lee, Khadar Abdi, Yong Jiang, Peter Michaely, Vann Bennett, and Piotr E Marszalek. Nanospring behaviour of ankyrin repeats. *Nature*, 440 (7081): 246–249, Mar 2006. doi: [10.1038/nature04437](https://doi.org/10.1038/nature04437). URL <http://dx.doi.org/10.1038/nature04437>.
- [58] David P Corey. What is the hair cell transduction channel? *J Physiol*, 576 (Pt 1): 23–28, Oct 2006. doi: [10.1113/jphysiol.2006.116582](https://doi.org/10.1113/jphysiol.2006.116582). URL <http://dx.doi.org/10.1113/jphysiol.2006.116582>.
- [59] Wei Li, Zhaoyang Feng, Paul W Sternberg, and X. Z Shawn Xu. A *c. elegans* stretch receptor neuron revealed by a mechanosensitive trp channel homologue. *Nature*, 440 (7084): 684–687, Mar 2006. doi: [10.1038/nature04538](https://doi.org/10.1038/nature04538). URL <http://dx.doi.org/10.1038/nature04538>.
- [60] Li E Cheng, Wei Song, Loren L Looger, Lily Yeh Jan, and Yuh Nung Jan. The role of the trp channel *nompC* in *drosophila* larval and adult locomotion. *Neuron*, 67 (3): 373–380, Aug 2010. doi: [10.1016/j.neuron.2010.07.004](https://doi.org/10.1016/j.neuron.2010.07.004). URL <http://dx.doi.org/10.1016/j.neuron.2010.07.004>.
- [61] Lijun Kang, Jingwei Gao, William R Schafer, Zhixiong Xie, and X. Z Shawn Xu. *C. elegans* trp family protein trp-4 is a pore-forming subunit of a native mechanotransduction channel. *Neuron*, 67 (3): 381–391, Aug 2010. doi: [10.1016/j.neuron.2010.06.032](https://doi.org/10.1016/j.neuron.2010.06.032). URL <http://dx.doi.org/10.1016/j.neuron.2010.06.032>.
- [62] Thomas Effertz, Robert Wiek, and Martin C Göpfert. *NompC* trp channel is essential for *drosophila* sound receptor function. *Curr Biol*, 21 (7): 592–597, Apr 2011. doi: [10.1016/j.cub.2011.02.048](https://doi.org/10.1016/j.cub.2011.02.048). URL <http://dx.doi.org/10.1016/j.cub.2011.02.048>.
- [63] Adam P Christensen and David P Corey. Trp channels in mechanosensation: direct or indirect activation? *Nat Rev Neurosci*, 8 (7): 510–521, Jul 2007. doi: [10.1038/nrn2149](https://doi.org/10.1038/nrn2149). URL <http://dx.doi.org/10.1038/nrn2149>.

- [64] Ellen A Lumpkin and Michael J Caterina. Mechanisms of sensory transduction in the skin. *Nature*, 445 (7130): 858–865, Feb 2007. doi: [10.1038/nature05662](https://doi.org/10.1038/nature05662). URL <http://dx.doi.org/10.1038/nature05662>.
- [65] Martin Chalfie. Neurosensory mechanotransduction. *Nat Rev Mol Cell Biol*, 10 (1): 44–52, Jan 2009. doi: [10.1038/nrm2595](https://doi.org/10.1038/nrm2595). URL <http://dx.doi.org/10.1038/nrm2595>.
- [66] Jóhanna Arnadóttir and Martin Chalfie. Eukaryotic mechanosensitive channels. *Annu Rev Biophys*, 39: 111–137, Jun 2010. doi: [10.1146/annurev.biophys.37.032807.125836](https://doi.org/10.1146/annurev.biophys.37.032807.125836). URL <http://dx.doi.org/10.1146/annurev.biophys.37.032807.125836>.
- [67] Azusa Kamikouchi, Hidehiko K Inagaki, Thomas Effertz, Oliver Hendrich, André Fiala, Martin C Göpfert, and Kei Ito. The neural basis of drosophila gravity-sensing and hearing. *Nature*, 458 (7235): 165–171, Mar 2009. doi: [10.1038/nature07810](https://doi.org/10.1038/nature07810). URL <http://dx.doi.org/10.1038/nature07810>.
- [68] Suzuko Yorozu, Allan Wong, Brian J Fischer, Heiko Dankert, Maurice J Kernan, Azusa Kamikouchi, Kei Ito, and David J Anderson. Distinct sensory representations of wind and near-field sound in the drosophila brain. *Nature*, 458 (7235): 201–205, Mar 2009. doi: [10.1038/nature07843](https://doi.org/10.1038/nature07843). URL <http://dx.doi.org/10.1038/nature07843>.
- [69] J. Howard and A. J. Hudspeth. Compliance of the hair bundle associated with gating of mechano-electrical transduction channels in the bullfrog's saccular hair cell. *Neuron*, 1 (3): 189–199, May 1988.
- [70] D. P. Corey and A. J. Hudspeth. Kinetics of the receptor current in bullfrog saccular hair cells. *J Neurosci*, 3 (5): 962–976, May 1983.
- [71] J. Howard and A. J. Hudspeth. Mechanical relaxation of the hair bundle mediates adaptation in mechano-electrical transduction by the bullfrog's saccular hair cell. *Proc Natl Acad Sci U S A*, 84 (9): 3064–3068, May 1987.

- [72] P. Martin, A. D. Mehta, and A. J. Hudspeth. Negative hair-bundle stiffness betrays a mechanism for mechanical amplification by the hair cell. *Proc Natl Acad Sci U S A*, 97 (22): 12026–12031, Oct 2000. doi: [10.1073/pnas.210389497](https://doi.org/10.1073/pnas.210389497). URL <http://dx.doi.org/10.1073/pnas.210389497>.
- [73] V. M. Eguíluz, M. Ospeck, Y. Choe, A. J. Hudspeth, and M. O. Magnasco. Essential nonlinearities in hearing. *Phys Rev Lett*, 84 (22): 5232–5235, May 2000.
- [74] A. J. Hudspeth, Y. Choe, A. D. Mehta, and P. Martin. Putting ion channels to work: mechano-electrical transduction, adaptation, and amplification by hair cells. *Proc Natl Acad Sci U S A*, 97 (22): 11765–11772, Oct 2000. doi: [10.1073/pnas.97.22.11765](https://doi.org/10.1073/pnas.97.22.11765). URL <http://dx.doi.org/10.1073/pnas.97.22.11765>.
- [75] Wiener-Khinchin Theorem. http://en.wikipedia.org/wiki/wiener%e2%80%93khinchin_theorem.
- [76] S. R. Shaw. Re-evaluation of the absolute threshold and response mode of the most sensitive known "vibration" detector, the cockroach's subgenual organ: a cochlea-like displacement threshold and a direct response to sound. *J Neurobiol*, 25 (9): 1167–1185, Sep 1994. doi: [10.1002/neu.480250911](https://doi.org/10.1002/neu.480250911). URL <http://dx.doi.org/10.1002/neu.480250911>.
- [77] J. A. Nelder and R. Mead. A simplex method for function minimization. *Computer Journal*, 4: 308–313, 1965. doi: [10.1093/comjnl/7.4.308](https://doi.org/10.1093/comjnl/7.4.308). URL <http://comjnl.oxfordjournals.org/content/7/4/308.abstract>.
- [78] Python. <http://www.python.org>. URL <http://www.python.org>.
- [79] UFF. <http://www.sdrl.uc.edu/universal-file-formats-for-modal-analysis-testing-1/universal-file-formats-for-modal-analysis-testing?searchterm=universal+file+format>. URL <http://www.sdrl.uc.edu/universal-file-formats-for-modal-analysis-testing-1/universal-file-formats-for-modal-analysis-testing?searchterm=universal+file+format>.
- [80] NIST/SEMATECH. e-handbook of statistical methods. 1.3.5.17, 2010. URL <http://www.itl.nist.gov/div898/handbook/>. Detection of outliers.

- [81] F. J. Harris. On the use of windows for harmonic analysis with the discrete fourier transform. 66 (1): 51–83, 1978. doi: [10.1109/PROC.1978.10837](https://doi.org/10.1109/PROC.1978.10837).
- [82] William Vetterling William H. Press, Saul Teukolsky and Brian Flannery. *Numerical Recipes 3rd Edition: The Art of Scientific Computing*. Cambridge University Press ISBN-13: 978-0521880688, 2007.
- [83] GNU Scientific Library. <http://www.gnu.org/software/gsl/>.
- [84] Qt4. <http://qt.nokia.com/>.
- [85] Qt widgets for technical applications. <http://qwt.sourceforge.net/>.
- [86] Scipy. <http://www.scipy.org/>.
- [87] PyQt. <http://www.riverbankcomputing.co.uk/software/pyqt/intro>.
- [88] Numeric. <http://people.csail.mit.edu/jrennie/python/numeric/>.
- [89] PyGSL. <http://sourceforge.net/projects/pygsl/>.
- [90] ScientificPython. <http://dirac.cnrs-orleans.fr/plone/software/scientificpython/>.
- [91] Matplotlib. <http://matplotlib.sourceforge.net/>.
- [92] SQLite. <http://www.sqlite.org/>.
- [93] Python-configobj. <http://pypi.python.org/pypi/configobj/>.
- [94] S. G. Mallat. A theory for multiresolution signal decomposition: the wavelet representation. 11 (7): 674–693, 1989. doi: [10.1109/34.192463](https://doi.org/10.1109/34.192463).
- [95] Preben Graberg Nes. *Edge-Detection in Signals using the Continuous Wavelet Transform*. PhD thesis, Norwegian University of Science and Technology, 2006.
- [96] William H. Press, Saul A. Teukolsky, William T. Vetterling, and Brian P. Flannery. *Numerical Recipes : The Art of Scientific Computing*. Cambridge University Press, third edition, 2007.

- [97] Thomas Effertz. *CANDIDATE MECHANOSENSITIVE TRANSDUCTION CHANNELS IN DROSOPHILA MELANOGASTER*. PhD thesis, Georg-August-University Göttingen, 2011.
- [98] K. P. Burnham and D. R. Anderson. *Model selection and multimodel inference : a practical information-theoretic approach*. Springer, New York, 2002.
- [99] P. Martin and A. J. Hudspeth. Active hair-bundle movements can amplify a hair cell's response to oscillatory mechanical stimuli. *Proc Natl Acad Sci U S A*, 96 (25): 14306–14311, Dec 1999.
- [100] P. Dallos. The active cochlea. *J Neurosci*, 12 (12): 4575–4585, Dec 1992.
- [101] R. Nobili, F. Mammano, and J. Ashmore. How well do we understand the cochlea? *Trends Neurosci*, 21 (4): 159–167, Apr 1998.
- [102] Yishan Sun, Lei Liu, Yehuda Ben-Shahar, Julie S Jacobs, Daniel F Eberl, and Michael J Welsh. Trpa channels distinguish gravity sensing from hearing in johnston's organ. *Proc Natl Acad Sci U S A*, 106 (32): 13606–13611, Aug 2009. doi: [10.1073/pnas.0906377106](https://doi.org/10.1073/pnas.0906377106). URL <http://dx.doi.org/10.1073/pnas.0906377106>.

Appendix A. Definition of continuous Fourier transform and discrete Fourier transform

The continuous Fourier transform used in this thesis is defined as

$$f(v) = \mathcal{F}\{f(t)\}(v)$$

$$f(v) = \int_{-\infty}^{\infty} f(t)e^{-2\pi i v t} dt.$$

Now consider generalization to the case of a discrete function, $f(t) \rightarrow f(t_k)$ by letting $f_k \equiv f(t_k)$, where $t_k \equiv k\Delta$, with $k = 0, \dots, N-1$. Writing this out gives the discrete Fourier transform $F_n = \mathcal{F}\{f_k\}_{k=0}^{N-1}(n)$ as

$$F_n = \frac{1}{N} \sum_{k=0}^{N-1} f_k e^{-2\pi i n k / N}.$$

And the inverse transform $f_k = \mathcal{F}\{F_n\}_{n=0}^{N-1}(k)$ is then

$$f_k = \sum_{n=0}^{N-1} F_n e^{2\pi i n k / N}.$$

The discrete Fourier transform at certain frequency v_n is computed as

$$\tilde{X}(v_n) = \int_{-\infty}^{\infty} X(t) e^{-2\pi i v_n t} dt = \sum_{k=0}^{\infty} X_k e^{-2\pi i v_n t_k \cdot \Delta t}.$$

Appendix B. Result of the energy flux analysis for fly 2 and fly 3

B.1. Fly 2 (Canton-S)

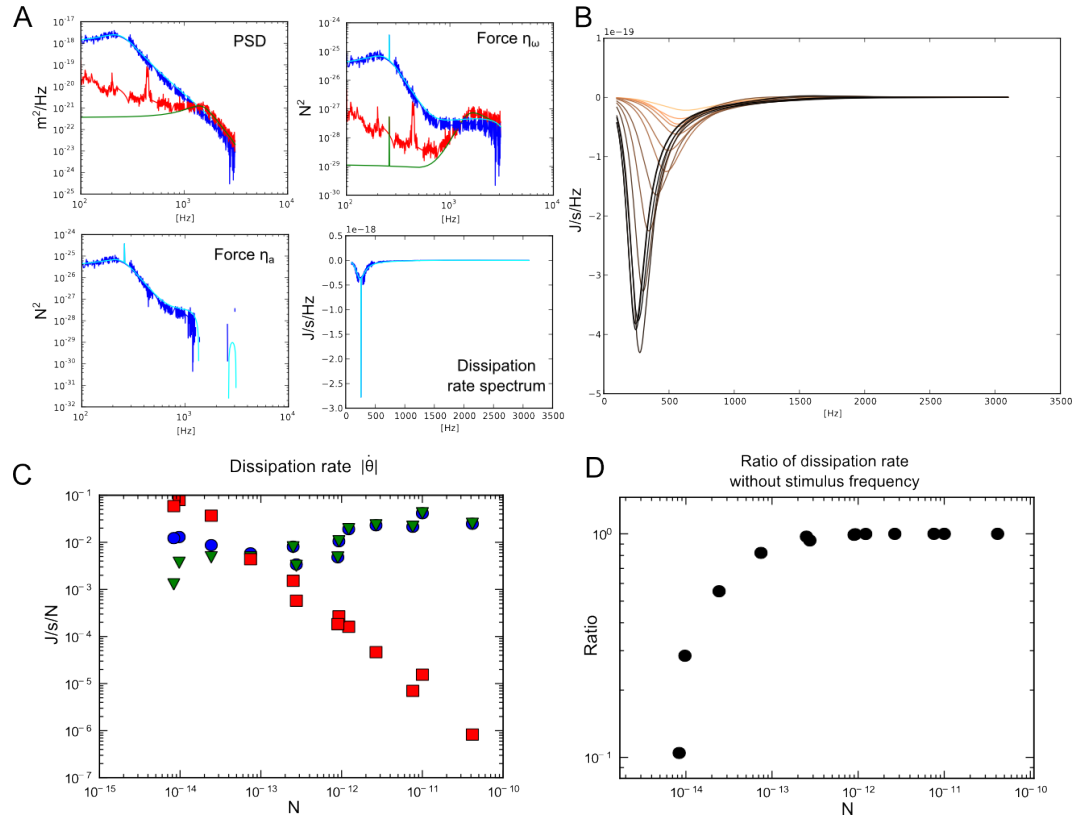


Figure 47: Assessing the auditory active process in fly 2

(A): The PSD of the sound-induced vibration was measured and fitted. Force η_ω and η_a and the dissipation rate spectrum was calculated and fitted (the measured data of the fly at anesthetized state were colored red and its fit data were colored green; the measured data of the fly at unanesthetized state were colored blue and its fit data in turquoise.) The apparent force of the pure tone stimulus was 13 fN

(B): The dissipation rate spectra of 14 stimulus intensities were plotted. The spectrum at the lowest stimulus intensity (apparent force = 8.3 fN) was colored black and the spectrum resulted from the highest stimulus intensity (apparent force=41 pN) was colored light orange. Spectra of the other stimuli were colored according to the color gradient.

(C): The absolute value of normalized dissipation rates were plotted against the apparent force exerted by the pure tone. The dissipation rates were normalized to the apparent force. The dissipation rate at the stimulus frequency is marked by green triangles; the dissipation rate at frequency other than the stimulus frequency by red squares and the total dissipation rate by blue circles.

(D): The ratio between the dissipation rate at the stimulus frequency and the total dissipation rate was plotted against the apparent force of the pure tone. Experimental data provided by Dr. Thomas Effertz.

B.2. Fly 2 (Canton-S)

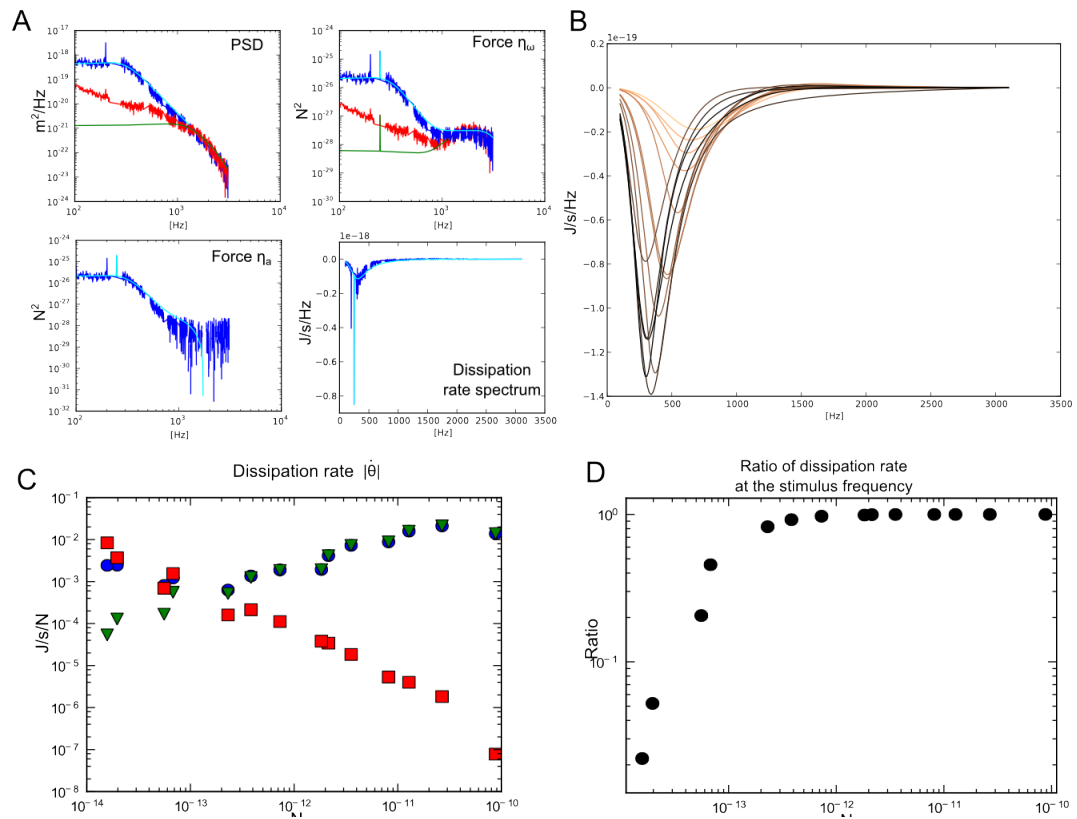


Figure 48: Assessing the auditory active process in fly 3

(A): The PSD of the sound-induced vibration was measured and fitted. Force η_ω and η_a and the dissipation rate spectrum was calculated and fitted (the measured data of the fly at anesthetized state were colored red and its fit data were colored green; the measured data of the fly at unanesthetized state were colored blue and its fit data in turquoise.) The apparent force of the pure tone stimulus was 15 fN

(B): The dissipation rate spectra of 14 stimulus intensities were plotted. The spectrum at the lowest stimulus intensity (apparent force = 15 fN) was colored black and the spectrum resulted from the highest stimulus intensity (apparent force=95 pN) was colored light orange. Spectra of the other stimuli were colored according to the color gradient.

(C): The absolute value of normalized dissipation rates were plotted against the apparent force exerted by the pure tone. The dissipation rates were normalized to the apparent force. The dissipation rate at the stimulus frequency is marked by green triangles; the dissipation rate at frequency other then the stimulus frequency by red squares and the total dissipation rate by blue circles.

(D): The ratio between the dissipation rate at the stimulus frequency and the total dissipation rate was plotted against the apparent force of the pure tone. Experimental data provided by Dr. Thomas Effertz.

Appendix C. Fit parameters used in this thesis

C.1. Two-state model

	$P_{o,s}$	S	K_{AJ} [pN/nm]	δ [nm]	λ [μg/s]	K_{GS} [pN/nm]	λ_a [μg/s]	m [ng]	N	D [nm]
CS small stimuli	0.5	6.57e-2	1.92e-2	4.78e2	4.92e-7	4.54e-2	1.29e-5	1.47	1.19e4	5.33e3
CS large stimuli	0.5	1.52e-1	2.32e-2	4.78e2	7.38e-7	2.19e-2	1.04e-5	1.80	6.85e3	3.53e3
TilB mutant	0.5	1.68e-24	2.11e-2	7.46e2	3.37e-6	1.31e-2	2.41e-5	1.76	5.53e3	1.36e3
NompA mutant	0.5	1.25e-1	3.21e-1	1.11e1	1.08e-4	6.60e-2	4.10e-4	78.66	8.80	6.56e1
NompC ³ mutant	0.5	3.67e-1	2.12e-2	4.65e2	1.42e-6	3.12e-2	1.20e-5	3.73	5.55e3	1.44e-7

C.2. Simple harmonic oscillator model with floating joint

	K_{AJ} [pN/nm]	λ [μg/s]	m [ng]	K_y [pN/nm]	τ_y [s]
CS large stimuli	2.87e-2	4.25e-6	2.44	4.39e-13	1.30e-1
TilB mutant	3.05e-2	7.83e-6	2.47	3.38e-1	9.38e-3
NompA mutant	1.76e-2	7.72e-6	4.35	3.44e-1	7.18e-3

C.3. Two-state model with floating joint

	$P_{o,s}$	S	K_{AJ} [pN/nm]	δ [nm]	λ [μg/s]	K_{GS} [pN/nm]	λ_a [μg/s]	m [ng]	N	D [nm]	K_y [pN/nm]	τ_y [s]
CS large stimuli	0.5	1.51e-1	2.38e-2	4.77e2	7.17e-7	2.18e-2	1.02e-5	1.77	6.77e3	1.85e3	3.10e-14	7.20e-2
TilB mutant	0.5	6.97e-2	1.32e-1	9.26e2	1.58e-5	4.87e-2	1.99e-5	3.21	54.15e3	2.20e-9	2.45e-1	1.57e-2
NompA mutant	0.5	1.23e-1	1.57e-2	2.24e2	4.59e-8	8.57e-2	9.31e-6	8.73	4.01e3	1.95e2	2.05e-1	9.25e-3

C.4. Two-state model with nonlinear parallel stiffness

	$P_{o,s}$	S	K_{AJ} [pN/nm]	δ [nm]	λ [μg/s]	K_{GS} [pN/nm]	λ_a [μg/s]	m [ng]	N	D [nm]	K_{AJ2} [pN/nm]	K_{AJ3} [pN/nm]
CS	0.5	2.11e-1	2.56e-2	3.60e2	8.54e-7	1.62e-2	1.02e-5	1.91	3.23e3	1.32e4	1.32e-7	6.52e-12

C.5. Four-state model

Fit parameters of wild-type fly (Canton-S) with four-state model:

$$K_{AJ} = 3.43e - 2 \text{ pN/nm}$$

$$\lambda = 4.58e - 7 \text{ } \mu\text{g/s}$$

$$m = 2.55 \text{ ng}$$

$$P_{o,s} = 0.5$$

$$D = 2.91e3 \text{ ng}$$

$$K_{GS} = 1.91e - 2 \text{ pN/nm}$$

$$\delta = 4.70e2 \text{ nm}$$

$$N = 6.86e3$$

$$\lambda_a 2.55e - 9 \text{ } \mu\text{g/s}$$

$$S = 1.12e - 5$$

$$P_{o,s2} = 0.5$$

$$D_2 = 2.38e - 1 \text{ ng}$$

$$K_{GS,2} = 2.25e - 2 \text{ pN/nm}$$

$$\delta_2 = 3.37e2 \text{ nm}$$

$$N_2 = 2.26e3$$

$$\lambda_{a,2} = 9.73e - 6 \text{ } \mu\text{g/s}$$

$$S_2 = 4.85e - 1$$

Appendix D. LDV Setup for sound stimulation

Air table: Linus Photonics series 63 table, Art-No. 436356401 (dimensions 900 × 1200 × 100 mm)

Laser Doppler Vibrometer (LDV): Polytec, PSV-400 equipped with an OFV-700 close-up unit (70 mm focal length)

A/D converter: Cambridge Electronic Devices, micro 1401 MKII

HiFi amplifier: dB Technologies MA 1060

Loudspeaker: Visaton W130S

Micro manipulators: 5 × MM33 with magnetic stand, Kanetec MB-K (animal holder; electrophysiology reference electrode; microphone; anterior and posterior electrostatic actuator electrodes) HS6, Märzhäuser (electrophysiology recording electrode)

Attenuator: Custom-build resistor based attenuator, attenuation range from 0-100 dB in 1 dB steps

Extracellular amplifier: 4-channel amplifier MA102

Humbug Quest Scientific

Microphone: Emkay NR 3158 miniature pressure-gradient microphone with an integrating amplifier, Knowles Electronics Inc., Itasca, Illinois, USA

Dissection microscope: Stereo microscope PZMIII-BS, World Precision Instruments

Lightsource: Fiberoptic clamp, Novaflex Bifurcated Light Guide Nova-186, World Precision Instruments

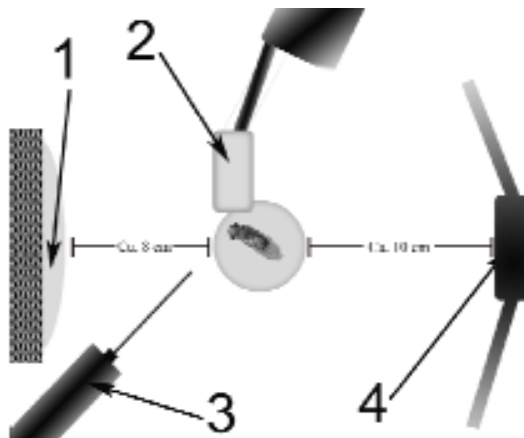


Figure 49 Experimental setup for sound intensity measurements

The LDV (1), measured the movement of the fly's antenna in response to sound stimuli emitted by a loudspeaker (4). A particle velocity sensitive microphone (2) measured the stimulus intensity at the position of the antenna. An etched insulated tungsten electrode (3) is inserted between the scape and head of the fly to record the compound action potential changes of the antennal nerve.

Appendix E. Table of Figures

Figure 1: Sequence of courtship of <i>Drosophila melanogaster</i>	6
Figure 2: Antennal hearing organ of <i>Drosophila</i>	7
Figure 3: Sketch of the chordotonal organ	8
Figure 4: Mechanical properties of sound receiver	10
Figure 5: Violation of the fluctuation-dissipation theorem demonstrates the active process	11
Figure 6: Model of TRP-channel function in <i>Drosophila</i> ear	13
Figure 7: Gating-spring model and activation of the MET-channel	15
Figure 8: Model of <i>Drosophila</i> hearing organ	16
Figure 9: Fixation of the fly	19
Figure 10 Fitting stimulated PSD	24
Figure 11 Illustration of force estimation for the sound induced stimulation	26
Figure 12 Setup for electrostatic measurements	27
Figure 13 Displacement response and its time trace of acceleration	30
Figure 14 Data cleaning	33
Figure 15 Averaged time trace	34
Figure 16: The workflow of the programs	40
Figure 17: Applying DWT edge detection on step stimuli	43
Figure 18: Fitting the step onset with sigmoidal function	44
Figure 19: Separated step stimuli and responses	46
Figure 20: The pre-processing of the PSD and the linear response function	48
Figure 21 database structure	49
Figure 22 GUI: Main window	50
Figure 23 GUI: Flies Management	50
Figure 24 GUI: Fit configuration	51
Figure 25 GUI: Parameters	51
Figure 26 GUI: Reference tables	53
Figure 27 GUI: Plots of the fit result	53
Figure 28 GUI: Visualization tool for the simulations	54
Figure 29: The cartoon of two-state model for <i>Drosophila</i> hearing organ	55
Figure 30: Mechanical responses of wild type fly fitted with 2-state model	58

Table of Figures

Figure 31: Deduced motor movement and channel open probabilities of wild type fly by 2-state model	59
Figure 32: Force-displacement characteristics of wild-type fly (Canton-S) with large stimuli fitted by 2-state model	60
Figure 33: Fit results of <i>tilB</i> and <i>nompA</i> mutants with 2-state model	62
Figure 34: Fit results of <i>nompC</i> mutants with 2-state model	63
Figure 35: Fit results of <i>tilB</i> and <i>nompA</i> mutants with harmonic oscillator with floating joint	65
Figure 36: Fit results of wild-type fly with harmonic oscillator with floating joint	66
Figure 37: The cartoon of two-state model with floating antennal joint	67
Figure 38: Fit results of wild-type fly, <i>tilB</i> mutant, and <i>nompA</i> mutant with two-state model with floating joint	68
Figure 39: Stimulus forces plotted against stationary displacement	69
Figure 40: Fit results of wild-type fly with two-state model with nonlinear parallel stiffness	70
Figure 41: The cartoon of four-state model for <i>Drosophila</i> hearing organ	71
Figure 42: Fit results of wild-type fly with four-state model	73
Figure 43: Mechanical fluctuation of the antennal sound receiver and corresponding PSD	83
Figure 44 dissipation rate spectrum during fluctuation of the sound receiver	88
Figure 45: Dissipation rate spectrum of the sound receiver during sound-induced vibration	91
Figure 46: Dissipation rate and ratio of the dissipation rate at the stimulus frequency	92
Figure 47: Assessing the auditory active process in fly 2	114
Figure 48: Assessing the auditory active process in fly 3	115
Figure 49 Experimental setup for sound intensity measurements	118

Table of Figures

Table 1 of mutants/wide types used during the thesis	19
Table 2 Summary of experimental data	35
Table 3 Libraries and description.....	36
Table 4 System requirements	37
Table 5: Result file produced by the post-processing modules.....	47
Table 6: Model selection for initial displacement peak of wild-type fly's sound receiver.....	79
Table 7: Model selection for stationary state of wild-type fly's sound receiver ...	79
Table 8: Model selection for initial displacement peak of <i>tilB</i> mutant's sound receiver.....	80
Table 9: Model selection for stationary state of <i>tilB</i> mutant's sound receiver.....	80
Table 10: Model selection for initial displacement peak of <i>nompA</i> mutant's sound receiver.....	81
Table 11: Model selection for stationary state of <i>nompA</i> mutant's sound receiver	81
Table 12: Fit parameters and the dissipation rates of measured flies	89

Acknowledgement

It is such a pleasure that I finally can say “thanks” to those people, who made this thesis possible. First, I want to thank my supervisor Martin Göpfert, for his endless support, for his patience, for his clever ideas which brought me forward.

I would like to thank my mentor Björn Nadrowski for introducing me into the modeling, contributing the program parts (page 35), and not only just for the scientific help, but also for interesting discussions. And I would like to thank the all-around man, Thomas Effertz, for providing experimental data and for being such a nice office-mate. When I needed help, he was always there.

Sometimes, the work just ran into a corner. At such situation, a second opinion is very important. Georg Raiser and David Piepenbrock were always the persons who could offer ideas helping me to find the clue. Thank you, Georg and David.

I actually want to thank everybody in the research group: Pingkalai Senthilan, Somdatta Karrak, Robert Wiek, Philipp Jähde, Gudrun Matthes, Stephanie Pauls, Guvanch Ovezmyradov All of them are good friends, nice co-workers. We shared scientific ideas, funny life experiences Because of them I had a good time. Without them, the thesis wouldn't have been possible.

I am grateful to my family, for the support by my parents, and especially for the encouragement by my wife.

Curriculum vitae

Personal Information

Name	Qianhao
Surname	Lu
Date of birth	April 12, 1979
Country of citizenship	China
Place of birth	Guiyang, China

Education

2007-Present **PhD Thesis:** The Virtual Ear: Deducing Transducer Function in the Drosophila Ear
Supervisor: Prof. Dr. Martin C. Göpfert, Cellular Neurobiology, Georg-August-University Göttingen, Germany

2006-2007 **Diploma thesis:** Peptid-Tyrosinkinase Inhibitor: Searching for Appropriate Sequences by Using Phage Display
Supervisor: Prof. Dr. H.W.Klein, Institute of Biochemistry, University of Cologne, Germany

2000-2006 **Study of biology**

Publications:

[1] Lu et al.: Using Drosophila for studying fundamental processes in hearing. Integr Comp Biol 49, 674680 (2009)

[2] P. Senthilan, Q. Lu und M.C. Göpfert: Grundlage des Hör- und Gleichgewichtssystems. Hören und Gleichgewicht 7. Hennig Symposium, Springer Wien New York (2010)